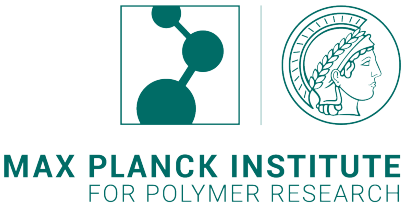

Master Thesis

Synthesis of thermally activated delayed fluorescence emitters and incorporation in novel single-layer OLED approaches

Mahni Fatahi
Mainz
June 2022

This work was carried out under the supervision of Dr. Jasper Michels at the Max Planck Institute for Polymer Research (MPIP) in Mainz, in the Molecular Electronics Group headed by Prof. Dr. Paul Blom.

First reviewer: Dr. Jasper Michels
Second reviewer: Prof. Dr. Heiner Detert

Eigenständigkeitserklärung

Ich, Mahni Fatahi, Matrikelnummer 2757020 versichere, dass ich meine Masterarbeit selbstständig verfasst und keine anderen als die angegebenen schriftlichen und elektronischen Quellen sowie andere Hilfsmittel benutzt habe. Alle Ausführungen, die anderen Schriften wörtlich oder sinngemäß entnommen wurden, habe ich kenntlich gemacht.

Ort, Datum | Unterschrift

Acknowledgements

First of all, I would like to thank Prof. Dr. Paul Blom for giving me the opportunity to do the Master's thesis in his group. And therefore giving me the opportunity to gain a deeper understanding in the field of organic semiconductors. Furthermore, I would like to thank Dr. Jasper Michels for the scientific supervision of the project, which enabled me to learn a lot about scientific work and to present its results.

I would also like to thank Prof. Heiner Detert, who agreed to assess this thesis as a second examiner.

A big thank you goes to Oskar Sachnik, who not only introduced me to the project but was always open to my questions and helped where he could. I am very happy to have had you as a colleague and wish you all the best for your further time at MPIP and beyond.

Big thanks also to Xiao Tan and Naz Ugur, who not only were nice office mates but also helped me with gaining a deeper understanding for device fabrication and measurement, as well as for spectroscopy. Big thanks to Dr. Gert-Jan Wetzelaer and Bas van der Zee, who helped me with the fitting and modelling of the device data and all questions about this topic.

I would also like to thank the technicians in the group, Verona Maus, Frank Keller and Christian Bauer, who were always there to help with problems in the labs. Without you, the realization of the project would not have been possible.

Apart from that, I would like to thank all the members of AK Blom for a great time. Not only was working with you a lot of fun, but also the lively discussions about all kinds of topics during the lunch breaks. I want to thank all of you for the warm welcome in the beginning and a very nice atmosphere in the labs.

I would like to thank my family for the motivation and support I received not only during my Master's thesis, but throughout my whole studies.

Last but not least, I would like to thank my friends and especially my girlfriend who always supported me and always gave me a sympathetic ear. Thank you Christin Lind, Georg Lutz, Janis Köster, Julian Titze and Vera Spanke.

1 Zusammenfassung

Organische Leuchtdioden (OLEDs) haben in den letzten Jahren immer mehr an Bedeutung gewonnen, so werden sie heutzutage in vielen elektronischen Geräten mit Bildschirm, wie beispielsweise Smartphones oder Fernsehern verbaut. Aufgrund der vielen Vorteile gegenüber der Flüssigkristall Display (LCD) Technologie verdrängen OLEDs diese Bildschirme zunehmend vom Markt, so sind OLEDs nicht nur energiesparender, farbechter und günstiger, sondern können auch umweltfreundlicher produziert werden[1][2]. Jedoch steht die OLED auch noch vor einigen Herausforderungen, eine der größten Herausforderungen stellt dabei die Suche nach einem effizienten und stabilen blauen Emitter dar. Um dieses Ziel zu erreichen, muss aber zunächst ein tieferes Verständnis für den Einfluss verschiedener Eigenschaften von Emittern auf deren Charakteristiken in einer OLED erlangt werden. Eine weitere Herausforderung ist eine weitere Senkung der Produktionskosten, um die OLED neben dem Einsatz in Bildschirmen für den Einsatz in Leuchtmitteln, wie Glühbirnen, interessant zu machen[3]. Diese Reduktion der Kosten könnte durch eine flüssig-prozessierte Einschicht-OLED, welche nur aus einer zwischen den Elektroden liegende, durch Flüssigprozession aufgetragene Emitterschicht besteht, realisiert werden[4]. Hier ist es ebenfalls nötig, ein grundlegendes Verständnis für Einflüsse von löslichkeitsvermittelnden Gruppen auf Emittereigenschaften zu gewinnen. Zusätzlich muss ein tiefer-gehendes Verständnis für Einflüsse der Gerätearchitektur auf die Leistung von OLEDs erlangt werden.

In dieser Arbeit sollen die beiden oben genannten Herausforderungen anhand von Fallbeispielen untersucht werden. In einer ersten Studie wurden vier Emitter mit gleicher chemischen Zusammensetzung, bestehtend aus einem Triazin-Akzeptor Baustein und drei Carbazol-Donor Bausteinen, mit variierter Konnektivität untersucht. Die, auf einem kürzlich publizierten blauen Emitter[5] basierenden, synthetisierten Emitter 9,9',9"-[5-(4,6-bis(4-fluorophenyl)-1,3,5-triazin-2-yl)benz-1,2,3-triyl]tris(9*H*-carbazol) (**345Trz**) 9,9',9"-[4-(4,6-bis(4-fluorophenyl)-1,3,5-triazin-2-yl)-benz-1,2,3-triyl]tris(9*H*-carbazol) (**234Trz**), 9,9',9"-[2-(4,6-bis(4-fluorophenyl)-1,3,5-triazin-2-yl)benz-1,3,4-triyl]tris-(9*H*-carbazol) (**236Trz**) und 9,9',9"-[5-(4,6-bis(4-fluorophenyl)-1,3,5-triazin-2-yl)-benz-1,2,4-triyl]-tris(9*H*-carbazol) (**245Trz**) sind in Abbildung 1.1 dargestellt.

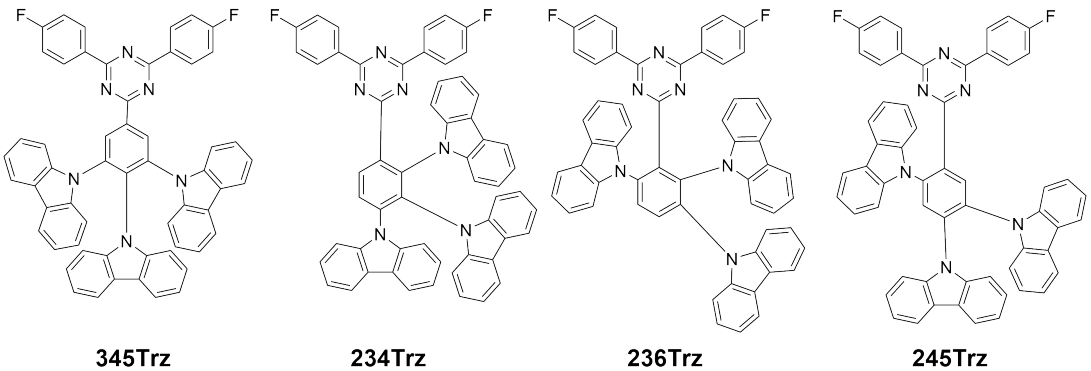

Abbildung 1.1: Emittermoleküle **345Trz**, **234Trz**, **236Trz** und **245Trz**.

Hierbei wurden sowohl die photophysikalischen Eigenschaften, als auch die Ladungstransporteigenschaften dieser Materialien untersucht, um Rückschlüsse hinsichtlich des Einflusses von relativer Donor-Akzeptoer Position zueinander auf für OLEDs grundlegende Eigenschaften, wie beispielsweise die Emissionswellenlänge oder Quantenausbeute ziehen zu können.

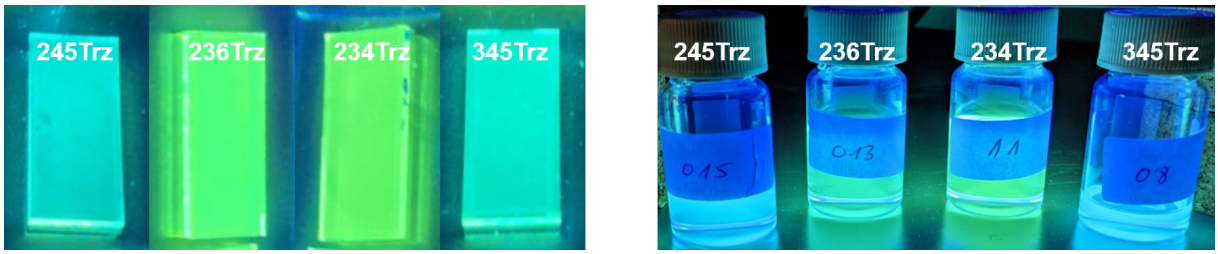

(a) Filme auf Quarzsubstraten. **(b)** Lösungen in Toluol.

Abbildung 1.2: Unterschiedliche Lumineszenz von a) Filmen auf Quarzsubstraten und b) Lösungen in Toluol der vier Emitter unter UV-Licht.

Anhand dieser Studie wurde gezeigt, dass die Position der Donor Bausteine sowohl Einflüsse auf die Emissionswellenlänge (siehe Abb. 1.2), als auch auf die Photolumineszenzquantenausbeute (PLQY) hat. Darüber hinaus wurden Unterschiede im Ladungstransport der vier Emitter beobachtet.

In einer zweiten Studie wurde, basierend auf Dichtefunktionaltheorie (DFT) Rechnungen ein Emitter mit einer Akzeptor-Donor-Akzeptor Struktur (siehe Abb.1.3), welcher ebenfalls auf Carbazol-Donor Bausteinen und Triazin-Akzeptor Bausteinen basiert, synthetisiert. Dieser Emitter sollte genutzt werden, um den Einfluss eines zweiten Triazin-Akzeptor Bausteins auf photophysikalische Eigenschaften, als auch die Ladungstransporteigenschaften zu untersuchen. Neben

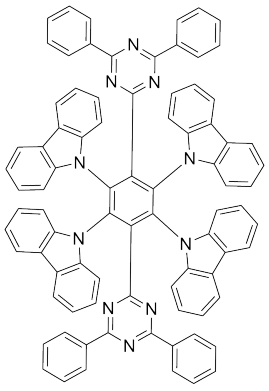

Abbildung 1.3: Akzeptor-Donor-Akzeptor Struktur **4Cz2Trz**.

der erfolgreichen Synthese von 9,9',9",9"'-(3,6-bis(4,6-diphenyl-1,3,5-triazin-2-yl)benz-1,2,4,5-tetrayl)- tetrakis(9*H*-carbazol) (**4Cz2Trz**) konnten aufgrund zu geringer Löslichkeit und Zerfall unter Evaporationsbedingungen (hohe Temperaturen und Hochvakuum) keine weiteren Unter-

suchungen durchgeführt werden. Somit war der Einbau in Einzelladungsträgergeräte, zur Untersuchung des Ladungsträgertransports von Elektronen und Löchern, sowie in OLEDs nicht möglich.

Um den Einfluss von löslichkeitsvermittelnden Gruppen auf Emittereigenschaften zu untersuchen, wurde in einer dritten Studie ein Derivat (siehe Abb. 1.4) des gut untersuchten Emitters 5,10-Bis(4-(9*H*-carbazol-9-yl)-2,6-dimethylphenyl)-5,10-dihydroboranthren (**CzDBA**) mit *tert*-butyl Gruppen synthetisiert und untersucht. Hierzu wurden nicht nur die photophysika-

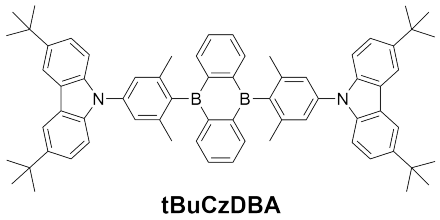

tBuCzDBA

Abbildung 1.4: Lösliches Emittermolekül **tBuCzDBA**.

lischen Eigenschaften von 5,10-bis(4-(3,6-di-*tert*-butyl-9*H*-carbazol-9-yl)-2,6-dimethyl-phenyl)-5,10-dihydroboranthren (**tBuCzDBA**) untersucht, sondern darüber hinaus auch die Ladungstransporteigenschaften in Einzelladungsträgergeräten sowie auch in OLEDs und mit **CzDBA** verglichen. Zusätzlich wurden verschiedene OLED-Architekturen getestet (siehe Abb. 1.5).

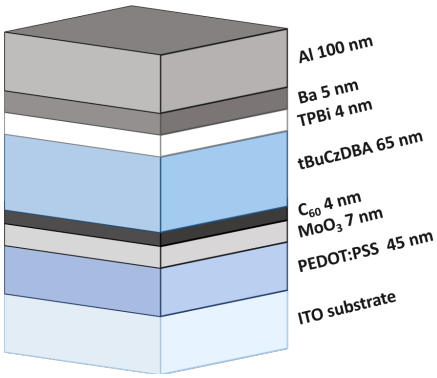

(a) Konventionelle Einschicht-OLED.

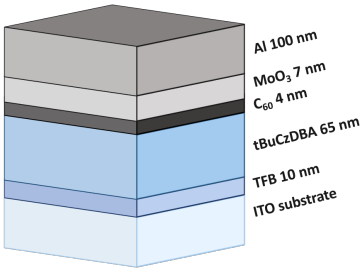

(b) Invertierte Einschicht-OLED.

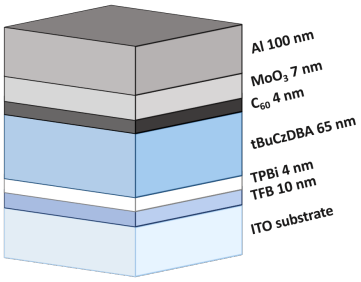

(c) Invertierte Einschicht-OLED mit TPBi Zwischenschicht.

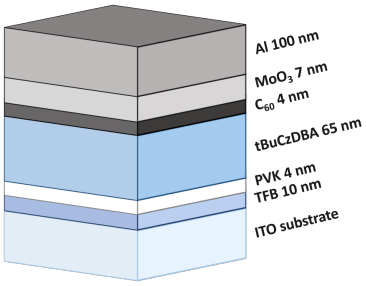

(d) Invertierte Einschicht-OLED mit PVK Zwischenschicht.

Abbildung 1.5: Konventionelle und invertierte Einschicht-OLED Architekturen mit **tBuCzDBA** als Emitter.

Anhand dieser Studie wurde gezeigt, dass die *tert*-butyl Gruppen keinen signifikanten Einfluss auf die Orbitaleigenschaften haben, darüber hinaus ist der Einfluss auf die PLQY gering. Der Ladungstransport hingegen, wird durch die *tert*-butyl Gruppen hingegen merklich beeinflusst: So konnte festgestellt werden, dass sowohl die Elektronenmobilität, als auch die Anzahl von Elektronenfallen in **tBuCzDBA** einen deutlichen Unterschied zu **CzDBA** aufweist. Des weiteren war die Leistung einer OLED mit **tBuCzDBA** als Emitter deutlich vermindert verglichen zu einer OLED mit **CzDBA**. Es konnte jedoch gezeigt werden, dass die OLED Leistung von Emittern mit ungleichmäßigem Ladungstransport von Elektronen und Löchern, durch den Einsatz einer invertierten OLED-Architektur verbessert werden kann.

2 Abstract

Organic light-emitting diodes (OLEDs) have become increasingly important in recent years, and are now present in a lot of electronic devices with screens, such as smartphones or televisions. Due to the many advantages over liquid crystal display (LCD) technology, OLEDs are increasingly displacing these screens from the market. OLEDs are not only more energy-efficient, more colorful and cheaper, but can also be produced in a more environmentally friendly way[1][2]. However, OLEDs still face some challenges, one of the biggest being the search for an efficient and stable blue emitter. To achieve this goal, a deeper understanding of the influence of different emitter properties on the characteristics of an OLED is needed. Another challenge is to further reduce production costs to make OLEDs interesting for use in light sources, such as incandescent bulbs[3]. This reduction in cost could be realized by a solution-processed single-layer OLED, which consists only of a solution-processed emitter layer sandwiched between the electrodes[4]. Here it is also necessary to gain a basic understanding of the influence of solubility mediating groups on emitter properties, in addition to a deeper understanding of the influence of device architecture on OLED performance.

In this work, the two challenges mentioned above will be investigated using case studies. In a first study, four emitters with the same chemical composition, consisting of a triazine acceptor building block and three carbazole donor building blocks, were investigated with varied connectivity. The synthesized emitters 9,9',9"-[5-(4,6-bis(4-fluorophenyl)-1,3, 5-triazin-2-yl)benzene-1,2,3-triyl]tris(9*H*-carbazole) (**345Trz**) 9,9',9"-[4-(4,6-bis(4-fluorophenyl)-1,3,5-tri-azin-2-yl)-benzene-1,2, 3-triyl]tris(9*H*-carbazole) (**234Trz**), 9,9',9"-[2-(4,6-bis(4-fluorophenyl)-1,3,5-triazin-2-yl) benzene-1,3,4-triyl]tris-(9*H*-carbazole) (**236Trz**) and 9, 9',9"-[5-(4,6-bis (4-fluorophenyl)-1,3,5-triazin-2-yl)-benzene-1,2,4-triyl]tris(9*H*-carbazoles) (**245Trz**), all based on a recently published blue emitter[5], are shown in Figure 2.1.

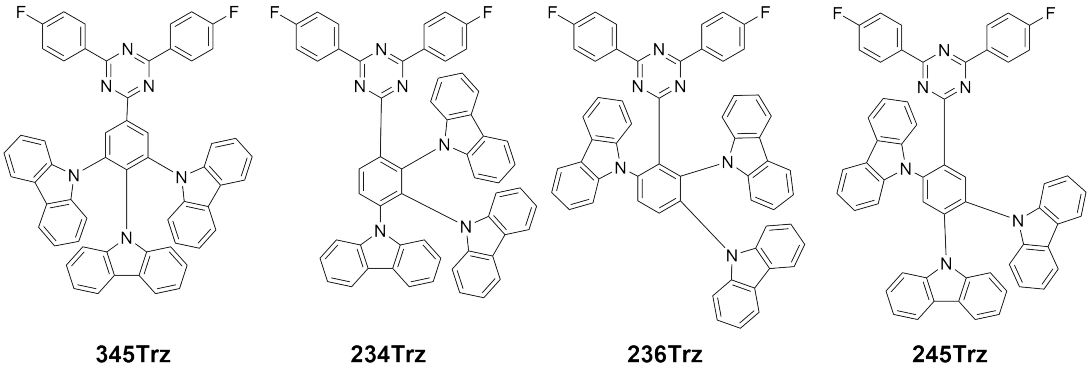

Figure 2.1: Emitters **345Trz**, **234Trz**, **236Trz** and **245Trz**.

The photophysical properties as well as the charge transport properties of these materials were investigated in order to draw conclusions regarding the influence of the relative donor-acceptor position on fundamental properties of OLEDs, such as emission wavelength or quantum yield.

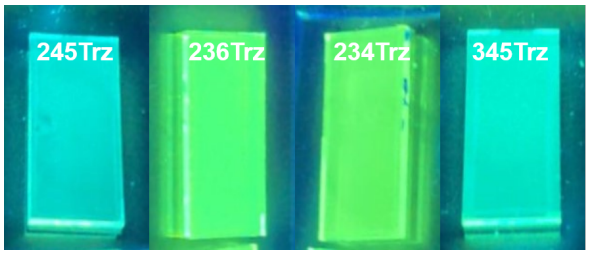

(a) Films on Quartz substrates.

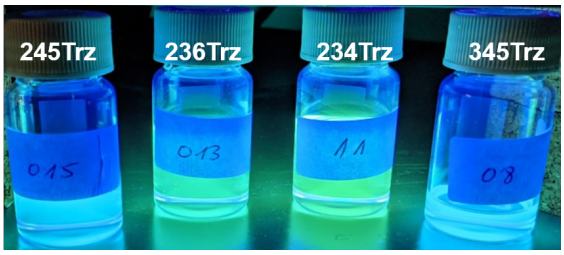

(b) Solutions in toluene.

Figure 2.2: Different luminescence of a) films on Quartz substrates b) solutions in toluene of the four emitters under UV light.

Based on this study, it was shown that the position of the donor devices has influence on the emission wavelength (see fig. 2.2) as well as on the photoluminescence quantum yield (PLQY). In addition, differences in the charge transport of the four emitters were measured.

In a second study, based on density-functional theory (DFT) calculations, an emitter with an acceptor-donor-acceptor structure (see fig. 2.3) also based on carbazole-donor building blocks and triazine-acceptor building blocks was synthesized. This emitter should be used to investigate the influence of a second triazine-acceptor building block on photophysical properties as well as charge transport properties.

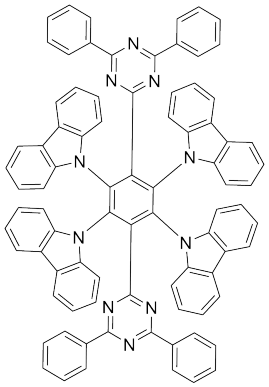

Figure 2.3: Acceptor-donor-acceptor structure **4Cz2Trz**.

Besides the successful synthesis of 9,9',9",9"'-(3,6-bis(4,6-diphenyl-1,3,5-triazin-2-yl)benzene-1,2,4,5-tetrayl)-tetrakis(9*H*-carbazole) (**4Cz2Trz**), no further studies could be carried out due to too low solubility and decay under sublimation or evaporation conditions (high temperatures and high vacuum). Thus, incorporation into single-carrier devices and OLEDs was not possible.

To investigate the influence of solubility-mediating groups on emitter properties, a derivative (see Fig. 2.4) of the well-studied emitter 5,10-bis(4-(9*H*-carbazol-9-yl)-2,6-dimethylphenyl)-5,10-dihydroboranthrenes (**CzDBA**) with *tert*-butyl groups was synthesized and investigated in a third study.

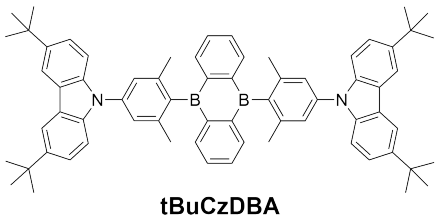

Figure 2.4: Soluble emitter **tBuCzDBA**.

For this purpose, not only the photophysical properties of 5,10-bis(4-(3,6-di-*tert*-butyl-9*H*-carbazol-9-yl)-2,6-dimethyl-phenyl)-5,10-dihydroboranthrenes (**tBuCzDBA**) were investigated, but furthermore the device characteristics in single charge carrier devices as well as OLEDs and compared with **CzDBA**. In addition, different OLED architectures were tested (see Fig. 2.5).

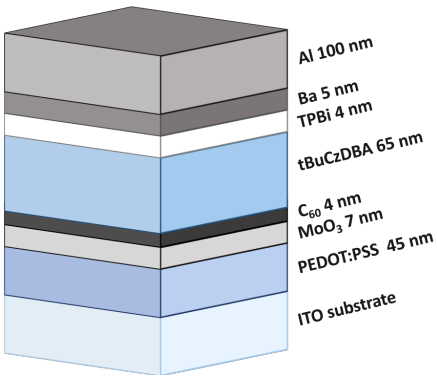

(a) Conventional single-layer OLED.

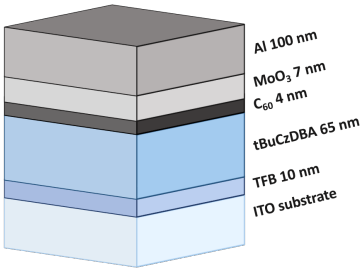

(b) Inverted single-layer OLED.

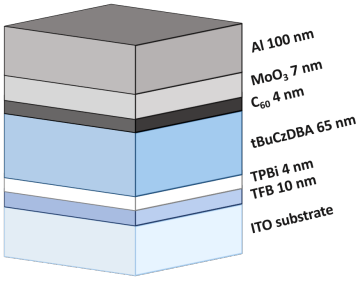

(c) Inverted single-layer OLED with TPBi interlayer.

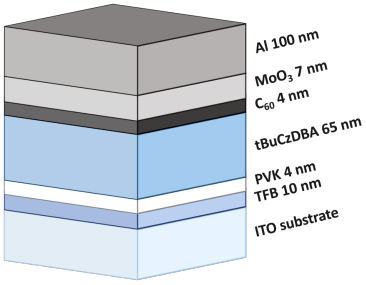

(d) Inverted single-layer OLED with PVK interlayer.

Figure 2.5: Conventional and inverted single-layer OLED architectures with **tBuCzDBA** as emitter.

Based on this study, it was shown that the *tert*-butyl groups have no significant effect on the orbital properties, moreover, the influence on the PLQY is small. The charge transport on the other hand, is noticeably affected by the *tert*-butyl groups. It was found that both the electron mobility and the number of electron traps in **tBuCzDBA** showed a significant difference from **CzDBA**. Furthermore, the performance of an OLED with **tBuCzDBA** as the emitter was significantly decreased compared to an OLED with **CzDBA**. However, it was shown that the OLED performance of emitters with unbalanced charge transport can be improved by using an inverted OLED architecture.

Contents

3 Introduction

Organic light emitting diodes (OLEDs) have become an indispensable part of our everyday lives. They are incorporated in many modern electronic devices such as smartphones, TV screens or laptops. The foundation for the development of OLEDs as we know them today was laid in 1987 by C. Tang and VanSlyke. By introducing a electroluminescent diode with 8-hydroxyquinoline aluminum (Alq_3) as organic emitter[6], they opened up an completely new field of research that less than 40 years later was to become a pioneering technology in almost all display applications. Modern OLEDs show several advantages over the conventional liquid crystal display (LCD) technology, which has been the market leader for many years. Since the pixels within an OLED screen are self-emitting, no background lighting as in LCD screens is necessary, which leads to a lower power consumption, a higher contrast and a better color purity[1]. Additionally, materials used in OLEDs can be produced cheaper and more environmentally friendly than for LCD screens[2]. Only by the incorporation of organic materials as emitters, technologies such as curved or transparent displays can be realized. Displays represent one of two major applications for OLEDs. The second application is lighting, where OLEDs offer a viable, energy efficient technology compared to conventional lighting products such as light bulbs and luminescent tubes. In recent years, the light bulb as invented by Edison[7] back in 1879, has been gradually replaced by the more energy-efficient (inorganic) light emitting diodes (LED) lamps[8]. Since the extraction of materials such as silicon is not very environmentally friendly, a more environmentally friendly technology is desired. This is where the OLED comes into play. However, in order to compete with LEDs, efficient, stable and above all, inexpensive, devices are needed[3]. OLED research has come a long way to catch up with LEDs. So, the first generation of organic emitters, based on fluorescent compounds was very inefficient and unstable. The first OLEDs that were efficient and stable were built with so-called second generation emitters. Emitters of this generation are based on heavy metal complexes, but the heavy metals used are not only expensive and toxic to humans, but the development of an efficient and stable blue emitter was not successful[9]. Research was continued and a third generation was introduced, which includes so-called thermally activated delayed fluorescence (TADF) emitters[10]. These emitters are cheaper, less toxic, more environmentally friendly and easier to process than the ones of previous generations[11]. But even for the third generation the design of an efficient and stable blue emitter is still a great challenge[12]. Meanwhile, conventional multilayer OLEDs (more details in Chapter 4.1) have shown to be efficient and stable[13], but due to the fact that within such a device a lot of different layers are incorporated, the production costs are quite high, because every additional layer adds an additional production step. In order to reduce costs and workload, the most simple device structure of an emitting layer sandwiched between two electrodes, a so-called single-layer OLED, would be ideal[4]. The concept of such devices will be further explained in Chapter 4.6. In addition to the modified device structure, the way the emitting layer is deposited on the device can be modified. Usually the emitting layer in an OLED is fabricated by thermal evaporation in vacuum. This methods requires a high vacuum evaporator and is quite time-consuming. In order to reduce the production costs further, this emitting layer could be fabricated by solution-processing methods

such as spin-coating or inject-printing. For that, a soluble emitter is required[3]. To develop such a solution-processed single-layer OLED, which is on the one hand efficient and stable, but on the other hand also inexpensive, is currently still a big challenge. In order to get one step closer to this goal, it is necessary to have a deeper understanding about the influences of emitter design and device structures on the efficiency of OLEDs.

4 Theory

4.1 Organic light emitting diodes

In general an OLED is built up from two electrodes, a cathode and an anode between which there are different layers of organic material. From the application of a voltage to the light output, there are various processes that take place in such a device. First, charges are injected from the electrodes, electrodes from the cathode and holes from the anode. After injection the electrons and holes have to be transported through the organic material in order to meet each other and recombine to form a hole-electron pair or so-called exciton. Under certain conditions, the relaxation of this exciton can lead to the emission of a photon. Since each of these processes involves a potential loss of efficiency and stability, an attempt was made to optimize them[13]. This optimization was achieved by introducing different organic layers. Therefore conventional OLEDs consist of multiple organic layers between the electrodes and are called multilayer OLEDs (see fig. 4.1). Within this architecture two electrodes (anode and cathode), two charge injection layers (hole and electron injection layer), two charge transport layers (hole and electron transport layer), two charge blocking layers (hole and electron blocking layer) and one emitting layer can be found.

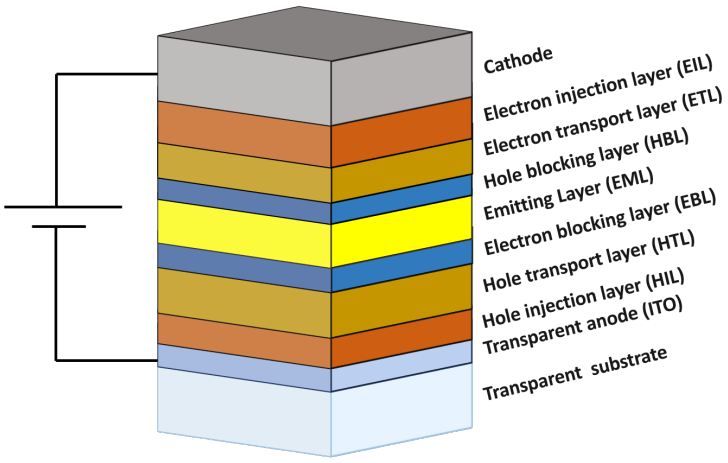

Figure 4.1: Device architecture of a conventional multilayer OLED.

4.2 Charge injection

To achieve efficient charge injection, it is necessary, that the work function of the electrode and the emitting layer (EML) align. Since this is often not the case for conventional electrodes, an injection barrier is formed. This injection barrier requires an increased voltage to overcome, which has a negative effect on the stability of an OLED. To avoid this, charge injection layers are used which reduce the work function of the anode and increase the work function of the cathode (see fig. 4.2)[13].

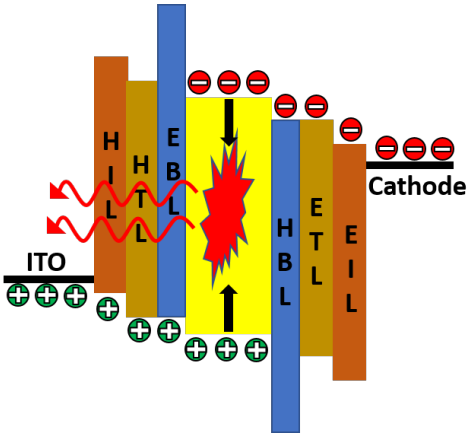

Figure 4.2: Schematic band diagram of a conventional multilayer OLED.

4.3 Charge transport

After the charges have been injected from the electrodes they need to be transported to the EML. In addition, the work function of the charge injection layers must be further aligned with that of the EML. This is achieved by the introduction of charge transport layers. Together with the charge injection layers the charge transport layers take part in a sort of staircase mechanism (see fig. 4.2). Since the charge injection layer may show an unbalanced charge transport, the charge transport layers ensure that holes and electrons are recombining exclusively inside the emitting layer[14]. Additionally, charge blocking layers are used to prevent counter charges from reaching the counter electrode and causing a short circuit. These charge blocking layers have very high (for electrons) or very low (for holes) work functions to prevent a transfer of the counter charges (see fig. 4.2). In order to determine the charge transport properties of an organic semiconductor single-carrier devices, in which only one type of charge carrier is allowed are used (see fig. 4.3). There are two types of single-carrier devices, those who only conduct electrons are called electron-only (EO) devices, the counterpart for positive charges is called hole-only (HO) device. In order to obtain a single-carrier device it is necessary to use electrodes from which only one type of charge, either holes or electrons can be injected into the organic semiconductor. This can be realized by a large energy difference between the work function of the electrode and the HOMO (EO) or LUMO (HO) level of the semiconductor, which creates a high injection barrier. Additional to that thin interlayers of buckminsterfullerene (C_{60}) (4 nm)

for the HO and 2,2',2"-(1,3,5-benzinetriyl)-tris(1-phenyl-1-*H*-benzimidazole) (TPBi) (4 nm) for the EO were used (see fig. 4.3). It has been shown that with thin interlayers of these materials an Ohmic contact between electrode and semiconductor can be established. Ohmic injection means that there is no injection barrier present[15]. In fig. 4.3c and 4.3d schematic band structures with Fermi level alignment at the thermal equilibrium are displayed, here an injection barrier for one of the electrodes in an asymmetric EO device can be observed.

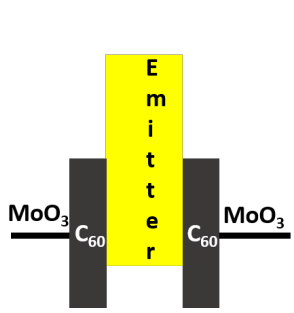

(a) Schematic band structure of a symmetric HO device architecture.

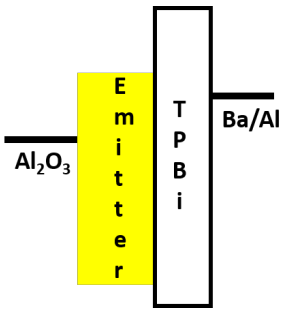

(b) Schematic band structure of an asymmetric EO device architecture.

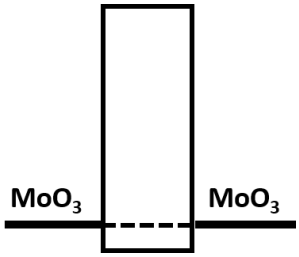

(c) Schematic band structure of a symmetric HO device architecture with Fermi level alignment at thermal equilibrium.

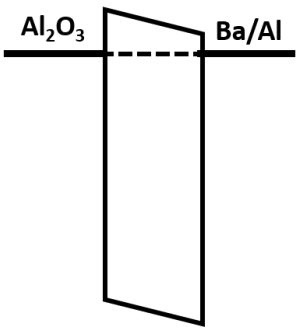

(d) Schematic band structure of an asymmetric EO device architecture with Fermi level alignment at thermal equilibrium.

Figure 4.3: Schematic band diagrams of a) symmetric HO and b) asymmetric EO devices and the corresponding band diagrams at the thermal equilibrium (c and d).

In Figure 4.4a the device architecture of a hole-only device is displayed. The device is build up from glass substrates with a patterned indium tin oxide (ITO) layer. On top of the substrate a 45 nm thick layer of poly(3,4-ethylenedioxythiophene) polystyrene sulfonate (PEDOT:PSS) is spin-coated, followed by an evaporated layer molybdenum trioxide (MoO_3) (7 nm) and an evaporated layer of C_{60} (4 nm). The next layer is an evaporated layer of the organic semiconductor. This layer is commonly 100-150 nm thick. On top, again the combination of C_{60} (4 nm) and MoO_3 (10 nm) is evaporated. The top electrode consists of a 100 nm thick layer of aluminium (Al). In fig. 4.4b the device architecture of an electron-only device is displayed. The device is

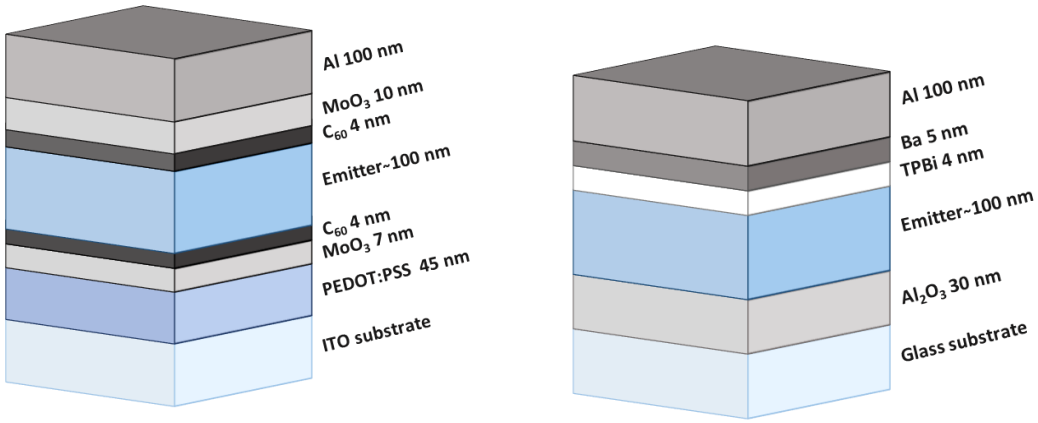

(a) hole-only device architecture

(b) electron-only device architecture

Figure 4.4: General architectures of single-carrier devices used for investigating charge transport properties. a) hole-only device architecture; b) electron-only device architecture.

built up from a glass substrate onto which a layer of 30 nm Al as bottom electrode is evaporated. In order to lower the work function, so that only electrons can be injected, the Al layer is exposed to air for no longer than 5 min to oxidize it to an Al_2O_3 layer. The next layer is an evaporated layer of the organic semiconductor. This layer is commonly 100-150 nm thick. On top of the emitter layer a 4 nm thick interlayer of TPBi is evaporated. The top electrode consists of a 5 nm thick layer of barium (Ba) and a 100 nm thick layer of Al.

The HO devices used in this work are built up symmetrically, therefore the work function of both electrodes is the same and holes can be injected from top or bottom depending on the bias (see fig. 4.3c), so also for negative bias a current is observed. These currents are measured in current-voltage measurements, a typical current density against voltage plot (JV plot) is displayed in fig. 4.5a. Here a symmetric curve can be observed, which means injection from top and bottom electrode has to be equal.

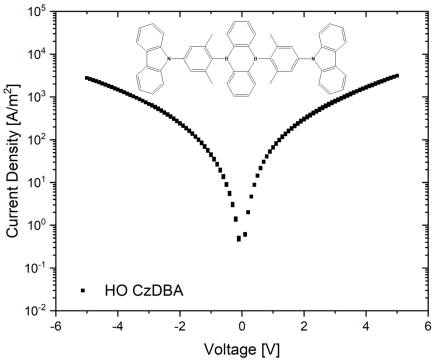

(a) semilog current density against voltage plot

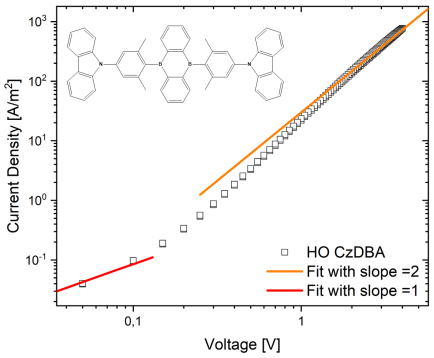

(b) log-log current density against voltage plot

Figure 4.5: Current density against voltage plot for a symmetric hole-only device of 5,10-Bis(4-(9*H*-carbazol-9-yl)-2,6-dimethylphenyl)-5,10-dihydroboranthrene (**CzDBA**) in a) semilog scale b) log-log scale[16].

If we take a look at the log-log scale (see fig. 4.5b) different current regimes can be observed. In the low voltage regime (diffusion regime), a linear JV dependence ($J \propto V$) can be observed (red line in fig 4.5b). The current can be described by a combination of Fick's first law of diffusion and Ohm's law[17]:

$$J_{diff} = nq\mu\frac{V}{L} \tag{4.1}$$

with J_{diff} the resulting current density, n the diffused charge carrier density, q the elementary charge, μ the charge mobility, V the voltage and L the thickness of the active layer. This diffusion regime is followed by the drift current regime, where the current is space charge limited and rises quadratically ($J \propto V^2$) (orange line in fig. 4.5b). This regime can be described by the Mott-Gurney law[18]:

$$J_{SCLC} = \frac{9}{8}\epsilon\mu\frac{(V - V_{bi})^2}{L^3} \tag{4.2}$$

With ϵ the dielectric constant of the emitter. In order to reach the space charge limited current regime, there are two prerequisites. The first is an Ohmic charge injection from the electrode into the semiconductor. The second prerequisite is that the semiconductor has to be trap free, because otherwise the current will be trap limited and will show a stronger voltage-dependence ($J \propto V^k$ with $k > 2$)[19].

The EO devices used in this work are built up asymmetric, therefore the difference between the work functions of the two electrodes causes a so-called built-in voltage Vbi (see fig. 4.3d). Here the electrons only can be injected from the top electrode, since the injection from the bottom electrode is hindered by an injection barrier[20]. A typical JV plot of an asymmetric EO device is displayed in Figure 4.6a.

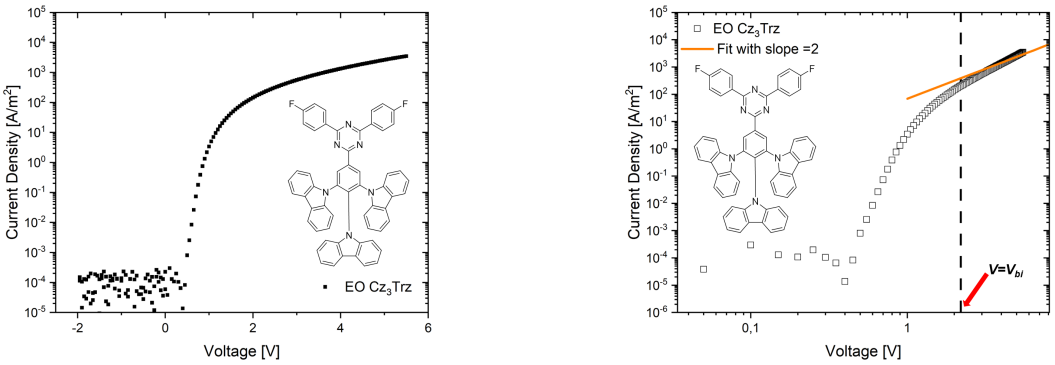

(a) semilog current density against voltage plot

(b) log-log current density against voltage plot

Figure 4.6: Current density against voltage plot for an asymmetric electron-only device of 9,9',9"-[5-(4,6-bis(4-fluorophenyl)-1,3,5-triazin-2-yl)benzene-1,2,3-triyl]tris(9H-carbazole) **345Trz** in a) semilog scale b) log-log scale.

In the log-log scale JV plot (see fig. 4.6b) again different current regimes can be observed. For the diffusion regime the JV dependence is no longer linear due to band bending at the top electrode, which is caused by accumulation of diffused charge carriers[20]. Further explanations about properties of the diffusion regime in asymmetric single-carrier devices and band bending in organic semiconductors can be found in references [20], [21] and [22]. After the applied voltage exceeds the built-in voltage V_{bi} (see fig. 4.6b), the current rises quadratically ($J \propto V^2$) (orange line in fig. 4.6b). This drift current regime can again be described by the Mott-Gurney law (eq. 4.2).

4.4 Charge recombination and light output

After the charges have been transported to the EML, they meet each other to form electron-hole pairs so-called excitons. In Figure 4.7 a Jablonski diagram for electrical excitation with following exciton formation is shown: 25% of the generated excitons are in the singlet state S_1 (total spin of S=0) and 75% of the generated excitons are in the triplet state T_1 (total spin of S=1).

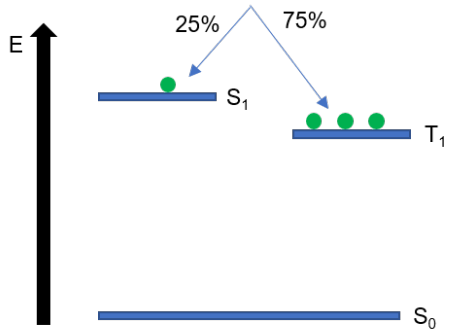

Figure 4.7: Jablonski diagram for electrical excitation.

This difference in occupation arises from the possible combinations of the half-integer spin of holes and electrons and is called spin-statistics. In fig. 4.8 the possible combinations of the half-integer spins of holes and electrons are displayed, it can be observed that there a three possible combinations that lead to a total spin of S=1 and therefore to the triplet state, while there is only one possible combination that leads to a total spin of S=0 and therefore to the singlet state.

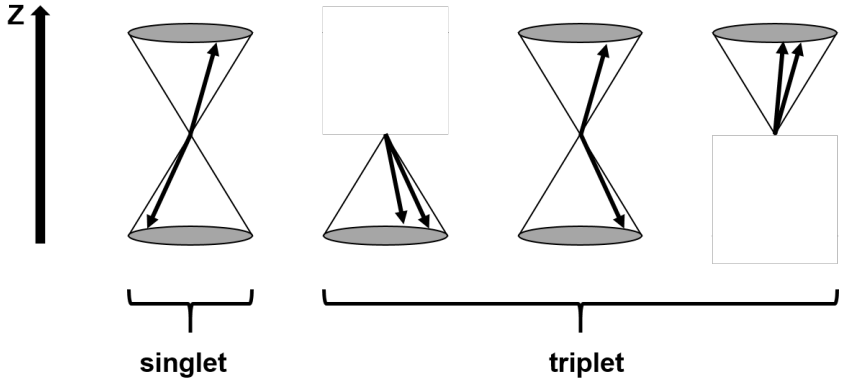

Figure 4.8: Spin statistic for excitons. Reproduced after literature[23].

In first generation OLEDs, purely organic fluorescent emitters have been used. By the fact that fluorescence is only generated by radiative relaxation from the S_1 level to the S_0 ground state, only 25% of the generated excitons can be transferred into emitted photons, which translates into

an internal quantum efficiency (IQE) of 25% in electroluminescent devices. The IQE describes the percentage of charges injected into the device that are transformed into photons within the device. The other 75% of excitons are trapped within the T_1 state because a radiative transition from T_1 to S_0 is forbidden due to a necessary spin flip. So 75% of the generated excitons are long-living and decay non-radiatively to the ground state (see fig. 4.9).

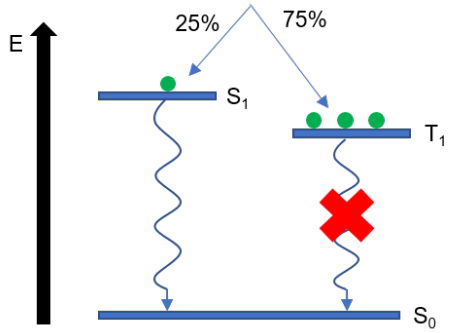

Figure 4.9: Jablonski diagram for first generation OLEDs using fluorescence emitters.

In order to increase the IQE the concept of the first generation has been improved, in the following, second generation heavy metals have been introduced into the until then purely organic emitters. The incorporated heavy metals are responsible for an increased spin-orbit coupling (SOC). The increased SOC now enables a radiative transition from T_1 to S_0, which is called phosphorescence. Additionally, the increased SOC enables a transition from S_1 to T_1 the so-called intersytem crossing (ISC) (see fig. 4.10). If the rate of ISC is higher than the rate of fluorescence decay up to 100% of the generated excitons populate the triplet state and decay via phosphorescence and IQE up to 100% can be achieved[24].

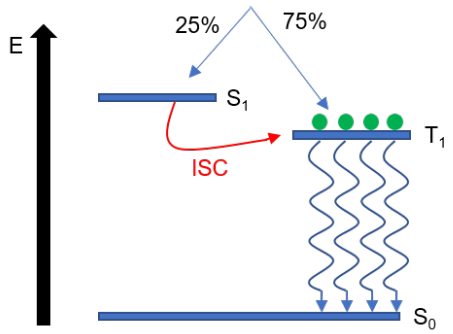

Figure 4.10: Jablonski diagram for second generation OLEDs using phosphorescence emitters.

4.5 Thermally activated delayed fluorescence

A third generation of OLEDs was introduced, which includes so-called thermally activated delayed fluorescence (TADF) emitters[10]. These kind of emitters are purely organic fluorescence emitters, but due to the fact, that they posses a very small energy gap between the S_1 and the T_1 state, usually smaller than 100 meV, the generated triplet excitons can be transferred into the singlet state via a process called reverse intersystem crossing (RISC) (see fig. 4.11)[25].

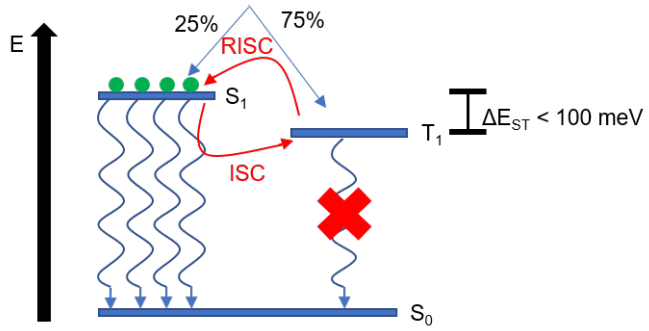

Figure 4.11: Jablonski diagram for third generation OLEDs using TADF emitters.

Since the decay form T_1 to S_0 is forbidden and therefore has a very low rate constant the generated triplet excitons get converted into the singlet state via RISC and decay from there via fluorescence. The rate-determining step in TADF is the RISC process, since its rate is much lower than the rate for fluorescence decay. One approach to increase its rate (k_{RISC}) is to minimise the energy difference ΔE_{ST} between T_1 and S_1, based on equation 4.3, a fitted Arrhenius equation[26].

$$k_{RISC} = A\ exp\ (-\frac{\Delta E_{ST}}{kT}) \tag{4.3}$$

With A the pre-exponential factor, k the Boltzmann constant and T the temperature. The term ΔE_{ST} in equation 4.3 corresponds to the energy difference between the lowest excited singlet state S_1 and the lowest excited triplet state T_1. The energy of the individual states can be understood as the sum of the orbital energy E_{orb}, the repulsion energy between electrons K and the exchange energy J, which corresponds to the first-order quantum mechanical correction. This correction contains the electron-electron repulsion according to the Pauli principle. If one now forms the difference of equations 4.4 and 4.5, one obtains $2J$ as the value for the energy difference ΔE_{ST}.[26]

$$E_{S1} = E_{orb} + K + J \tag{4.4}$$

$$E_{T1} = E_{orb} + K - J \tag{4.5}$$

$$\Delta E_{ST} = E_{S1} - E_{T1} = 2J \tag{4.6}$$

The exchange energy J can be minimised by a spatial separation of the highest occupied molecule orbital (HOMO) and the lowest unoccupied molecule orbital (LUMO). To achieve this separation, there are two main approaches: It can either be achieved by a twist within the molecular structure between donor (HOMO) and acceptor (LUMO) or by a fixed separation (e.g. spiro compounds). With this kind of emitters a quantum yield of up to 100% is possible. In order to get light output from an OLED, a radiative charge recombination within the EML, as shown above, is necessary. Therefore all layers within a multilayer OLED architecture have to be optimized, so that the hole and electrons recombine within the EML. In order to compare the OLEDs with each other, a standard benchmark for the performance of OLEDs, the external quantum efficiency (EQE) has been introduced. This value represents the percentage of injected charges that can be harvested as photons outside the device. However, this EQE is strongly limited by the outcoupling efficiency, which describes how many of the photons generated in the device are outcoupled from the device. The outcoupling efficiency for common OLEDs is about 25-30%, which means that an emitter with an internal quantum efficiency (IQE) of 100% can achieve a maximum EQE of 25-30%[27].

4.6 Single-layer OLED

In comparison to the introduced multilayer OLED a single-layer OLED consists only from an EML sandwiched between two electrodes. The absence of charge injection, charge transport and charge blocking layers simplifies the device architecture a lot, but on the other hand also increases the demands on the properties of the emitter. Since the emitter has to compensate the properties of all the mentioned layers. A first step towards a highly efficient single-layer OLED with a simplified device architecture has recently been made by Kotadiya and coworkers[28]. They present an OLED architecture as displayed in fig. 4.12a, as a promising single-layer approach. In fig. 4.12b a schematic band diagram of the architecture is shown. Here it can be observed, that there is no staircase mechanism like in the multilayer OLED mentioned above (see. fig. 4.2).

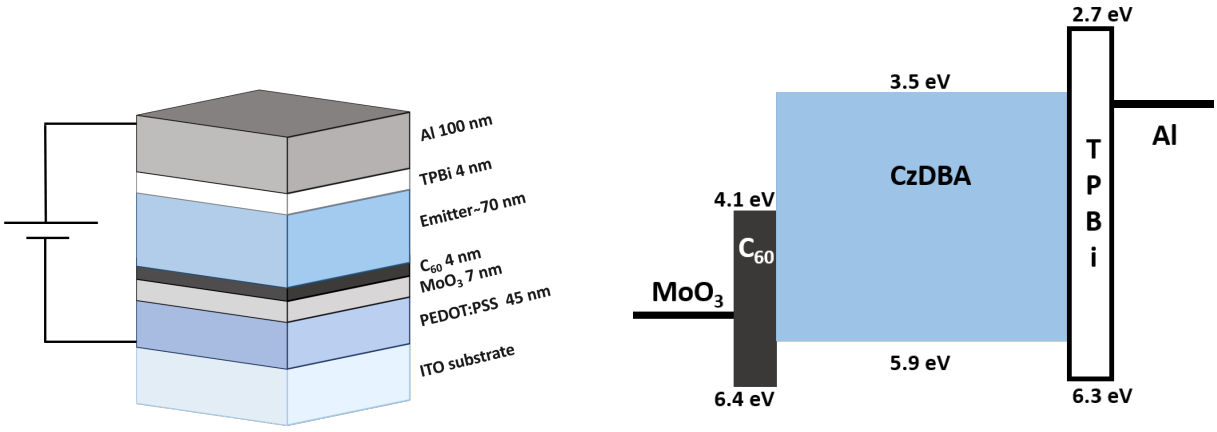

(a) Device architecture of a single-layer OLED.

(b) Schematic band diagram of a single-layer OLED.

Figure 4.12: Device architecture and schematic band diagram of a single-layer OLED as presented by Kotadiya and coworkers[28].

For this approach a MoO_3 anode (7 nm) has been evaporated on top of a ITO substrate with spin-coated PEDOT:PSS on top. On the MoO_3 anode a thin interlayer (4 nm) of C_{60} was evaporated in order to form an Ohmic contact between MoO_3 and the emitter. On top of an evaporated layer of **CzDBA** (70 nm) a thin interlayer of TPBi (4 nm) was evaporated in order to form an Ohmic contact with the Al cathode (100 nm) on top[28]. An exemplary JV plot for a singe-layer OLED is displayed in Figure 4.13. This plot can be split up into three sections which are marked in the graph.

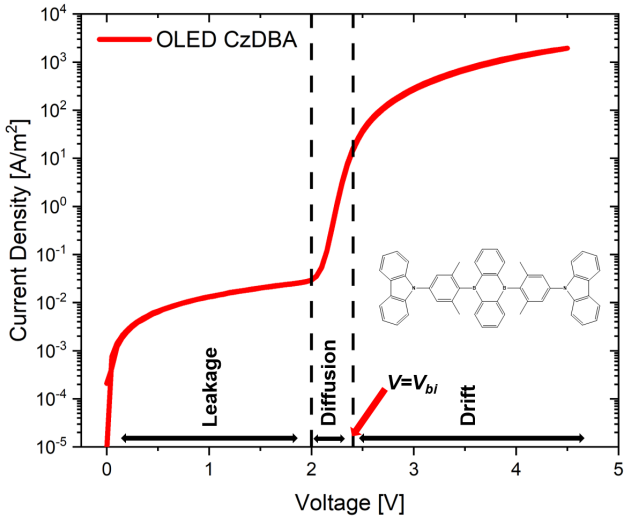

Figure 4.13: Current density against voltage plot for a single-layer OLED of 5,10-Bis(4-(9*H*-carbazol-9-yl)-2,6-dimethylphenyl)-5,10-dihydroboranthrene (**CzDBA**) in semilog scale[28].

In the first regime the current shows a linear dependence on voltage and represents the leakage current. This leakage current arises from parasitical currents between the electrodes[29], but does not indicate major defects. In case of major defects, this leakage current would be several orders of magnitude higher, resulting from short circuits[30]. In the second regime the resulting current is dominated by diffusion of charges and shows an exponential dependence on voltage ($J \propto e^V$). The current in this diffusion regime can be described by the Shockley diode equation[31]:

$$J = J_0 \left[exp\left(\frac{V}{\eta V_T}\right) - 1 \right] \tag{4.7}$$

with J_0 the saturation current density, η the ideality factor which has a value between $\eta = 1$ to $\eta = 2$. $\eta = 1$ corresponds to a trap free charge transport and $\eta = 2$ corresponds to a trap assisted recombination[32] and V_T the thermal voltage. This thermal voltage describes the potential through which an electron would gain an energy equal to the thermal energy (kT). Within this regime the current density shows a strong temperature dependence due to the temperature dependence of the saturation current density J_0 and the ideality factor η[29][33].After the built-in voltage V_{bi} the drift current regime begins, within this regime the current is space charge limited and shows a quadratic dependence on voltage following the Mott-Gurney law (eq. 4.2)[29]. For a trap limited emitter a higher current dependence on voltage is obtained ($J \propto V^k$ with $k > 2$).

In contrast to the above mentioned multilayer OLED, the recombination within a single-layer OLED can take place everywhere in the device, since no hole or electron blocking layer are used. Recently our group has shown, that a broad recombination profile within the center of EML is desirable, in order to achieve a high outcoupling efficiency and therefore a high EQE for single-layer OLEDs[27].

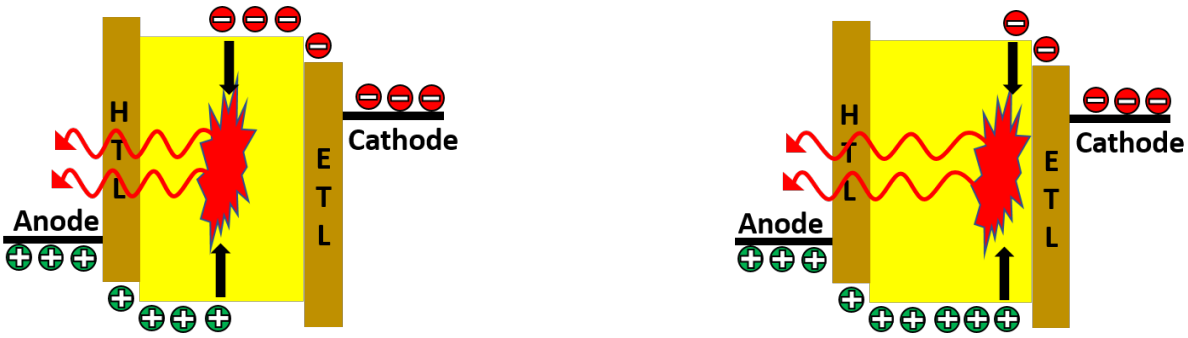

(a) Centered recombination.

(b) Shifted recombination.

Figure 4.14: Centered and shifted recombination in OLEDs due to balanced and unbalanced charge transport.

A centered recombination of holes and electrons in single-layer OLEDs (see fig. 4.14a) is only the case for emitters that exhibit balanced charge transport. A good estimation whether an emitter has a balanced charge transport is by comparing the density of electron and hole traps. Estimating a high density of electron or hole traps, can be done by comparing the highest occupied molecular orbital (HOMO) and the lowest unoccupied molecular orbital (LUMO) energies to the so-called trap-free window, which has been recently published[19]. It has been demonstrated that for compounds with an ionization energy (IE) of lower than 6 eV behave trap-free regarding hole transport. On the other side compounds with an electron affinity (EA) of higher than 3.6 eV behave trap-free regarding electron transport. Additional to that the compounds which are within this trap-free window show a quadratic dependence of current to voltage in the drift current regime, following eq. 4.2. If, like in many cases for organic emitters the hole transport is enhanced compared to the electron transport the recombination zone is shifted towards the top electrode (cathode) (see fig. 4.14b). In this scenario the generated excitons are much closer to the emitter/metal interface and therefore the formation of surface plasmon polariton, which represents a non-radiative decay is more likely[27][34]. There are two different possible solutions for a single-layer OLED approach incorporating an emitter with unbalanced charge transport. The first option is to use an optimized OLED architecture with a thicker interlayer between the EML and the cathode. Since this approach would no longer represent a single-layer OLED, another approach was chosen. The second more, and promising, approach is an inverted architecture of a single-layer OLED where cathode and anode are switched. The latter will be tested and discussed in this work.

5 Motivation

In order to design an efficient and stable blue emitter it is indispensable to derive a deeper understanding which factors influence the electronic and photophysical properties of TADF molecules. Additionally, to the blue emission, a high solubility in common organic solvents is of great interest in order to achieve solution-processed devices. Since the dilution of the emitting layer with polymers such as polystyrene (PS) is only feasible with solution processing and would be impossible with co-evaporation methods. Such dilutions are used to increase the efficiency of OLEDs, due to a reduced self quenching in the EML. The aim of this work is the synthesis, investigation and comparison of a range of organic emitters with a systematically varied molecular structure, based on a recently published sky-blue TADF emitter consisting of a triazine acceptor and carbazole donor units, which achieved an exceptional external quantum efficiency (EQE) of 25% in an OLED[5].

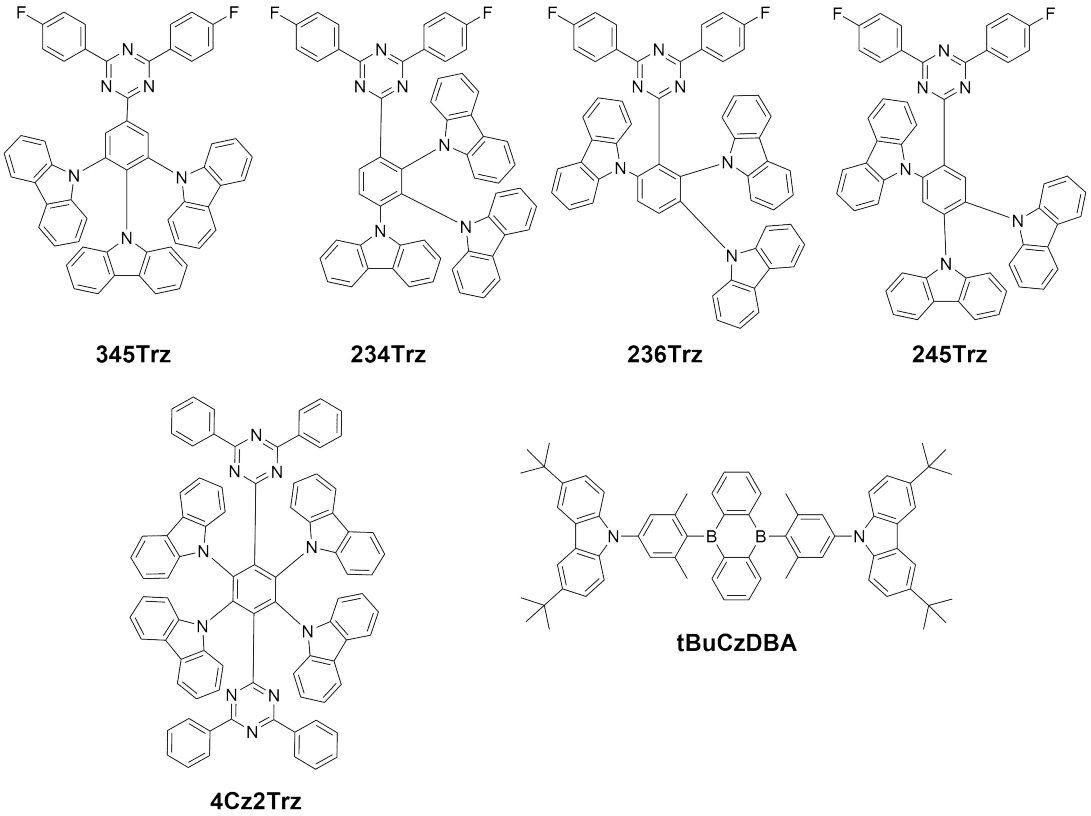

Figure 5.1: Target molecules **345Trz**, **234Trz**, **236Trz**, **245Trz**, **4Cz2Trz** and **tBuCzDBA**.

Recent investigations at our group demonstrated trap-free electron and hole currents for the emitter published by Lee and coworkers[5]. Therefore a group of five molecules consisting of carbazole donor units and triazine acceptor units was designed, synthesized and investigated regarding photophysical and charge transport properties. Four of the five molecules are com-

posed of one triphenyltriazine acceptor unit and three carbazole donor units. The fifth molecule contains two acceptor units and four donor units (see **4Cz2Trz** in fig. 5.1). By varying the arrangement of the donor units on the central phenyl ring, or increasing the number of acceptors, a possible link between molecular structure and electronic properties may be identified.

As a reference molecule the symmetrically arranged 9,9',9"-[5-(4,6-bis(4-fluorophenyl)-1,3,5-triazin-2-yl)benzene-1,2,3-triyl]tris(9*H*-carbazole) (**345Trz**) will be used (see Figure 5.1). For the three compounds 9,9',9"-[4-(4,6-bis(4-fluorophenyl)-1,3,5-triazin-2-yl)benzene-1,2,3-triyl]tris(9*H*-carbazole) (**234Trz**), 9,9',9"-[2-(4,6-bis(4-fluorophenyl)-1,3,5-triazin-2-yl)benzene-1,3,4-triyl]tris-(9*H*-carbazole) (**236Trz**) and 9,9',9"-[5-(4,6-bis(4-fluorophenyl)-1,3,5-triazin-2-yl)-benzene-1,2,4-triyl]-tris(9*H*-carbazole) (**245Trz**) the carbazole units are arranged asymmetrically around the central phenyl ring. By comparing the asymmetric compounds to **345Trz**, we may identify differences in the photophysical and charge transport properties. Thus, we hope to obtain a deeper understanding on the link between the relative position of donor and acceptor and the optoelectronic properties.

As fifth target molecule 9,9',9",9"'-(3,6-bis(4,6-diphenyl-1,3,5-triazin-2-yl)benzene-1,2,4,5-tetrayl)-tetrakis(9*H*-carbazole) (**4Cz2Trz**) composed of two triphenyltriazine units and four carbazole units was synthesized. By investigating this acceptor-donor-acceptor (A-D-A) structure a possible link between the number of acceptor units and optoelectronic properties may be identified.

Additionally, the TADF molecule 5,10-bis(4-(3,6-di-*tert*-butyl-9*H*-carbazol-9-yl)-2,6-dimethylphenyl)-5,10-dihydroboranthrene (**tBuCzDBA**) consisting of two *tert*-butyl carbazoles as donor units and one diboraanthracene as acceptor unit was synthesized and investigated. The compound is very similar to the well known emitter 5,10-Bis(4-(9*H*-carbazol-9-yl)-2,6-dimethylphenyl)-5,10-dihydroboranthrene (**CzDBA**) but the attached *tert*-butyl groups provide significantly improved solubility, and make the molecule compatible with solution-processing. Nevertheless, its molecular weight is compatible with thermal evaporation, which we will employ as well for this particular emitter. To investigate the charge transport properties, electron-only (EO) devices and hole-only (HO) devices were used. By comparison of both a possible imbalance in charge transport of the compounds can be investigated. Additionally, the behaviour of **tBuCzDBA** in different OLED device structures was tested. These different architectures in principle allow to understand i) what the influence is of the solubilizing groups on optoelectronic performance and ii) differences in photophysical properties between devices obtained by evaporation and solution processing.

6 Comparison of Carbazole$_3$-triazine compounds

Within this section, the influence of spatial donor-acceptor arrangement on TADF properties will be discussed. Therefore four emitters, based on a recently published blue TADF emitter[5], each consisting of three carbazole donor units and a triazine acceptor unit with varied connectivity have been synthesized, investigated and compared to each other.

6.1 Synthesis and characterization

The four carbazole compounds shown at the top in Figure 5.1 have been synthesized in a three step synthesis starting from the appropriate trifluoro-bromo-benzene precursors (see Scheme 6.2). The first step represents a nucleophilic aromatic substitution of the fluoride by carbazole. In a second step the aryl-bromides were converted into corresponding boronic acids (**234Trz**, **236Trz** and **245Trz**) or the corresponding boronic acid pinacol ester (**345Trz**), both of which were used in a subsequent Suzuki coupling (see Scheme 6.2). The reaction to the boronic acid was carried out with trimethyl borate and *n*-BuLi, while the synthesis of the boronic acid pinacol ester was performed with bis(pinacol)diborane and Pd-catalyst (Miyaura-Borylation). The third step was a Suzuki coupling for all four substances with compound **Trz** which was previously synthesized in a Grignard reaction (see Scheme 6.1).

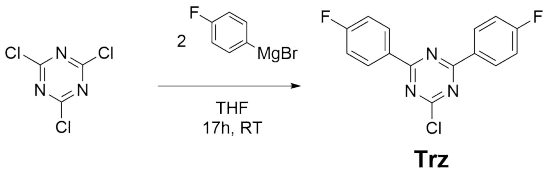

Trz

Scheme 6.1: Synthesis of triazine acceptor compound **Trz** via Grignard reaction.

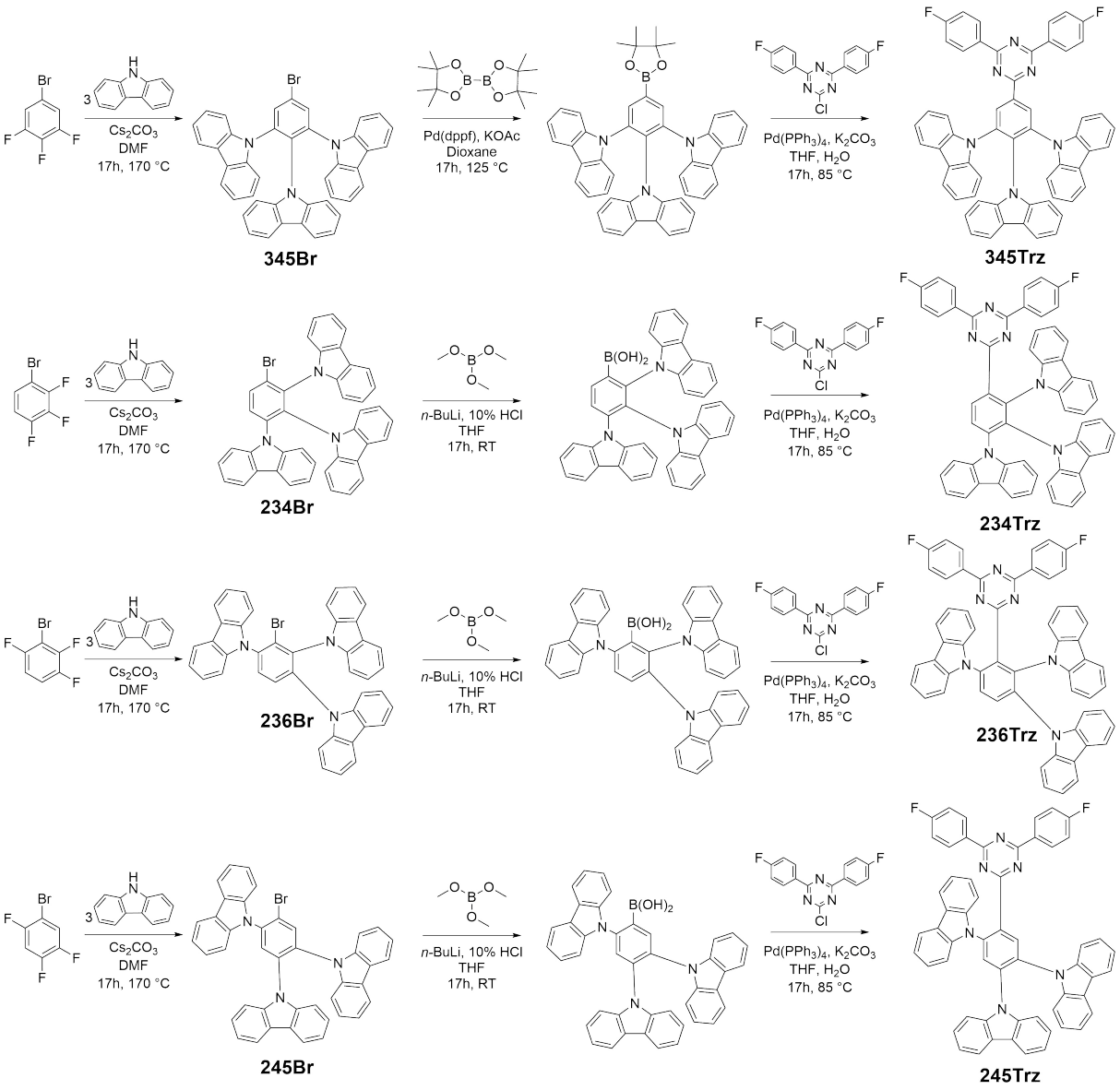

Scheme 6.2: Reaction chart for compounds **345Trz**, **234Trz**, **236Trz** and **245Trz**. With a nucleophilic aromatic susbstitution of a fluoro-benzene followed by a conversion into a boronic acid/ pinacol ester and as third step a Suzuki reaction to couple the donor and acceptor units.

All compounds were purified by column chromatography and sublimation to result in yellow powders. The purified compounds were characterized by ^{1}H-NMR, ^{13}C-NMR and atmospheric pressure chemical ionization (APCI) mass spectrometry (see Chapter 10.6, 10.7, 10.8 and 10.9 for details). For the ^{1}H-NMR a shift of the signals with the highest chemical shift at 8.6–9.2 ppm which can be assigned to the hydrogen atoms (marked in red) from the central phenyl ring (see fig. 6.1) can be observed. For **345Trz** one singlet is observed, since the two hydrogen atoms are equivalent, for **234Trz** and **236Trz** two doublets are present, since the the two hydrogen atoms are neighboring but not equivalent and for **245Trz** two singlets are present due to the different chemical environment of the two hydrogen atoms. The chemical shift for the ortho hydrogen atoms of the flouro-phenyl groups (marked in green, doublet of doublet) remains similar for **236Trz** and **245Trz** at 8.1 ppm, while for **345Trz** the signal is shifted to 8.8 ppm and for **234Trz** to 8.0 ppm. For the meta hydrogen atoms of the flouro-phenyl groups (marked in blue, triplet) again **236Trz** and **245Trz** show a similar signal at 7.4 ppm, **345Trz** shows a to 7.2 ppm shifted signal and **234Trz** shows the lowest chemical shift with 7.1 ppm.

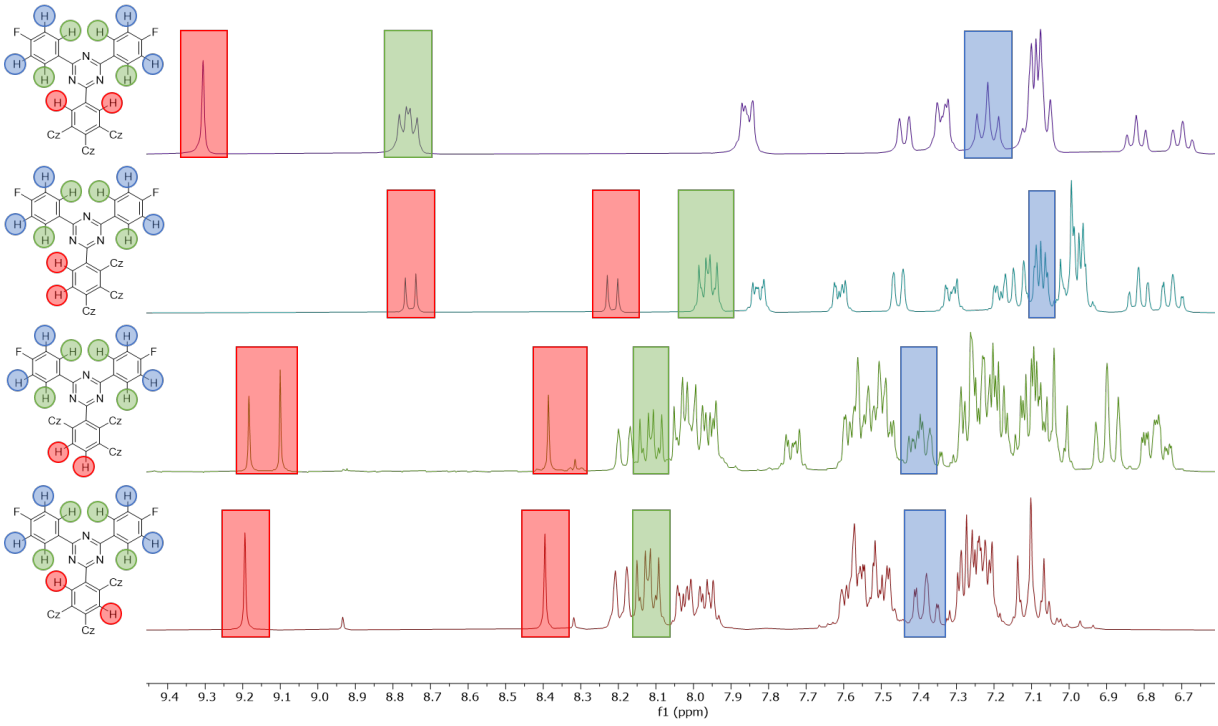

Figure 6.1: Aromatic region of ^{1}H-NMR spectra of compounds **345Trz**, **234Trz**, **236Trz** and **245Trz** (from top to bottom).

6.2 Theoretical calculations

For the above synthesized compounds DFT calculations have been performed to determine the HOMO and LUMO levels, as well as the singlet and triplet levels and the energy gap between them (ΔE_{ST}). Furthermore, the HOMO levels have been measured by ultraviolet photoelectron spectroscopy (UPS) in ambient atmosphere. In order to determine the LUMO levels, the optical band gap was subtracted from the experimental HOMO levels. The optical band gap was determined using the Tauc plot[35] following Equations 6.1 and 6.2.

$$E = \frac{hc}{\lambda} \tag{6.1}$$

With E the photon energy, h the Planck constant, c the speed of light and λ the wavelength of the photon. If we now assume that the optical band gap corresponds to the lowest absorbed photon energy, and therefore its wavelength (onset absorption) the following equation is obtained.

$$band\ gap = \frac{hc}{\lambda} = \frac{hc}{onset\ absorption} \tag{6.2}$$

All calculated and experimentally derived energy levels are displayed in Table 6.1. The calculated singlet energies (S_1) show similar values for **345Trz**, **234Trz** and **236Trz** (2.68–2.69 eV). Only **245Trz** indicates a little higher S_1 level (2.75 eV). The four compounds show some deviation in terms of triplet energy (T_1) . **345Trz** shows the lowest and **245Trz** the highest value (2.66 eV) across the series. The resulting ΔE_{ST} for **345Trz** is with 0.17 eV by far the largest in the investigated series, whereas **234Trz** has a ΔE_{ST} of only 0.07 eV. The high ΔE_{ST} of **345Trz** is unfavorable for efficient TADF, which relies on a high reverse intersystem crossing rate (k_{RISC}), and decreases with increasing ΔE_{ST}. The comparably low value of compound **234Trz** is an indicator for an efficient TADF emitter. For **236Trz** and **245Trz** the values are similar with 0.09 and 0.10 eV and within the usual range for TADF emitters[25].

Table 6.1: Determined energy levels for **345Trz**, **234Trz**, **236Trz** and **245Trz**.

compound		**345Trz**	**234Trz**	**236Trz**	**245Trz**
HOMO calc.[a]	[eV]	-5.45	-5.46	-5.50	-5.47
HOMO exp.	[eV]	-5.90	-5.91	-5.91	-5.92
LUMO calc.[a]	[eV]	-2.27	-2.26	-2.32	-2.21
LUMO exp.	[eV]	-3.03	-2.91	-2.97	-3.03
S_1 calc.[a]	[eV]	2.69	2.68	2.68	2.75
T_1 calc.[a]	[eV]	2.52	2.61	2.58	2.66
ΔE_{ST} calc.[a]	[eV]	0.17	0.07	0.10	0.09

[a] Calculated based on a TD-DFT approach at a B3LYP/6–31G level.

The differences between the measured and calculated HOMO and LUMO values in Table 6.1 arise from the fact that the latter are determined for vacuum conditions, while the experimental values were determined under ambient conditions as explained above. The calculated HOMO

values are very similar across all four compounds, this applies also to the experimental values. The only deviation can be observed for the LUMO of **245Trz** which according to the calculations has a higher LUMO than the other three compounds. Nevertheless, this deviation is not reflected by the experimental values. In Figure 6.2 the HOMO and LUMO distribution is displayed. Here it is noticeable that for compounds **345Trz** and **245Trz** the HOMO-LUMO overlap is smaller than for **234Trz** and **236Trz**.

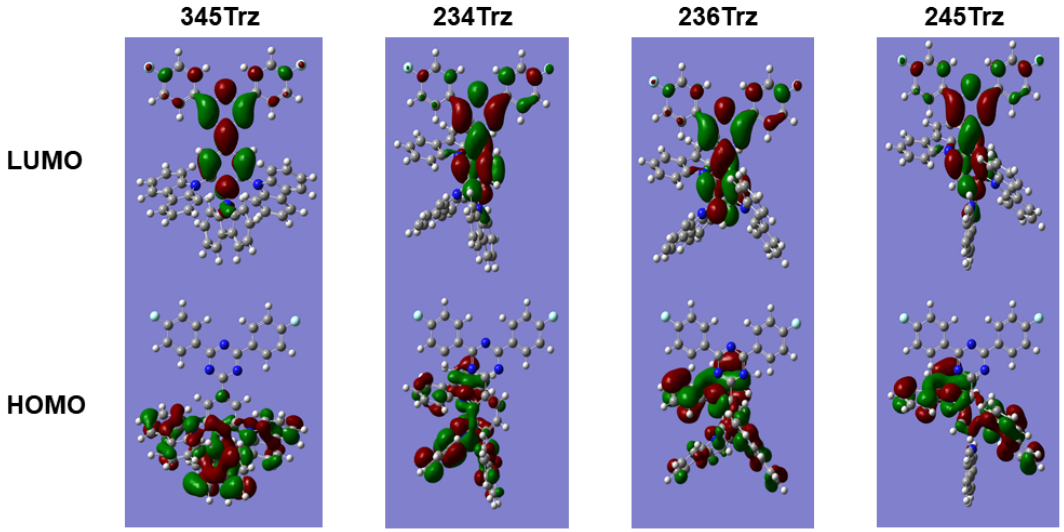

Figure 6.2: Calculated HOMO and LUMO distributions on optimized structures of **345Trz**, **234Trz**, **236Trz** and **245Trz**.

6.3 Photophysical properties

For solid state investigations all four materials were spin-coated on quartz substrates (20×10 mm), resulting in film thicknesses of around 100 nm (procedure is described in Chapter 10). These films were used for recording UV-Vis absorption and photoluminescence (PL) spectra, as well as for the determination of the photoluminescence quantum yield (PLQY). Additionally, solutions samples were prepared using dry toluene as a solvent. In Figure 6.3 absorption spectra of the solid state samples (films) (fig.6.3a) and dissolved samples (fig. 6.3b) are displayed. Small differences between the solid state and solution spectra can be observed. The wavelength of the lowest energy transition (LET) and the absorption maxima (Abs_{max}), as well as the used concentrations are displayed in Table 6.2. In both cases **345Trz** shows a red-shifted lowest energy transition compared to the three asymmetric compounds, although all four compounds show a similar second absorption maximum. For **236Trz** a difference between solution and film measurement can be observed: the film measurement exhibits a shoulder after the maximum at 338 nm, therefore the baseline is reached at a higher wavelength compared to the solution measurement. Further a slight red-shift for the LET, as well as for the absorption maxima in the film spectra compared to the solution spectra can be observed for all four compounds. Both of these observations indicate the formation of J-type aggregates in the film samples[36][37].

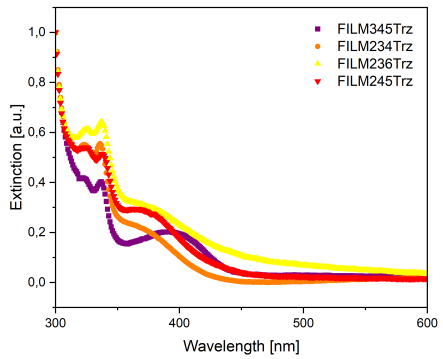

(a) Absorption spectra of spin coated films of compounds **345Trz**, **234Trz**, **236Trz** and **245Trz**.

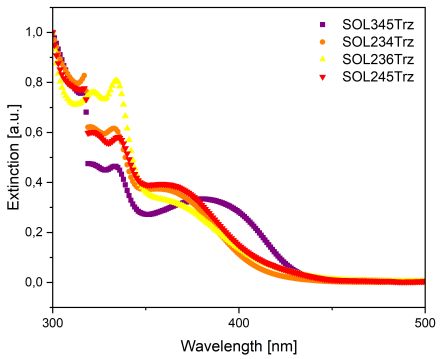

(b) Absorption spectra of 0.03 mg·mL^{-1} solutions in toluene of compounds **345Trz**, **234Trz**, **236Trz** and **245Trz**.

Figure 6.3: Absorption spectra of compounds **345Trz**, **234Trz**, **236Trz** and **245Trz**.

In Figure 6.4 the emission spectra of the film (fig. 6.4a) and the solution samples (fig.6.4b) as well as pictures of the samples under UV-light (254 nm) (fig. 6.4c and 6.4d) are displayed. The spectra of the films show that the emission maxima (see Table 6.2) of samples **345Trz** and **245Trz** are very similar. The emission maxima of samples **234Trz** and **236Trz** are very similar to each other too, but are red-shifted compared to **345Trz** and **245Trz**. This can also be observed by eye since films of samples of **345Trz** and **245Trz** show a sky blue fluorescence under UV irradiation, while films of samples of **234Trz** and **236Trz** appear to have a more green fluorescence.

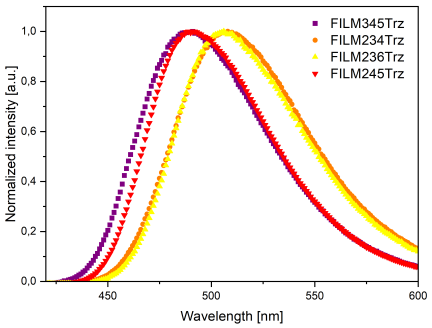

(a) Emission spectra of spin-coated films

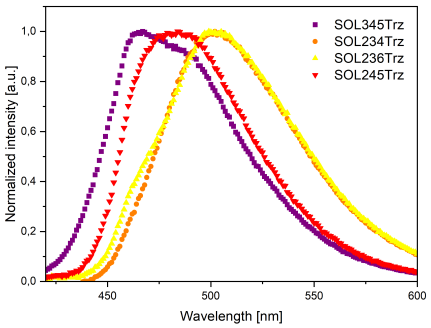

(b) Emission spectra of 0.015 mg·mL^{-1} solutions in toluene

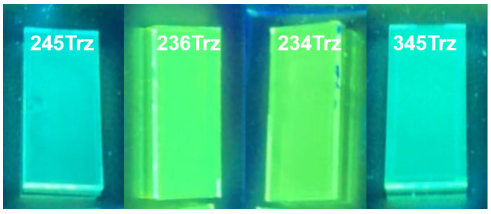

(c) Emission of spin coated films under UV-light

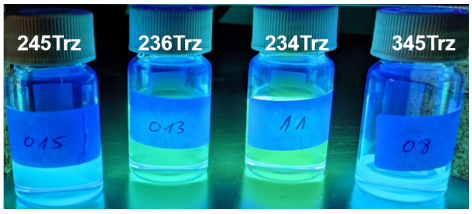

(d) Emission of toluene solutions under UV-light

Figure 6.4: Emission spectra of (a) spin-coated films and (b) 0.015 mg·mL^{-1} solutions in toluene of compounds **345Trz**, **234Trz**, **236Trz** and **245Trz**. Measured samples show visible distinguishable emission under UV-light (c and d).

If the film PL spectra of **234Trz**, **236Trz** and **245Trz** are compared to the corresponding solution PL spectra, it can be observed, that for the films the emission maximum is red-shifted by 6–7 nm. The reason for this red-shift can be J-type aggregation in the films[37]. The solution spectrum of sample **345Trz** shows a by 24 nm blue-shifted maximum compared to the film spectrum. This is caused by the appearance of a vibronic fine structure in the spectrum. For **245Trz**, a slight formation of a fine structure can also be observed. The reason this phenomenon is not observed for all four compounds is the larger Stokes shift of the green emitting materials, for which a lower fine structure splitting is observed. Under UV-light the solutions show a comparable fluorescence to the films. Samples **345Trz** and **245Trz** show sky-blue and **234Trz** and **236Trz** show green fluorescence (see fig. 6.4d).
The PLQY measurements of the film samples were carried out using an integrating sphere. The obtained values are displayed in Table 6.2. Although compounds **345Trz** and **245Trz** show similar emission wavelength, they differ significantly in terms of their quantum yield, compound **345Trz** shows a 9 % higher PLQY compared to **245Trz**. The green fluorescent compounds **234Trz** and **236Trz** show a relatively high PLQY, up to 55 %.

Table 6.2: Summary of photophysical properties of **345Trz**, **234Trz**, **236Trz** and **245Trz**.

		345Trz		**234Trz**		**236Trz**		**245Trz**	
		Film	Solution	Film	Solution	Film	Solution	Film	Solution
Conc.[a]	[mg·L^{-1}]	25	0.03/ 0.015	35	0.03/ 0.015	25	0.03/ 0.015	20	0.03/ 0.015
LET	[nm]	396	385	367	365	374	366	368	365
Abs$_{max}$	[nm]	337	334	336	333	338	334	338	335
Em$_{max}$	[nm]	491	467	508	502	506	499	491	484
PLQY	[%]	41	-	53	-	55	-	32	-

[a] Film: concentration of toluene solutions used for spin-coating films with a thickness of round 100 nm on quartz substrates. Solution: concentration of 0.03 mg·mL^{-1} in toluene used for UV-Vis and concentration of 0.015 mg·mL^{-1} used for PL measurements.

To investigate the TADF properties of the compounds time-resolved photoluminescence (TRPL) spectra were recorded on pristine evaporated films (100 nm) of **345Trz**, **234Trz** and **245Trz** on quartz substrates (20 × 10 mm)(see fig. A.5). Additionally, **345Trz** and **245Trz** spectra were recorded as a function of temperature and laser power (see fig. 6.5 and A.6).

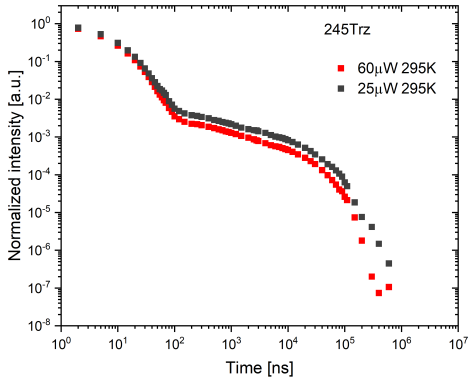

(a) Power-dependent TRPL measurement of **245Trz**.

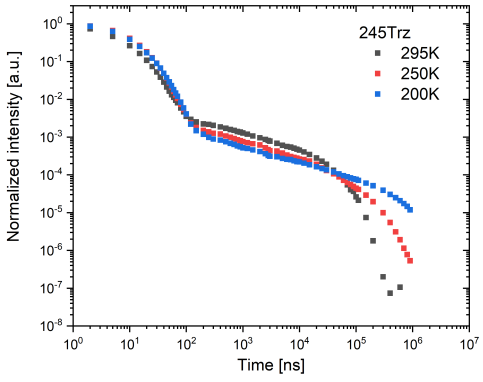

(b) Temperature-dependent TRPL measurement of **245Trz**.

Figure 6.5: Temperature- and power-dependent TRPL measurements of **245Trz**.

In Figure 6.5a the power-dependent measurement of **245Trz** is displayed and a power dependence can be observed. The power dependence for the prompt emission indicates that a singlet-singlet annihilation (SSA) processes takes place and the power dependence for the delayed emission indicates that a triplet-triplet annihilation (TTA) processes takes place. Since the power dependence is significantly lower for the prompt emission and higher for the delayed part the number of TTA processes is much higher than for SSA processes. From the temperature dependent measurements of **345Trz** (see fig. A.6b) and **245Trz** (see fig. 6.5b) it can be observed that for both compounds TADF processes are happening, since the intensity for the delayed part decreases with decreasing temperature. Furthermore, the intensity at the long living regime

(phosphorescence) increases with decreasing temperature which indicates a reduced RISC and stronger phosphorescence. By fitting the prompt and delayed decay to two separate exponential (either mono- or biexponential) decay curves (see fig. A.5 in Appendix), the prompt and delayed fluorescence lifetimes were derived (see tab. 6.3). **345Trz**, **234Trz** and **245Trz** show similar prompt lifetimes with 15–18 ns. Regarding the delayed lifetime **345Trz** and **245Trz** show similar values, while **234Trz** shows a very short delayed lifetime of only 5 μs.

Table 6.3: Prompt and delayed fluorescence lifetime of compounds **345Trz**, **234Trz** and **245Trz**.

compound	**345Trz**	**234Trz**	**245Trz**
t_{prompt} [ns]	17	18	15
$t_{delayed}$ [μs]	10	5	9

6.4 Device characteristics

In order to determine the electronic properties, such as charge transport properties and trap density of hole or electron traps, single-carrier devices (HO and EO) were fabricated. The exact fabrication procedure can be found in Chapter 10. The architectures of the HO and EO devices is displayed in Figure 4.4 in Chapter 4.3. For a balanced emitter, electron and hole mobility and trap density of electron and hole traps (with the same trap depth) would be in the same order of magnitude. In a single-layer OLED with a balanced emitter holes and electrons recombine in the center of the emitting layer. This has several advantages for a single-layer OLED architecture, since no additional electron- and/or hole-transport layers would be required. In Figure 6.6 the measured current density is plotted against voltage for both EO and HO devices of the four compounds. Here the data points represent the measured values, whereas the lines represent fits obtained from drift-diffusion simulations employing the extended Gaussian disorder model (further information about the model can be found in ref. [38]).

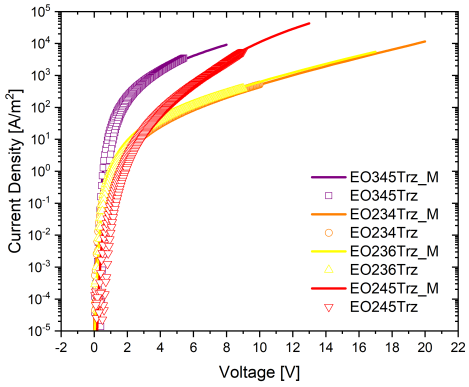

(a) Experimental (dots) and fitted (lines) data for EO devices of **345Trz**, **234Trz**, **236Trz** and **245Trz**.

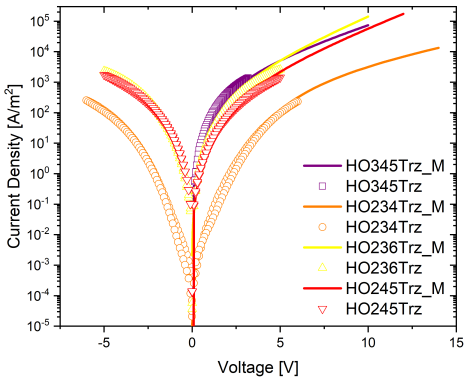

(b) Experimental (dots) and fitted (lines) data for HO devices of **345Trz**, **234Trz**, **236Trz** and **245Trz**.

Figure 6.6: Experimental (dots) and fitted (lines) single-carrier device data of **345Trz**, **234Trz**, **236Trz** and **245Trz**.

The fitting of the single-carrier devices showed that there are only minor differences between all four compounds in terms of charge transport (see tab. 6.4). The hole mobility μ^h is quite similar for all four compounds, with **345Trz** showing the lowest and **234Trz** the highest value. Regarding the electron mobility μ^e **345Trz** and **245Trz** are showing significantly increased values compared to **234Trz** and **236Trz**. The hole trap density P_t again was similar, with only **236trz** showing an increased value. **345Trz**, **234Trz** and **236Trz** are showing a similar electron trap density N_t, whereas **245Trz** shows an increased value. So for **245Trz** the electron transport is more trapped than the hole transport. For **345Trz** and **236Trz** the density of electron and hole traps is balanced, while for **236Trz** the the hole transport is is more trapped.

Table 6.4: Input and fitting results for the fitting of single-carrier devices of **345Trz**, **234Trz**, **236Trz** and **245Trz** with an EDGM model.

compound		**345Trz**	**234Trz**	**236Trz**	**245Trz**
HO thickness	[nm]	100	140	85	140
hole mobility μ^h	$[m^2 \cdot (Vs)^{-1}]$	$6.4 \cdot 10^{-11}$	$3.4 \cdot 10^{-10}$	$1.6 \cdot 10^{-10}$	$1.6 \cdot 10^{-10}$
zero field mobility holes μ_0^h	$[m^2 \cdot (Vs)^{-1}]$	$8.0 \cdot 10^{4}$	$1.1 \cdot 10^{4}$	$1.2 \cdot 10^{4}$	$3.0 \cdot 10^{4}$
lattice constant holes α_h	[nm]	1.4	1.4	1.4	2.5
width of Gaussian DOS σ_h	[eV]	0.150	0.130	0.135	0.140
hole trap density P_t	$[m^{-3}]$	$1.5 \cdot 10^{22}$	$8.5 \cdot 10^{22}$	$1.0 \cdot 10^{23}$	$8.0 \cdot 10^{22}$
hole trap depth $E_{p\ gauss}$	[eV]	0.60	0.40	0.50	0.60
EO thickness	[nm]	118	123	136	86
electron mobility μ^e	$[m^2 \cdot (Vs)^{-1}]$	$4.2 \cdot 10^{-9}$	$1.3 \cdot 10^{-11}$	$3.1 \cdot 10^{-11}$	$2.8 \cdot 10^{-9}$
zero field mobility electrons μ_0^e	$[m^2 \cdot (Vs)^{-1}]$	$1.5 \cdot 10^{2}$	$1.0 \cdot 10^{3}$	$1.0 \cdot 10^{3}$	$1.0 \cdot 10^{2}$
lattice constant electrons α_e	[nm]	1.3	1.2	1.3	1.1
width of Gaussian DOS σ_e	[eV]	0.100	0.135	0.130	0.100
electron trap density N_t	$[m^{-3}]$	$1.4 \cdot 10^{22}$	$3.0 \cdot 10^{22}$	$1.0 \cdot 10^{22}$	$1.1 \cdot 10^{24}$
electron trap depth $E_{n\ gauss}$	[eV]	0.50	0.62	0.65	0.38

Furthermore, all the devices were modelled with a thickness scaling for the active layer of 140 nm and these data sets are in shown in fig. 6.7. For the electron-only devices with the same thickness it can be observed that **234Trz** and **236Trz** show similar current densities at the same voltage. By comparing them to the curve for **345Trz** it can be observed that they have a similar electron trap density but a lower electron mobility. **245Trz** shows the highest current of all four compounds.

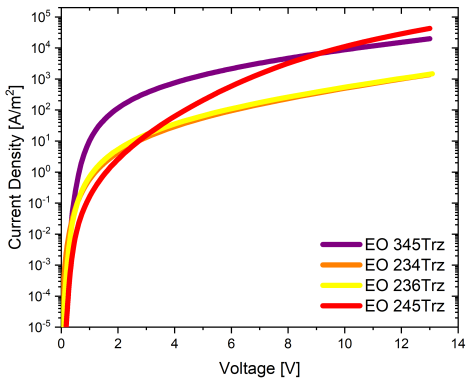

(a) Modelled data for EO devices with a thickness of 140 nm of **345Trz**, **234Trz**, **236Trz** and **245Trz**.

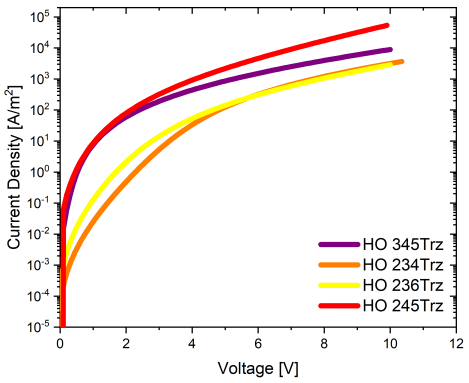

(b) Modelled data for EO devices with a thickness of 140 nm of **345Trz**, **234Trz**, **236Trz** and **245Trz**.

Figure 6.7: Modelled single-carrier device data of devices scaled to a thickness of 140 nm of **345Trz**, **234Trz**, **236Trz** and **245Trz**.

Regarding the hole-only devices the curves of **234Trz** and **236Trz** are again quite similar while

this time they are comparable to the curve of **245Trz** which seems to have a similar hole trap density but a higher hole mobility.
By comparing the hole with the electron current for each of the compounds it is possible to determine how balanced the charge transport is for each compound. The comparisons for all compounds are shown in fig. 6.8. It can be observed that **345Trz** is very balanced in terms of charge transport. Closest to that is **245Trz** for which hole and electron current are trending towards each other for increasing voltage. For compounds **234Trz** and **236Trz** the opposite trend can be observed, here electron and hole current are drifting apart from each other with increasing voltage. For all three asymmetric compounds the hole current is higher than the electron current. The reason for that is a combination of a higher electron trap density than hole trap density and/or a higher hole mobility than electron mobility in the compound.

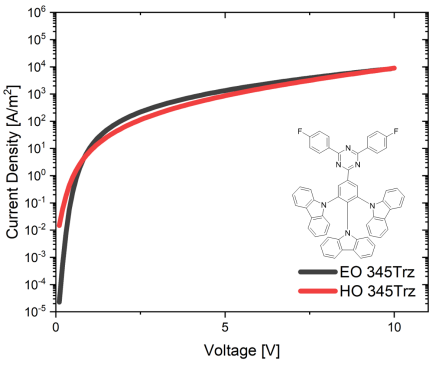

(a) Modelled HO (red) and EO (grey) device data of **345Trz**.

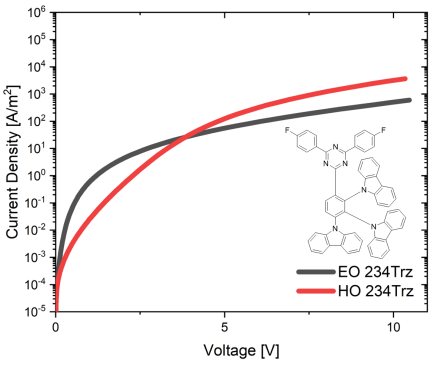

(b) Modelled HO (red) and EO (grey) device data of **234Trz**.

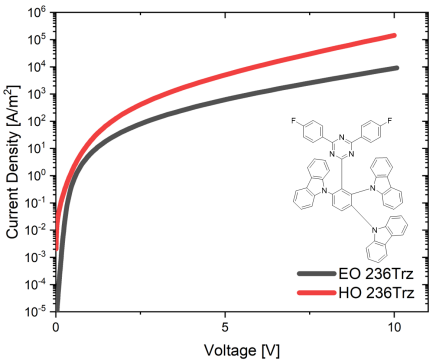

(c) Modelled HO (red) and EO (grey) device data of **236Trz**.

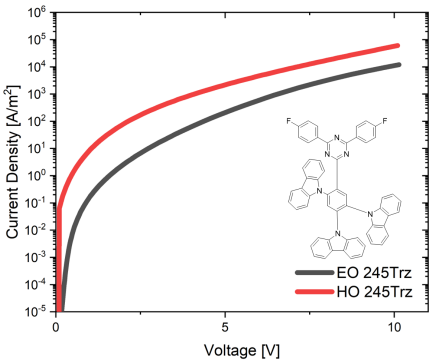

(d) Modelled HO (red) and EO (grey) device data of **245Trz**.

Figure 6.8: Comparison of modelled HO (red) with modelled EO (grey) device data in order to make differences in charge transport visible.

6.5 Summary and conclusions

In order to investigate the effect of the position of the carbazole donor units on the photophysical and charge transport properties of a carbazole-triazine donor-acceptor system, three asymmetric and one symmetric compound have been designed, synthesized, investigated and compared. Starting by the synthesis where a different synthetis route was necessary to derive the three asymmetric compounds compared to the symmetric **345trz**. DFT calculations of the HOMO and LUMO levels showed that only minor differences between the compounds arise by changing the arrangement of the donor building blocks. These minor differences have been confirmed by experimental data. By comparing the calculated HOMO and LUMO, it can be seen that for **234Trz** and **236Trz** the HOMO-LUMO overlap is larger, than for **345Trz** and **245Trz**. Regarding the calculated singlet and triplet energy levels some deviations can be observed. **245Trz** shows a higher S_1 level than found for the other three compounds. For the triplet levels the numbers have a distribution from 2.52–2.66 eV. Interestingly the energy gap ΔE_{ST} between S_1 and T_1 is for the symmetric compound by far the highest and for **234Trz** the lowest. **345Trz** shows a red-shifted lowest energy transition in UV-Vis, compared to the asymmetric compounds. For the three asymmetric compounds the absorption spectra were similar. In terms of fluorescence, **234Trz** and **236Trz** show a green emission , while **345Trz** and **245Trz** appear to have a sky-blue emission. Further, the two green-emitting compounds **234Trz** and **236Trz** show a significantly increased PLQY with over 50% compared to **345Trz** and **245Trz**. TRPL showed that the prompt fluorescence lifetimes are similar for **345Trz**, **234Trz** and **245Trz**, whereas the delayed lifetime of **234Trz** is shortest for the three compounds. Considering the above, it seems like **234Trz** shows a higer RISC rate and a higher PLQY than the other compounds, which in theory makes it the most efficient emitter of the compared compounds. Regarding the charge transport properties, only the symmetric **345Trz** shows a balanced charge transport, whereas the three asymmetric compounds show higher hole currents compared to electron currents. Overall, **234Trz** and **236Trz** have similar photophysical and charge transport properties while **345Trz** and **245Trz** differ from that but show many similarities to each other. This is an indicator that the arrangement of the carbazole units has an effect on various photophysical and charge transport properties, whereby the symmetric pattern seems to be most favorable.

7 Acceptor-Donor-Acceptor structure 4Cz2Trz

Within this section a by calculations predicted structure built up from two triazine acceptor groups and four carbazole donor groups will be discussed, in order to see which impact the number of acceptor groups has on photophysical properties, as well as charge transport properties.

7.1 Theoretical calculations

In order to predict whether a molecule fulfills the prerequisites to be a TADF emitter, theoretical calculations on the basis of DFT method are performed. For **4Cz2Trz** a geometric optimization on a ωB97XD* level were performed in order to receive an optimized structure. From this structure it is possible to calculate the HOMO and LUMO level of **4Cz2Trz** which are shown in Table 7.1.

Table 7.1: Theorethically calculated energy levels for **4Cz2Trz**.

compound		**4Cz2Trz**
HOMO calc.[a]	[eV]	-5.76
LUMO calc.[a]	[eV]	-1.91
S_1[a]	[eV]	2.82
T_1[a]	[eV]	2.72
ΔE_{ST}	[eV]	0.10

[a] Calculated based on a TD-DFT approach at a ωB97XD*/6–311G level.

Further calculations with a TD-DFT approach give us the energies of the lowest excited singlet state S_1 and the lowest excited triplet state T_1, which can be used to calculate firstly the energy gap ΔE_{ST} and secondly the expected emission wavelength. For the ΔE_{ST} a value of 0.10 eV is calculated. This quite small energy gap is an important prerequisite for TADF. Furthermore, the S_1 level at 2.82 eV indicates a deep blue fluorescence around 440 nm. Additionally, the calculated HOMO level is within the trap-free window (see Chapter 4.6), what indicates a trap-free hole transport, while the LUMO level is outside the trap-free window, meaning that electron transport is expected to be trap-limited. In fig. 7.1 the calculated spatial distribution of the HOMO and LUMO on an optimized structure of **4Cz2Trz** is displayed. It can be seen that the HOMO is located on the four carbazole donor units and that they all contribute to the donor characteristics. The LUMO is distributed on the triazine acceptor units but seems to exhibit some overlap with the HOMO.

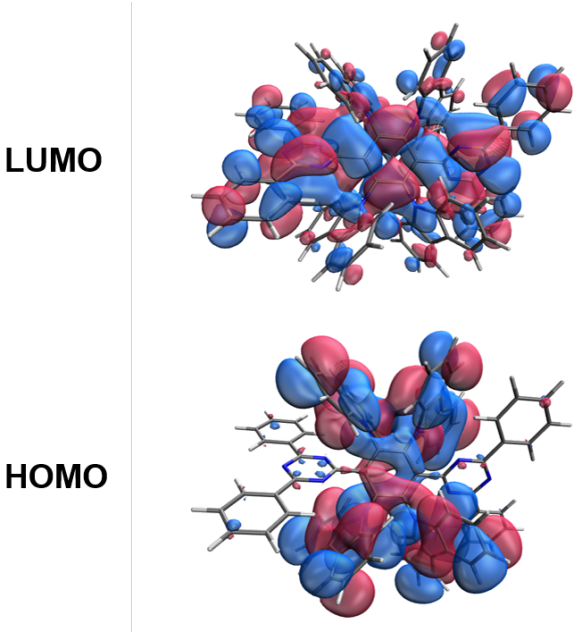

Figure 7.1: Calculated HOMO and LUMO distributions on optimized structure of **4Cz2Trz**.

7.2 Synthesis and characterization

The synthesis of **4Cz2Trz** took place in two steps and is shown in Scheme 7.1. In a first step the two aldehyde groups of 2,3,5,6-tetrafluoroterephthalaldehyde were converted into diphenyl triazine groups to give 6,6'-(perfluoro-1,4-phenylene)bis(2,4-diphenyl-1,3,5-triazine) **4F2Trz** via a ring closure reaction. In a second step, which represents a nucleophilic aromatic substitution of the four fluoride atoms by four carbazole donor units, the desired A-D-A structure 9,9',9",9"'-(3,6-bis(4,6-diphenyl-1,3,5-triazin-2-yl)benzene-1,2,4,5-tetrayl)- tetrakis(9*H*-carbazole) **4Cz2Trz** was obtained.

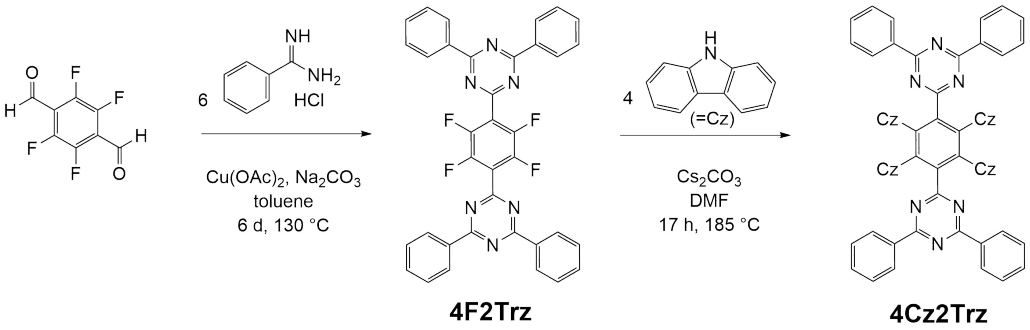

Scheme 7.1: Synthesis of **4Cz2Trz** via two step reaction.

7.3 Summary and conclusions

The calculations are promising in the sense that they predict a blue emitter with a low energy gap between singlet and triplet state (ΔE_{ST}) and small overlap between HOMO and LUMO. Furthermore, the synthesis of **4Cz2Trz** was succesful. Unfortuanely, due to the low solubility no films could be prepared for photophysical characterization. Moreover, **4Cz2Trz** began to decompose under sublimation or evaporation conditions (high vacuum and heating). Therefore the preparation of solid state samples for photophysical investigations as well as device fabrication for single-carrier devices or OLED devices was not possible.

8 5,10-Bis(4-(3,6-di-*tert*-butyl-9*H*-carbazol-9-yl)-2,6-dimethyl-phenyl)-5,10-dihydroboranthrene tBuCzDBA

Within this section the synthesis, photophysical investigations and device characteristics of a derivative of the well-known emitter 5,10-Bis(4-(9*H*-carbazol-9-yl)-2,6-dimethylphenyl)-5,10-dihydroboranthrene (**CzDBA**) with attached *tert*-butyl groups in order to increase solubility, will be discussed. In order to see which impact the introduction of *tert*-butyl groups has on charge transport properties a comparison to **CzDBA** will be made.

8.1 Synthesis and characterization

In a first step the donor building block 9-(4-bromo-3,5-dimethylphenyl)-3,6-di-*tert*-butyl-9*H*-carbazole (**tBuCz**) was synthesized with a nucleophilic aromatic substitution of iodide by *tert*-butyl carbazole on 2-bromo-5-iodo-1,3-dimethylbenzene (see Scheme 8.1). In order to receive 5,10-dibromo-5,10-dihydroboranthrene (**DBA**), precursor of the 5,10-dihydroboranthrene acceptor building block (see Scheme 8.2) 1,2-bis(trimethylsilyl)-benzene and tribromoborate where heated and stirred under reduced pressure for 5 days.

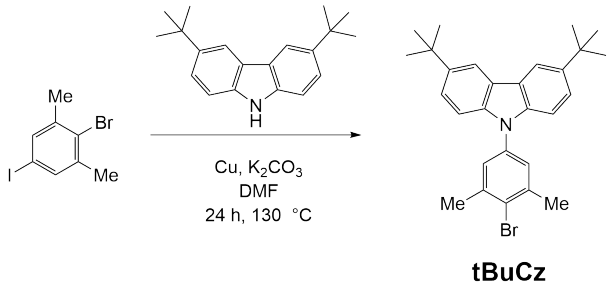

Scheme 8.1: Synthesis of *tert*-butyl carbazole donor compound **tBuCz**.

In a second flask **tBuCz** was converted into the corresponding lithium species by addition of *n*-BuLi. **DBA** was slowly transferred into the solution of the lithium organyl to give 5,10-bis(4-(3,6-di-*tert*-butyl-9*H*-carbazol-9-yl)-2,6-dimethyl-phenyl)-5,10-dihydroboranthrene (**tBuCzDBA**).

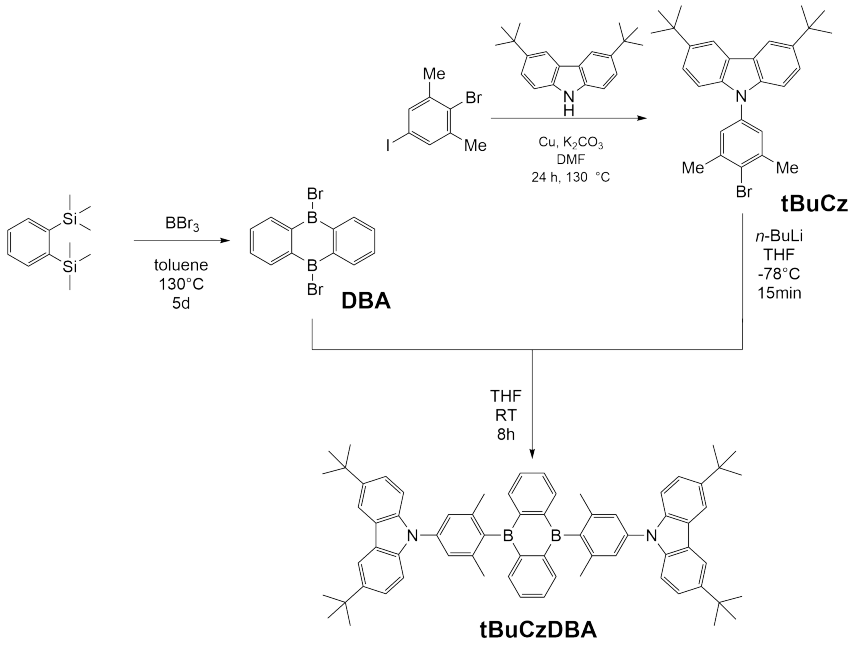

Scheme 8.2: Synthesis of **tBuCzDBA** via two step reaction.

8.2 Theorethical calculations

DFT-calculations have been performed for **tBuCzDBA** to determine the HOMO and LUMO levels, as well as the singlet S_1 and triplet T_1 levels and the resulting energy gap (ΔE_{ST}). The results of the calculations are displayed in Table 8.1. In fig. 8.1 the HOMO and LUMO

Table 8.1: Determined energy levels for **tBuCzDBA**.

compound		**tBuCzDBA**	**CzDBA**
HOMO calc.[b]	[eV]	-5.75	-5.83
HOMO exp.[a]	[eV]	-5.88	-5.93
LUMO calc.[b]	[eV]	-2.20	-2.40
LUMO exp.[a]	[eV]	-3.49	-3.45
S_1 calc.[b]	[eV]	2.651	2.770
S_1 exp.[a]	[eV]	2.486	2.629
T_1 calc.[b]	[eV]	2.625	2.731
T_1 exp.[a]	[eV]	2.464	2.596
ΔE_{ST} calc.[b]	[eV]	0.026	0.039
ΔE_{ST} exp.[a]	[eV]	0.022	0.033

[a] Experimental energy levels taken from literature [39].
[b] Calculated based on a TD-DFT approach at a BMK/6–31G* level.

distributions on an optimized structure of **tBuCzDBA** are shown. A small HOMO-LUMO overlap can be noticed. A small overlap of HOMO and LUMO has been connected to a low energy gap ΔE_{ST} between singlet S_1 and triplet T_1 energy levels (see Chapter 4.4).This is also confirmed by the calculated singlet and triplet energy levels and the resulting ΔE_{ST} of 0.026 eV.

The calculated S_1 energy level of 2.651 eV leads to a calculated fluorescence wavelength of around 470 nm. Comparing the calculated energy levels of **tBuCzDBA** and **CzDBA**, it is noticeable that the *tert*-butyl groups do not seem to have a great influence on the position of these levels. Thus, the difference with respect to the calculated HOMO levels is 0.08 eV. For the calculated LUMO levels the difference is 0.20 eV. For the calculated excited singlet and triplet

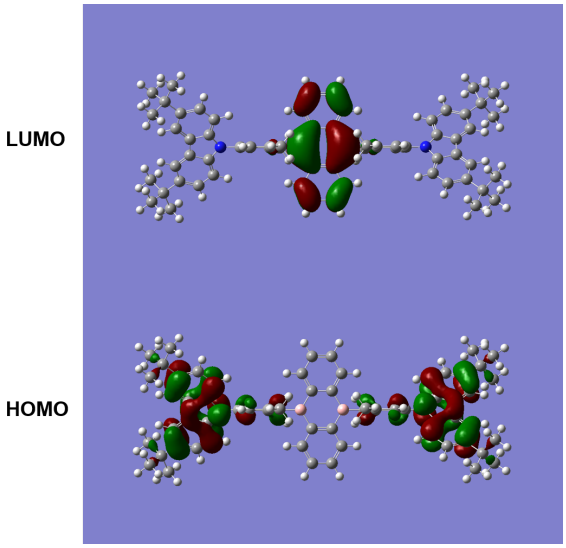

Figure 8.1: Calculated HOMO and LUMO distributions on optimized structure of **tBuCzDBA**.

states **CzDBA** exhibit by around 0.1 eV higher values than **tBuCzDBA**, meaning the expected fluorescence of **CzDBA** is blue-shifted by about 20 nm. The difference between the calculated energy gaps ΔE_{ST} is only 0.01 eV, meaning that both **tBuCzDBA** and **CzDBA** are showing promising properties for TADF emitter. Comparing the calculated values for **tBuCzDBA** to experimental values from literature[39] only the calculated LUMO value deviates significantly from the experimentally found values with a difference of 1.3 eV. The reason for this deviation is that the calculated values were determined for vacuum conditions, while the experimental value was determined by subtracting the optical band gap from an ultraviolet photoelectron spectroscopy in atmospheric conditions. The calculated values for singlet and triplet levels and the energy gap between are in well agreement with the experimental values from literature[39], which supports that the *tert*-butyl groups do not have a large influence on the energetic position of the orbitals. If the experimental HOMO and LUMO values from the literature[39] are considered with respect to their position in the trap-free window, it can be observed that for **CzDBA** and **tBuCzDBA** the HOMO values, which are corresponding to the ionization energy with 5.93 eV and 5.88 eV, are within the window with the upper limit of 6 eV[19]. The experimental LUMO values from the literature[39], both for **CzDBA** and **tBuCzDBA** with 3.45 eV and 3.49 eV, are outside the trap-free window with a lower limit of 3.6 eV. Based on the level of the molecular orbitals, one would expect a trap free hole transport, whereas electron transport might be slightly trap limited.

8.3 Photophysical properties

Photophysical characterization was performed using steady state UV-Vis absorption and photoluminescence measurements on thermally evaporated films on quartz substrates (20 × 10 mm) with a thicknesses of 100 nm, as well as solution samples with a concentration of $1{\cdot}10^{-5}$ mol·L^{-1} in dry toluene (see fig. 8.2a and 8.2b). The absorption spectra of the solution and solid state samples are similar, showing a lowest energy transition (LET) at 450 nm and an absorption maximum (Abs$_{max}$) at 348 nm (see Table 8.2).

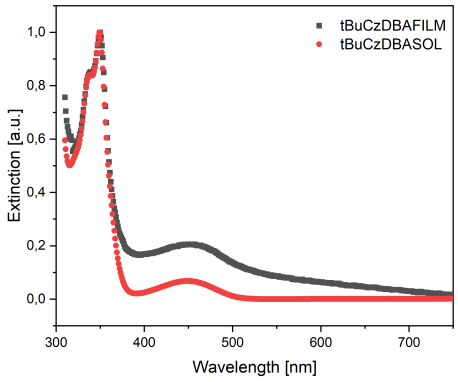

(a) Solution (red) and solid state (grey) UV-Vis spectra of **tBuCzDBA**.

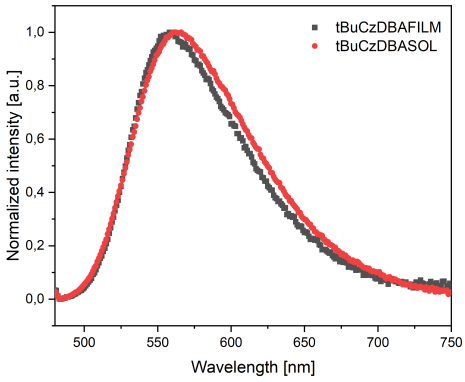

(b) Solution (red) and solid state (grey) emission spectra of **tBuCzDBA**.

Figure 8.2: Solution and solid state UV-Vis and emission spectra of **tBuCzDBA**; solutions were prepared with a concentration of $1{\cdot}10^{5}$ mol·L^{-1} in dry toluene; solid state samples were prepared by thermal evaporation on quartz substrates.

The baseline of the spectrum of the solid film seems to be tilted somewhat (resulting in a perhaps spurious red-shift of the lowest absorption band), which may point to an minor instrumental or measurement artifact. The emission spectrum of the solid state sample shows a maximum (Em$_{max}$) at 558 nm, whereas the solution sample shows a red-shifted emission at 563 nm. This small red-shift seems to be accompanied by a slightly broadened signal and might have to do with a minor difference in the ratio of vibronic contributions. The photoluminescence quantum yields (PLQY) were measured using an integration sphere filled with nitrogen. The dilute solution sample shows a value of 41%, which is exceeded by that of the solid film which exhibits a PLQY >90%. The high film PLQY is a promising indicator for an efficient emitter and testifies a low self-quenching. In literature **tBuCzDBA** is reported to show a lower PLQY of 84%[39] for a pristine film, this difference may arise due to the fact that the integration sphere in the literature was filled with air instead of nitrogen. Nevertheless, the value in literature supports low self-quenching. Further **CzDBA** shows a high pristine film PLQY of 91% in literature[39], but this value could again be exceeded by a nitrogen atmosphere in the integration sphere. By comparing the film PLQY values from literature it can be observed, that **tBuCzDBA** shows a slightly increased self-quenching compared to **CzDBA**. Therefore it seems like the *tert*-butyl

groups are responsible for increasing self-quenching in **tBuCzDBA**.

Table 8.2: PLQY for diluted solution and solid state samples of **tBuCzDBA**.

sample	LET [nm]	Abs_{max} [nm]	Em_{max} [nm]	PLQY [%]
Film[a]	450	348	558	>90
Solution[b]	450	348	563	41

[a] Thermally evaporated film (100nm) on a quartz substrate.
[b] Solution with a concentration of $1 \cdot 10^{-5}$ mol·L^{-1} in dry toluene.

8.4 Device characteristics

To determine electron and hole transport properties of **tBuCzDBA**, a set of HO and EO devices has been fabricated. The architecture of both devices has been given in Chapter 4.3. In order to ensure that the active layer in both EO and HO devices had the same thickness (155 nm), they were produced simultaneously and the active layer was evaporated in the same evaporator at the same time. In fig. 8.3 the measured current (symbols) is displayed as a function of voltage, together with fits (lines) to a drift-diffusion model employing the extended Gaussian disorder model (further information about the model can be found in ref. [38]).

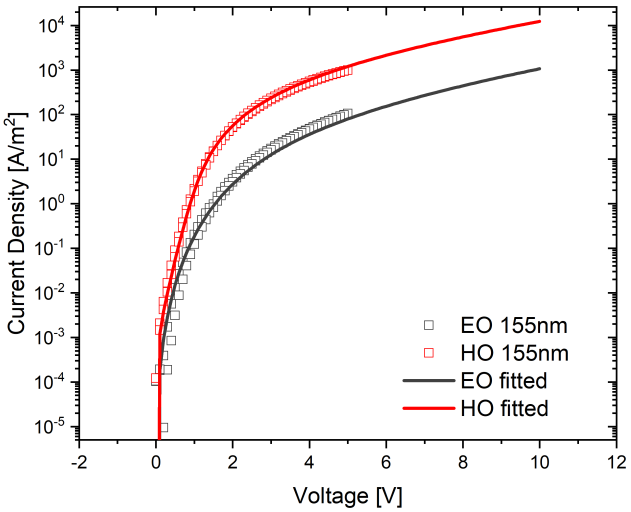

Figure 8.3: Comparison of single-carrier device data derived by measurement (dots) and fitting (lines).

The hole current (red) is one order of magnitude higher than the electron current (grey). It is interesting to compare **tBuCzDBA** to **CzDBA**, because for **CzDBA** a balanced charge transport has been shown[16]. So the *tert*-butyl groups on the carbazole seem to either advance the hole transport or inhibit the electron transport somewhat. From the fitting, we have obtained the transport parameters (see Table 8.3). The electron mobility μ^e for **tBuCzDBA** is lower than for **CzDBA**, while the hole mobilities μ^h for both compounds are similar. Furthermore, the electron trap density N_t is higher for **tBuCzDBA**, so not only the electron mobility is lower for **tBuCzDBA** but also the electron transport suffers more from trapping. These results are in good agreement with the experimental determined HOMO and LUMO levels from literature[39] and their position relative to the postulated trap free window[19]. It seems the introduction of the *tert*-butyl groups is responsible for lowering the electron mobility, as well as for increasing the electron trap density. The origin of the electron traps remains uncertain, but they could be related to morphological features, impurities, synthesis, or even universal water and oxygen-traps, another possible explanation could be a higher disorder in the film, possibly associated with a decrease in density due to the additional alkyl fraction imparted by the *tert*-butyl groups.

Table 8.3: Input and fitting results for the fitting of single-carrier devices of **tBuCzDBA** and **CzDBA** with an EDGM model.

compound		**tBuCzDBA**	**CzDBA**[a]
hole mobility μ^h	$[m^2 \cdot (Vs)^{-1}]$	$1.8 \cdot 10^{-9}$	$3.0 \cdot 10^{-9}$
electron mobility μ^e	$[m^2 \cdot (Vs)^{-1}]$	$2.3 \cdot 10^{-10}$	$5.0 \cdot 10^{-9}$
zero field mobility holes μ_0^h	$[m^2 \cdot (Vs)^{-1}]$	$5.5 \cdot 10^{3}$	$2.0 \cdot 10^{4}$
zero field mobility electrons μ_0^e	$[m^2 \cdot (Vs)^{-1}]$	$7.0 \cdot 10^{2}$	$5.0 \cdot 10^{3}$
lattice constant holes α_h	[nm]	1.7	1.3
lattice constant electrons α_e	[nm]	1.8	1.5
width of Gaussian DOS σ_h	[eV]	0.115	0.135
width of Gaussian DOS σ_e	[eV]	0.115	0.115
hole trap density P_t	$[m^{-3}]$	$2.7 \cdot 10^{22}$	$1.7 \cdot 10^{22}$
electron trap density N_t	$[m^{-3}]$	$4.0 \cdot 10^{23}$	$1.4 \cdot 10^{22}$
hole trap depth $E_{p\ gauss}$	[eV]	0.78	0.65
electron trap depth $E_{n\ gauss}$	[eV]	0.26	0.65

[a] Fitting input and results for **CzDBA** taken from reference [40].

In order to determine the performance in actual OLEDs, four device architectures have been fabricated and studied. As a starting point, the conventional single-layer architecture with an evaporated EML has been chosen. In fig. 8.4 the conventional architecture of a single-layer OLED is displayed. It consists of an ITO substrate as bottom electrode, a spin-coated layer of PEDOT:PSS, an evaporated layer of MoO_3, followed by a thin evaporated layer of C_{60} and an evaporated layer of **tBuCzDBA**. On top a thin layer of the electron transport material TPBi, followed by the Ba/Al cathode was evaporated.

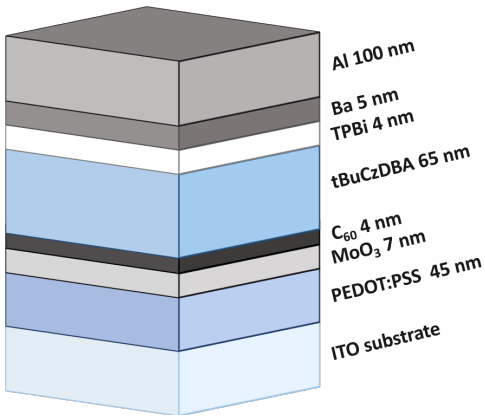

Figure 8.4: Device architecture of a conventional single-layer OLED of **tBuCzDBA**.

The measurements were performed by a scan of a set voltage regime, while the resulting current was measured. The light output was determined with a calibrated Si photodiode, which was placed close to the area of the OLED that was measured. All measurements were carried out in a nitrogen-filled glove box in order to avoid any oxygen or water quenching. In fig. 8.5a the current density against voltage is displayed. Different regimes can be discerned. In the low voltage regime (leakage regime) the measured current is a leakage current. This current has a linear dependence to voltage and has a weak temperature dependence. After the leakage regime the diffusion regime ($V<V_{bi}$) shows an exponential dependence on voltage. In this regime the current exhibits a significant temperature dependence, which is caused by the the dependence of the electric current density in a diode on the saturation current density J_0 and the ideality factor η as described by the Shockley diode equation (see Chapter 4.6). After the built-in voltage ($V_{bi} \approx 2.1$ V) is exceeded a flattening of the current can be observed (drift regime). Here the current becomes space charge limited. In fig. 8.5b the luminance is displayed against voltage. This plot shows the onset of emission to coincide with the point where the built-in voltage is exceeded. The light output or luminance decreases with temperature, which is expected, since a lower current gives less excitons and therefore a suppressed emission.

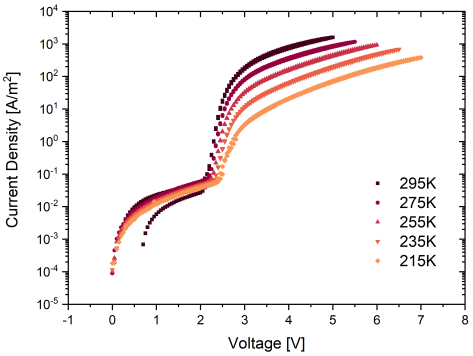

(a) Current density against voltage plot for a thermal scan of a conventional single-layer OLED architecture of **tBuCzDBA**.

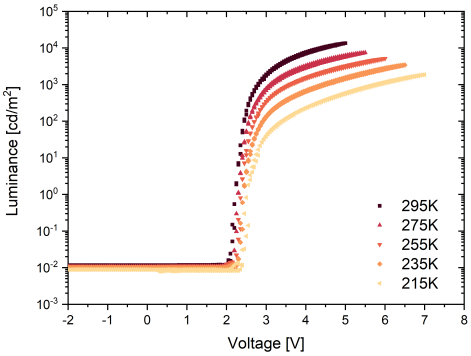

(b) Luminance against voltage plot for a thermal scan of a conventional single-layer OLED architecture of **tBuCzDBA**.

Figure 8.5: Current density and luminance plots against voltage of a thermal scan of a conventional single-layer OLED architecture of **tBuCzDBA**.

In order to calculate the external quantum efficiency (EQE), in addition to the measured current density and photocurrent, an electroluminescence spectrum is necessary to determine the wavelength of the emitted photons. The EQE represents a common benchmark for light-emitting materials in order to compare their performance in OLED devices[41] and is further described in Chapter 4.4. The electroluminescence spectrum was measured with a USB4000-UV-Vis-ES spectrometer and is displayed in fig. 8.6, here the emission reaches a maximum at a wavelength of 556 nm.

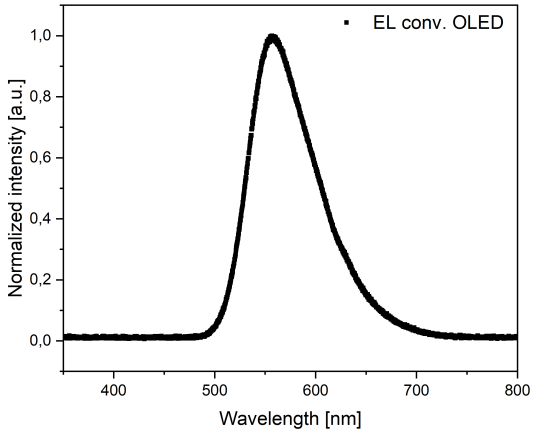

Figure 8.6: Elelctroluminescence spectrum of a **tBuCzDBA** OLED device with conventional architecture.

Afterwards, the EQE value for every data point was calculated and plotted against the luminance in fig. 8.7. For the conventional architecture **tBuCzDBA** reaches a maximum EQE of

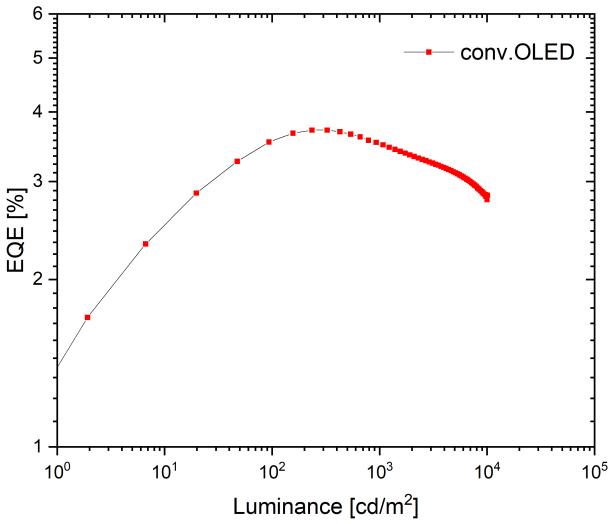

Figure 8.7: External quantum efficiency (EQE) of a single-layer OLED of **tBuCzDBA** with conventional architecture.

4% which is quite low compared to the 19% EQE published for **CzDBA** with a similar device architecture[28]. This difference may be partly due to the unbalanced charge transport within the **tBuCzDBA** layer which leads to a shift of the recombination zone towards the top electrode (cathode), which causes enhanced cathode quenching (see Chapter 4.6). Additionally, the position of the recombination profile has an influence on several modes within the device, such as waveguide mode, the substrate mode and the air mode. Since every interface in the device has a difference in refractive index and is therefore angular dependent, the outcoupling changes with the distance from the recombination zone to the interface. Recent investigations in our group have shown, that the outcoupling efficiency is influenced by the distance of the recombination zone to the cathode (further reading ref. [27]).

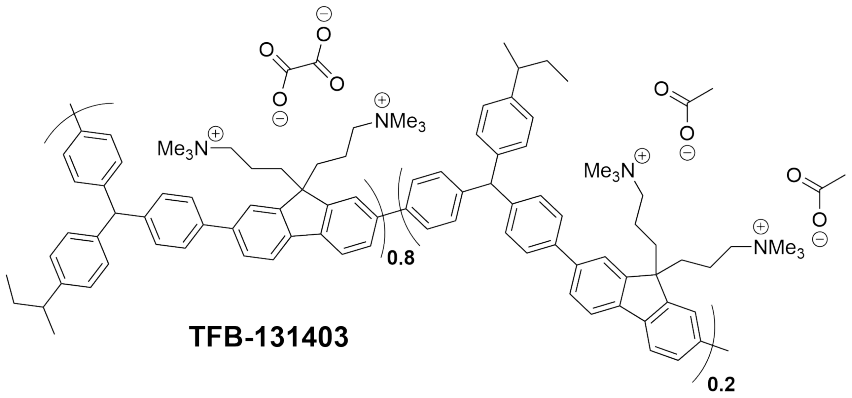

Figure 8.8: Chemical structure of n-doped polymer **TFB-131403**.

Since this shift of the recombination causes multiple processes which are responsible for decreasing the light output. For instance surface plasmon effects at the top metal electrode or the angular dependence of the different modes. In order to reduce the two mentioned light output reducing processes, an inverted OLED architecture has been tested. Within this architecture the electrodes are switched, so electrons get injected from the bottom ITO electrode, while holes get injected from the top Al electrode. Since the recombination zone is now shifted to the bottom electrode the formation of surface plasmons at the top metal electrode should be reduced. Additionally, the path the photons have to travel through the device is shortened. To make this switch possible a n-doped polymer, **TFB-131403** (fig. 8.8) which injects electrons into the LUMO of the EML is necessary.

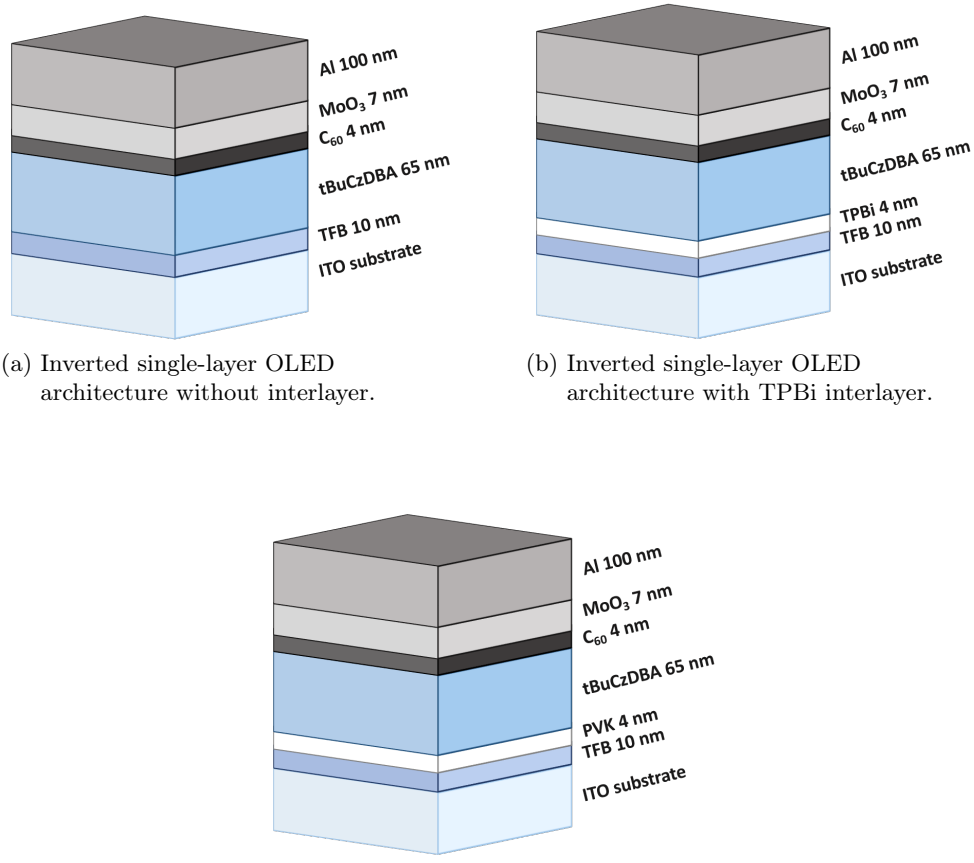

(a) Inverted single-layer OLED architecture without interlayer.

(b) Inverted single-layer OLED architecture with TPBi interlayer.

(c) Inverted single-layer OLED architecture with PVK interlayer.

Figure 8.9: Inverted single-layer OLED architectures; a) inverted single-layer OLED without interlayer;b) inverted single-layer OLED with TPBi interlayer; c)inverted single-layer OLED architecture with PVK interlayer.

The architecture of the inverted OLED is displayed in fig. 8.9a, further on two similar architectures have been tested to determine whether a thin interlayer has an impact in device performance, as it has for the conventional architecture[15]. Therefore in one batch of devices a thin evaporated layer of TBPi has been added on top of the spin-coated **TFB-131403** layer. For a third architecture, an inverted **tBuCzDBA** OLED with a thin spin-coated layer of polyvinylcarbazole (PVK) on top of the **TFB-131403** layer has been studied. Additionally, the **tBuCzDBA** has been spin-coated on top of the PVK layer, in order to get one step closer to the completely solution processed OLED (see fig.8.9b and 8.9c). To ensure comparability, all devices were fabricated with the same **tBuCzDBA** layer thickness (65 nm). All other layers were processed in the same way for all devices.

In fig. 8.10a the current density against voltage and the luminance against voltage plots are shown for all four tested OLED device architectures. In terms of current density, the conventional architecture (red) and the inverted architecture without interlayer (orange) behave similar, whereas the inverted architectures with interlayer show lower current densities at the same voltage. Especially the inverted spin-coated architecture with PVK interlayer (green) shows a significantly reduced current density and an increased leakage current in the lower voltage regime. Comparing the luminance (see fig. 8.10b), three of the four tested architectures show similar maximum luminance values around $1{\cdot}10^4$ cd·m^{-2}. Again the inverted spin-coated architecture PVK interlayer (green) shows a significantly lower value, but this can also be explained by the lower current density at 5 V. Despite a lower current density, the inverted architecture with TPBi interlayer (blue) shows a comparable luminance to the conventional (red) and inverted architecture without an interlayer (orange), which is a first good indication for an efficient OLED.

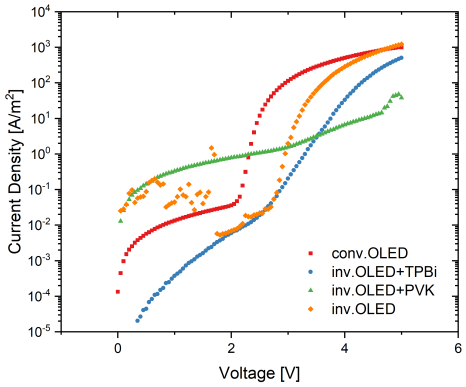

(a) Comparison of the current density of **tBuCzDBA** OLED devices with different architectures.

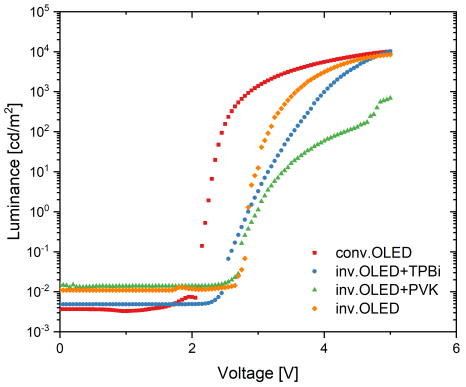

(b) Comparison of the luminance of **tBuCzDBA** OLED devices with different architectures.

Figure 8.10: Comparison of current density and luminance of **tBuCzDBA** OLED devices with different architectures.

The comparison of the EQE values for the four different OLED architectures results that only the inverted architecture with the TPBi interlayer shows a significantly increased maximum EQE of 14% compared to the 4% maximum EQE that were achieved by the three remaining architectures (see fig. 8.11). By comparing the inverted architecture without interlayer to the well-performing one with the TPBi interlayer, it becomes clear that the thin interlayer has a significant effect on the device performance. A possible reason for this could be that the work function of **TFB-131403** does not match with the LUMO of the **tBUCzDBA**, for which reason the thin interlayer enhances charge injection. Furthermore, the comparison of the inverted architectures with interlayers reveals that the PVK interlayer does not enhance device performance, as the TPBi interlayer does. The reason for this difference remains unknown. A possible explanation could be that the PVK layer does not adhere to the **TFB-131403** gets washed away by the next spin-coating step.

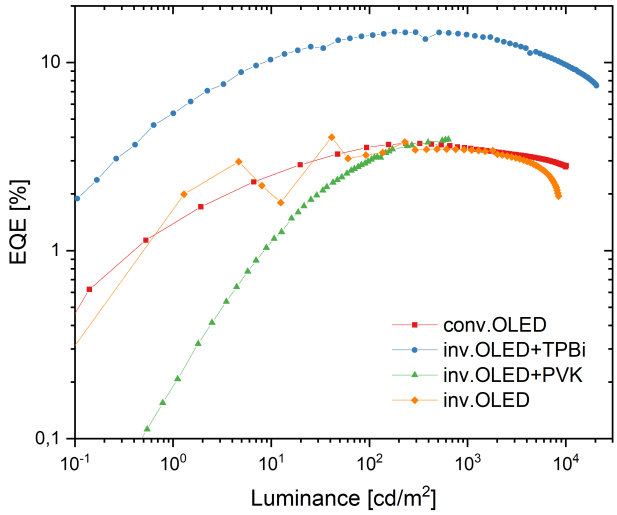

Figure 8.11: Comparison of external quantum efficiencies of **tBuCzDBA** OLED devices with different architectures.

8.5 Summary and conclusions

In order to take a step towards the goal of a solution-processed single-layer OLED, the synthesis and characterization, as well as device incorporation of **tBuCzDBA**, a derivative of well-known emitter **CzDBA** with solubilizing groups attached was performed. Additional to that the impact of the *tert*-butyl groups on the TADF properties of emitters was investigated. DFT calculations have shown that the compound possess a low ΔE_{ST} value which is a necessary prerequisite for an efficient TADF emitter. Furthermore, the HOMO level is within the limits of the trap free window, while the LUMO is very close to the lower limit of the trap-free window. By this a trap-free charge transport, which represents another prerequisite for an efficient emitter, can be predicted. Steady state UV-Vis and PL measurements gave similar spectra for the solid film and solution of **tBuCzDBA**. In contrast, the PLQY of the solid film is more than twice as high as measured in solution. Investigations of the charge transport properties and comparison to **CzDBA** have revealed that the *tert*-butyl groups seem to be responsible for a reduced electron mobility and increased electron trap density in **tBuCzDBA**. A single-layer OLED with conventional architecture has been fabricated and investigated. The comparison with a similar device with **CzDBA** (EQE 19% [28]) as EML, showed a by 15% lower EQE. This difference in device performance may be associated with a less-balanced charge transport within the **tBuCzDBA** layer and therefore reduced light output. To improve the device performance of **tBuCzDBA**, an inverted OLED architecture has been tested in order to shift the recombination zone closer towards the bottom electrode and therefore closer to the surface of the substrate. This inverted OLED has been realized through the use of the n-doped polymer **TFB-131403** that acts as a electron injection layer. The inverted architecture without interlayer resulted in 4% EQE which is no improvement to the conventional device. A reason for the relatively low EQE of could be that the work function of the **TFB-131403** does not match the LUMO level of **tBuCzDBA**. In order to investigate if a thin electron transporting interlayer can improve the device performance in the same way as for the conventional architecture, a 4 nm thick interlayer of TPBi has been added, resulting in an EQE of 14%. The comparison of the conventional device with the inverted architecture with the TPBi interlayer reveals that the latter can enhance the EQE significantly. Replacing the evaporated TPBi interlayer with a spin-coated layer of PVK unfortunately did not work, as the latter probably was washed off during the subsequent spin-coating of **tBuCzDBA**. All in all, we have shown that devices with quite decent performance can be fabricated, based on tBuCzDBA as emitter. Furthermore, the importance of a thin interlayer between the electron injecting leayer (EIL) and the EML has been shown.

9 Outlook

9.1 Comparison of Carbazole$_3$-triazine compounds

In order to gain more information which role symmetry in the donor-acceptor arrangement plays for charge transport and TADF properties, a possible next step would be the synthesis and investigation of a second symmetric regioisomer **246Trz**, which is shown in fig. 9.1. By comparison to the series discussed in this work a possible link between symmetry and various properties could be found. Another interesting resumption of this work would be the fabrication

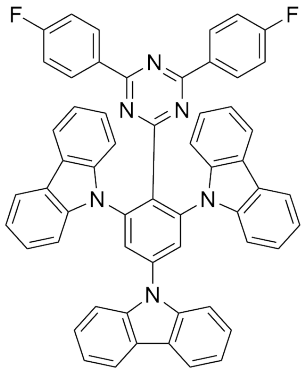

Figure 9.1: Chemical structure of second symmetric regioisomer **246Trz**.

of an OLED of **234Trz**. The compound shows the highest PLQY and the lowest ΔE_{ST} of the series, which are promising photophysical properties for an emitter for good device performance, additional to that, operational lifetimes could be determined.

9.2 Acceptor-Donor-Acceptor structure 4Cz2Trz

Since the synthesis has been successful but no further processing was possible, the introduction of solubility-promoting groups such as methyl or *tert*-butyl groups at the carbazole donor units could be a promising attempt. The resulting structures are displayed in fig. 9.2. With a higher solubility, a proper photophysical characterization would be possible and even solution processed devices could be fabricated. Since theoretical calculations are promising as far as that they have predicted the 4Cz2Trz to be a highly efficient blue TADF emitter, this approach would be very worthwhile.

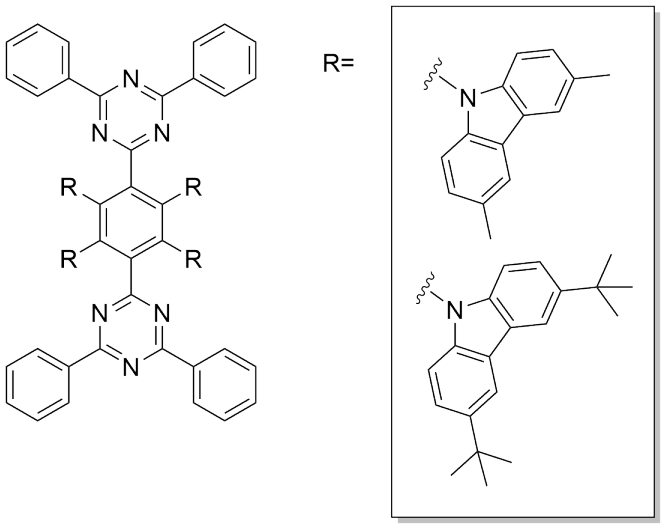

Figure 9.2: Chemical structure of **4Cz2Trz** with attached solubility-promoting groups to carbazole donor units.

9.3 5,10-Bis(4-(3,6-di-*tert*-butyl-9*H*-carbazol-9-yl)-2,6-dimethylphenyl)-5,10-dihydroboranthrene tBuCzDBA

In order to verify the theoretically calculated HOMO and LUMO energy levels, ultraviolet photoelectron spectroscopy (UPS) could be performed to derive an experimental HOMO level and steady state UV/Vis spectroscopy can be used to calculate the optical band gap. By subtraction of the optical band gap from the HOMO an experimental LUMO value can be obtained. By performing TRPL measurements an experimental determination of the S_1 and T_1 and ΔE_{ST} is possible, which also could verify the calculated values for the mentioned energies. Additionally, the determination of rate constants of several intramolecular photophysical processes such as intersystem crossing, fluorescence decay or reverse intersystem crossing is possible. These rate constants would give further insight into electronic properties of the molecule. To continue the development towards an OLED, where every layer except the electrodes is solution-processed, several additional approaches could lead to significant progress. One possbile option is replacing the PEDOT:PSS layer in the conventional structure by a PEDOT:PFI layer[42]. This layer would be able to inject properly into **tBuCzDBA** and makes it possible to waive the MoO_3 and C_{60} Ohmic contact and **tBuCzDBA** could be spin-coated directly on top of PEDOT:PFI. Regarding the inverted structure two further attempts could be made, firstly an approach of spin-coating the TPBi interlayer would be of great interest, since the tested OLED structure with a TPBi interlayer has shown a good device performance. With this approach it also would be possible to study electron transport properties within spin-coated EO devices. Since test for the inverted OLED structure have shown, that without an interlayer between the EIL (**TFB-131403**) the device performance is quite low with 4% EQE, further tests with different thicknesses of a PVK interlayer could be performed in order to match with the device performance of the tested OLED structure with a TPBi interlayer. If a good performing device with a spin-coated EML is

achieved, further improvement may be reached upon diluting **tBuCzDBA** in a polymer matrix in order to reduce concentration quenching. Finally, the thicknesses of the incorporated layers in the devices could be optimized by simulations in order to further enhance the EQE. Additional to that, operational lifetimes could be determined.

10 Experimental procedures

All commercial available chemical and solvents were used without further purification.
THF, DMF, toluene, dioxane, 2,2,2-trifluoroethanol, Cs_2CO_3, Pd(dppf), $Pd[PPh_3]_4$, bis-(pinacolato)diboron, boron-tribromide, benzamidine hydrochloride, C_{60}, TPBi, 4-fluorophenylmagnesium bromide solution and *n*-BuLi solution were purchased by Sigma Aldrich. DCM, *n*-hexane, trifluoro-bromobenzene compounds, K_2CO_3, Na_2CO_3, KOAc, $Cu(II)(OAc)_2$, MoO_3, copper and silica were purchased by Fisher Scientific. 2,2,3,3,4,4,5,5-octafluoro-1-pentanol, trimethyl borate, cyanuric chloride, 2,3,5,6-tetrafluoroterephthalaldehyde, 2-bromo-5-iodo-1,3-dimethylbenzene, 1,2-bis(trimethylsilyl)benzene, 9*H*-carbazole, 3,6-di-*tert*-butyl-9*H*-carbazole, were purchased by TCI. PEDOT:PSS was purchased by Clevios. TFB-131403 n-doped polymer was provided by Organic Nano Device Laboratory, National University of Singapore.
All flasks were put under an argon atmosphere prior to addition of the chemicals and solvents if not stated differently

Theoretical calculations

Theoretical calculations were performed with the software Gaussian 09. The optimization of the ground-state $Carbazole_3$-triazine structure was performed with the DFT method with the B3LYP functional with 6-31G basis set. The S_1 and T_1 energies were calculated based on a TD-DFT approach at a B3LYP/6–31G level. The optimization of the ground-state **4Cz2Trz** structure was performed with the DFT method with the ωB97XD* functional with 6-311G basis set. The S_1 and T_1 energies were calculated based on a TD-DFT approach at a ωB97XD*/6–311G level. The optimization of the ground-state **tBuCzDBA** structure was performed with the DFT method with the BMK functional with 6-31G* basis set. The S_1 and T_1 energies were calculated based on a TD-DFT approach at a BMK/6–31G* level.The distribution of the molecule orbitals was visualized on the Gaussview 5.0 software.

Thin-layer chromatography

For qualitative thin-layer chromatography ALUGRAM® SIL G/UV254 (Macherey-Nagel) plates were used with 0.20 mm of silica oxide on aluminum sheets as the stationary phase. Compounds that are fluorescent under irradiation were detected under irradiation with a UV-lamp at wavelengths of 254 nm or 365 nm.

Column chromatography

As the stationary phase for column chromatography silica gel 60 (size 40 – 63 μm) (Macherey-Nagel) was used. The separations have been performed at room temperature. All solids were placed on the silica gel as dry load.

Mass spectrometry

APCI-MS spectra were measured with an Expression L Compact Mass Spectrometer quadrupole mass spectrometer (Advion). The resulted spectra were processed with the computer program Advion Data Express 4.0.13.8 (Advion). MALDI-TOF MS spectra were measured with a Rapidflex MALDI-TOF/TOF Mass Spectrometer (Bruker). The resulted spectra were processed with the computer program MMASS 5.5.0 (Bruker).

Nuclear magnetic resonance spectroscopy (NMR)

NMR spectra were measured at the Bruker 300 MHZ NMR Spectrometer Avance). The assignments were made with MestReNova 14.1.1 (Mestrelab) and Topspin 3.6.1 (Bruker Biospin GmbH). The respective measuring frequency and the deuterated solvents which where used are displayed in brackets in front of the spectroscopic data. The chemical shifts are in parts per million (ppm) relative to the respective undeleted residual signal of the solvent. The following abbreviations were used to designate the fine structures of the proton signals: s (singlet), d (doublet), t (triplet), q (quartet), dd (doublet of doublet), dt (doublet of triplet), td (triplet of doublet), qd (quartet of doublet), m (multiplet). The coupling constants J are given in Hertz.

Luminescence spectroscopy

To record photoluminescence quantum yields and photoluminescence (PL) spectra, a HORIBA Jobin Yvon Fluorolog-3 spectrofluorometer was used, using FluorEssence software. The solutions studied in the spectrofluorimeter were diluted to maintain the absorbance maximum <0.1.

UV-Vis spectroscopy

The absorption measurements were recorded using a PerkinElmer Lambda 900 UV-VIS-NIR Spectrometer.

Time-resolved photoluminescence spectroscopy

For TRPL measurements the solid state samples were excited at 350 nm with a Ti: sapphire laser (Coherent, Astrella, 1 kHz, 5 mJ, 35 fs) paired with a Coherent OperA optical parametric amplifier. TRPL measurements were performed with a Standford Computer Optics 4 Picos gated-iCCD camera. The spectra were captured using the 4 Spec software from Stanford Computer Optics. The laser beam was focused onto the sample with a spot size of 0.8 mm, to check the focus a Coherent LaserCamHr-II beam profiler was used.

Device fabrication

For all devices the used substrates were cleaned by scrubbing with detergent solution and ultrasonification in acetone and isopropanol followed by drying for 10 min at 140 °C. Furthermore the substrates were treated with UV-ozon for 20 min.

For hole-only devices glass substrates with patterned ITO layer on top were used. After the cleaning a layer of PEDOT:PSS (Clevios PVP AI 4083) (45 nm) was spin-coated on the substrate followed by 10 min annealing at 140 °C. Afterwards, the substrates were transferred into a nitrogen-filled glove box and were kept inside for the rest of the fabrication. First a layer of MoO_3 (7 nm) was evaporated on the substrate followed by a layer of C_{60} (4 nm), a layer of the investigated compound and another C_{60} layer (4 nm). As top contact a layer of MoO_3 (10 nm) and Aluminium (Al) (100 nm) were evaporated. The two MoO_3 and the Al layer were evaporated at a pressure lower than $5 \cdot 10^{-7}$ mbar. The organic layers were evaporated at a pressure of $3 \cdot 10^{-6}$ mbar.

For electron-only devices cleaned glass substrates were transferred to nitrogen-filled glove box. As bottom contact a layer of Al (30 nm) was evaporated and subsequent exposed to air for oxidation for no longer than 5 min before transferring the substrates back in the glove box. As next step, a layer of the investigated compound was evaporated followed by a layer of TPBi (4 nm).

As top contact a layer of Barium (Ba) (5 nm) and Al (100 nm) were evaporated. The Ba and Al layers were were evaporated at a pressure lower than $5 \cdot 10^{-7}$ mbar. The organic layers were evaporated at a pressure of $3 \cdot 10^{-6}$ mbar.
For OLED devices different device structures and therefore fabrication methods were used.
For single-layer evaporated OLEDs glass substrates with patterned ITO layer on top were used. After the cleaning, a layer of PEDOT:PSS (Clevios PVP AI 4083) (45 nm) was spin-coated on the substrate followed by 10 min annealing at 140 °C. Afterwards, the substrates were transferred into a nitrogen-filled glove box and were kept inside for the rest of the fabrication. On the PEDOT:PSS layer a layer of MoO_3 (7 nm) was evaporated. Followed by a layer of C_{60} (4 nm), a layer of the investigated compound and a layer of TPBi (4 nm). As top contact a layer of Ba (5 nm) and Al (100 nm) were evaporated. The Ba, MoO_3 and Al layers were were evaporated at a pressure lower than $5 \cdot 10^{-7}$ mbar. The organic layers were evaporated at a pressure of $3 \cdot 10^{-6}$ mbar.
For single-layer inverted evaporated OLEDs glass substrates with patterned ITO layer on top were used. After the cleaning, the substrates were transferred into a nitrogen-filled glove box and a of layer TFB-131403 (10 nm) was spin-coated on the ITO. Afterwards, either an interlayer of TPBi (4 nm) or directly the compound layer were evaporated.Followed by an evaporated layer of C_{60} (4 nm). As top contact MoO_3 (7 nm) and Al (100 nm) were evaporated. The MoO_3 and the Al layer were evaporated at a pressure lower than $5 \cdot 10^{-7}$ mbar. The organic layers were evaporated at a pressure of $3 \cdot 10^{-6}$ mbar.
For single-layer inverted spin-coated OLEDs glass substrates with patterned ITO layer on top were used. After the cleaning the substrates were transferred into a nitrogen-filled glove box and a layer TFB-131403 (10 nm) was spin-coated on the ITO. On top of the TFB layer an interlayer PVK (4 nm) and the compound layer were spin-coated. On top of the compound layer a layer C_{60} (4 nm) and as top contact MoO_3 (7 nm) and Al (100 nm) were evaporated. The MoO_3 and the Al layer were evaporated at a pressure lower than $5 \cdot 10^{-7}$ mbar. The C_{60} layer was evaporated at a pressure of $3 \cdot 10^{-6}$ mbar.

Device measurements

Electrical characterization measurements were performed in a nitrogen-filled glove box with a Keithley 2400 source meter. For OLEDs the light output was measured with a Si photodiode with NIST-traceable calibration, which was placed close to the area of the OLED which was measured. Electroluminescence spectra were measured with an USB4000-UV-Vis-ES spectrometer.

Spin-coating procedures

PEDOT:PSS (Clevios PVP AI 4083): To receive a 45 nm thick layer, 0.5 mL of the solution were deposited on the substrate and spin-coated 10 sek with 1000 rpm with an acceleration of 1000 rpm·sek^{-1}, followed by 60 sek with 4000 rpm and 1000 rpm·sek^{-1}. Subsequently to the spin-coating the substrates were annealed at 140 °C for 10 min under air.
TFB (TFB-131403 Batch NS4-50): Prior to spin-coating, a solution of TFB-131403 was prepared as follows. TFB-131403 was dissolved in degassed TFE in a nitrogen-filled glove box with a con-

centration of 5.3 mg·mL^{-1} and heated to 50 °C for 15 min. Afterwards, the solution was diluted with OFP until a concentration of 4 mg·mL^{-1} (TFE:OFP 3:1). To receive a 10 nm thick layer 250 μL TFB solution were deposited on the substrate and spin-coated for 60 sek with 6000 rpm and an acceleration of 3000 rpm·sek^{-1}.
PVK: Prior to spin-coating, a 5 mg·mL^{-1} solution of PVK in dry chlorobenzene was prepared inside a nitrogen-filled glove box. To receive a 4 nm thick layer, 250 μL of the solution were deposited on the substrate and spin-coated for 60 sek with 3000 rpm with an acceleration of 2000 rpm·sek^{-1}. Subsequently to the spin-coating the substrates were annealed at 120 °C for 10 min within the glove box.
tBuCzDBA: Prior to spin-coating, a 15 mg·mL^{-1} solution of tBuCzDBA in dry toluene was prepared inside a nitrogen-filled glove box. To receive a 65 nm thick layer, 200 μL of the solution were deposited on the substrate and spin-coated for 60 sek with 2000 rpm with an acceleration of 2000 rpm·sek^{-1}. Subsequently to the spin-coating the substrates were annealed at 110 °C for 10 min within the glove box.
Carbazole$_3$-triazine compounds: Prior to spin-coating, all four compounds were dissolved in dry toluene, but due to different solubility of the four substances different concentrations of the solutions were obtained which are shown in Table 10.1. To receive a 100 nm thick layer, 55 μL of the solutions were deposited on the substrate and spin-coated for 60 sek with 3000 rpm with an acceleration of 2000 rpm·sek^{-1}.

Table 10.1: Concentrations of the solutions used for spin coating the film samples of compounds **345Trz**, **234Trz**, **236Trz** and **245Trz**.

compound	**345Trz**	**234Trz**	**236Trz**	**245Trz**
concentration $[\frac{mg}{mL}]$	25	35	25	20

Chemical structure of EIL and HIL materials

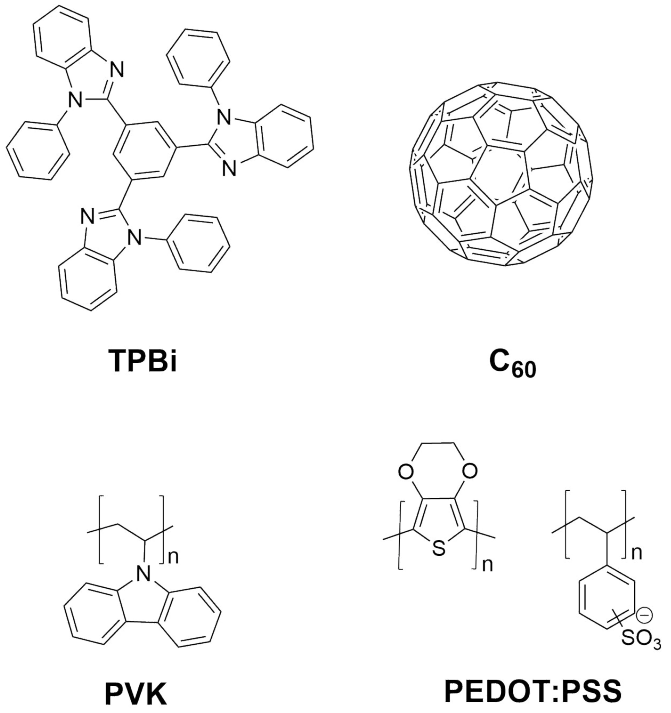

Figure 10.1: Chemical structures EIL and HIL materials used in devices.
Top left: 2,2',2"-(1,3,5-benzinetriyl)-tris(1-phenyl-1-*H*-benzimidazole) **TPBi**; top right: Buckminsterfullerene $\mathbf{C}_{60}$; bottom left: Polyvinylcarbazole **PVK**; bottom right: poly(3,4-ethylenedioxythiophene) polystyrene sulfonate **PEDOT:PSS**.

10.1 Synthesis of 2-chloro-4,6-bis(4-fluorophenyl)-1,3,5-triazine (Trz)

In a two-necked 100 mL round bottom flask with attached reflux condenser cyanuric chloride (3.68 g, 18.4 mmol, 1.0 eq.) was dissolved in dry THF (30 mL) under an argon atmosphere. The solution was cooled to 0 °C and 4-flourophenylmagnesium bromide (52 mL, 1 Mol, 52 mmol, 2.8 eq.) was added dropwise over 2 h. After the addition was completed the mixture was warmed to room temperature and stirred for additional 17 h. Afterwards, the reaction was quenched with distilled water and extracted with DCM. After evaporating the solvent a brown solid was obtained. The crude product was purified by column chromatography (eluent: *n*-hexane:DCM 85:15) to give 3.74 g (62 %) white solid.
^{1}H-NMR (300 MHz, CD_2Cl_2): δ (ppm) = 8.64 (dd, J = 8.9, 5.6 Hz, 4 H), 7.26 (t, J = 8.7 Hz, 4 H); ^{13}C-NMR (75 MHz, CD_2Cl_2): δ (ppm) = 108.49, 116.25, 116.54, 132.16, 132.29, 165.12, 168.49, 191.22; APCI calc. ($C_{15}H_8ClF_2N_3$): 303.1 found: 303.8

10.2 Synthesis of 9,9',9"-(5-bromobenzene-1,2,3-triyl)tris(9*H*-carbazole) (345Br)

In a two necked 100 mL round bottom flask with a reflux condenser attached 1-bromo-3,4,5-trifluorobenzene (1.40 g, 6.6 mmol, 1.0 eq.) carbazole (3.33 g, 19.9 mmol, 3.0 eq.) and caesium carbonate (8.64 g, 19.9 mmol, 4.0 eq.) were dispersed in dry DMF (35 mL) and stirred for 17 h at 170 °C under an argon atmosphere. The reaction mixture was quenched with distilled water and the product was extracted with DCM. After evaporating the solvent a white solid was obtained. The crude product was purified by column chromatography (eluent: *n*-hexane:DCM 60:40) to give 2.77 g (64 %) white solid.
^{1}H-NMR (300 MHz, CD_2Cl_2): δ (ppm) = 8.13 (s, 2 H), 7.86 –7.71 (m, 4 H), 7.42 (d, J = 7.6 Hz, 2 H), 7.25 (dt, J = 8.2, 2.9 Hz,4 H), 7.17 –6.90 (m, 10 H), 6.80 (t, J = 7.4 Hz, 2 H), 6.70 (t, J = 7.5 Hz, 2 H); APCI calc. ($C_{42}H_{26}BrN_3$): 651.1 found: 651.7

10.3 Synthesis of 9,9',9"-(4-bromobenzene-1,2,3-triyl)tris(9*H*-carbazole) (234Br)

In a two necked 100 mL round bottom flask with a reflux condenser attached 1-bromo-2,3,4-trifluorobenzene (1.01 g, 4.7 mmol, 1.0 eq.) carbazole (2.38 g, 14.2 mmol, 3.0 eq.) and caesium carbonate (6.19 g, 19.0 mmol, 4.0 eq.) were dispersed in dry DMF (35 mL) and stirred for 17 h at 170 °C under an argon atmosphere. The reaction mixture was quenched with distilled water and the product was extracted with DCM. After evaporating the solvent a white solid was obtained. The crude product was purified by column chromatography (eluent: *n*-hexane:DCM 60:40) to give 2.26 g (73 %) white solid.
^{1}H-NMR (300 MHz, CD_2Cl_2): δ (ppm) = 8.29 (d, J = 8.8 Hz, 1 H), 7.92 (d, J = 8.7 Hz, 1 H), 7.84 –7.72 (m, 4 H), 7.40 –7.25 (m, 4 H), 7.13 –6.99 (m,12 H), 6.77 (t, J = 6.9 Hz, 2 H), 6.68 (t, J = 7.0 Hz, 2 H); APCI calc. ($C_{42}H_{26}BrN_3$): 651.1 found: 651.7

10.4 Synthesis of 9,9',9"-(2-bromobenzene-1,3,4-triyl)tris(9*H*-carbazole) (236Br)

The synthetic procedure was similar to the synthesis of 9,9',9"-(4-bromobenzene-1,2,3-triyl)-tris(9*H*-carbazole) **(234Br)** the only difference was the usage of 1-bromo-2,3,5-trifluoro-benzene (1.01 g, 4.7 mmol, 1.0 eq.) as starting material. The crude product was purified by column chromatography (eluent: *n*-hexane:DCM 60:40) to give 1.48 g (48 %) white solid.
^{1}H-NMR (250 MHz, CD_2Cl_2): δ (ppm) = 8.22 (d, J = 7.3 Hz, 2 H), 8.00 (s, 2 H), 7.81 (t, J = 6.7 Hz 4 H), 7.57 (t, J = 7.7 Hz 2 H), 7.46 –7.24 (m, 6 H), 7.24 –7.02 (m, 1 H0); APCI calc. ($C_{42}H_{26}BrN_3$): 651.1 found: 651.8

10.5 Synthesis of 9,9',9"-(5-bromobenzene-1,2,4-triyl)tris(9*H*-carbazole) (245Br)

The synthetic procedure was similar to the synthesis of 9,9',9"-(4-bromobenzene-1,2,3-triyl)-tris(9*H*-carbazole) **(234Br)** the only difference was the usage of 1-bromo-2,3,6-trifluorobenzene (1.01 g, 4.7 mmol, 1.0 eq.) as starting material. The crude product was purified by column chromatography (eluent: *n*-hexane:DCM 60:40) to give 1.74 g (56 %) white solid.
^{1}H-NMR (300 MHz, CD_2Cl_2): δ (ppm) = 8.31 (s, 1 H), 8.11 (d, J = 7.7 Hz, 2 H), 7.95 (s, 1 H), 7.69 –7.85 (m, 4 H), 7.44 (t, J = 7.2, 7.2 Hz, 2 H), 7.31 (dd, J = 10.2, 7.9 Hz, 5 H), 7.19 (dd, J = 6.2, 2.7 Hz, 2 H), 6.94-7.14 (m, 9 H); APCI calc. ($C_{42}H_{26}BrN_3$): 651.1 found: 651.8

10.6 Synthesis of 9,9',9"-[5-(4,6-bis(4-fluorophenyl)-1,3,5-triazin-2-yl)benzene-1,2,3-triyl]tris(9*H*-carbazole) (345Trz)

In a first step a Miyaura-borylation of **345Br** was performed followed by a Suzuki reaction to couple the donor unit to the triazine acceptor **Trz**.
In a two necked 100 mL round bottom flask with a reflux condenser attached 9,9',9"-(5-bromo-benzene-1,2,3-triyl)tris(9*H*-carbazole) **(345Br)** (2.77 g, 4.2 mmol, 1.0 eq.), bis(pinacol)diborane (1.40 g, 5.5 mmol, 1.3 eq.), potassium acetate (1.33 g, 13.5 mmol, 3.2 eq.) and Pd[dppf]Cl_2 (0.11 g, 0.1 mmol, 0.03 eq.) were flushed 3 times with argon. Then the solids were dissolved in anhydrous 1,4-dioxane (40 mL) and stirred at 125 °C over night (17 h). After the reaction cooled to room temperature the mixture was extracted with DCM.The organic layer was dried over $MgSO_4$ and the solvent was evaporated afterwards. The crude product was purified by column chromatography (eluent: *n*-hexane:DCM 60:40) to give 3.27 g (54 %) yellow solid.
In a 50 mL Schlenk-tube the pinacol borane derivate of **345Br** (0.31 g, 0.4 mmol, 1.0 eq.), 2-chloro-4,6-bis(4-fluorophenyl)-1,3,5-triazine **Trz** (0.15 g, 0.5 mmol, 1.1 eq.), Pd[PPh_3]$_4$ (0.03 g, 0.02 mmol, 0.05 eq.), K_2CO_4 (0.18 g, 1.3 mmol, 3.0 eq.) were mixed in THF (10 mL) and distilled water (5 mL) and were flushed with argon for 15 min. Afterwards, the mixture was heated to 80 °C and stirred over night (17 h). When the reaction reached room temperature it was quenched with distilled water and extracted with DCM. The organic layer was dried over $MgSO_4$ and the solvent evaporated to give a yellow solid. The crude product was purified by

column chromatography (eluent: *n*-hexane:DCM 60:40) to give 0.20 g (54 %) yellow solid.
^{1}H-NMR (300 MHz, CD_2Cl_2): δ (ppm) = 9.31 (s, 2 H), 8.76 (dd, $J = 8.7, 5.7$ Hz, 4 H), 7.95 –7.75 (m, 4 H), 7.44 (d, $J = 7.7$ Hz, 2 H), 7.39 –7.28 (m, 4 H), 7.22 (t, $J = 8.7$ Hz, 4 H), 7.08 (td, $J = 6.6, 3.7$ Hz 10 H), 6.82 (t, $J = 7.4$ Hz, 2 H), 6.70 (t, $J = 8.0$ Hz, 2 H); ^{13}C-NMR (75 MHz, CD_2Cl_2): δ (ppm) = 25.68, 108.49, 110.25, 110.67, 116.05, 116.34, 119.65, 120.24, 120.37, 120.60, 123.73, 123.80, 125.05, 125.91, 130.58, 131.83, 131.96, 138.03, 138.49, 138.66, 140.27, 164.73, 168.12, 171.58; APCI calc. ($C_{57}H_{34}F_2N_6$): 840.3 found: 841.0

10.7 Synthesis of 9,9',9"-[4-(4,6-bis(4-fluorophenyl)-1,3,5-triazin-2-yl)benzene-1,2,3-triyl]tris(9*H*-carbazole) (234Trz)

In a first step the boronic acid derivate of **234Br** was synthesized and afterwards coupled via a Suzuki reaction to the triazine acceptor **Trz**.
In a 50 mL Schlenk-tube **234Br** (1.00 g, 1.5 mmol, 1.0 eq.) was dissolved in anhydrous THF (30 mL) and cooled to -78 °C in an actone/dry ice bath. *n*-BuLi (1.87 mL, 1.6 M, 3.0 mmol, 2.0 eq.) was added slowly to the cool solution and the resulting solution was stirred for an additional 1 h at -78 °C. Then trimethyl borate (0.28 mL, 2.3 mmol, 1.5 eq.) was added to the mixture and the cooling bath was removed and the reaction stirred at room temperature over night (17 h). Then the reaction was quenched with 10% HCl, extracted with ethyl acetate and distilled water. The solvent of the organic layers was evaporated. The crude product was purified by column chromatography (starting with *n*-hexane:DCM 50:50 then gradually adding methanol) to give 0.62 g white solid (66%).
In a 50 mL Schlenk-tube the boronic acid derivate of **234Br** (0.42 g, 0.7 mmol, 1.0 eq.), 2-chloro-4,6-bis(4-fluorophenyl)-1,3,5-triazine **Trz** (0.23 g, 0.8 mmol, 1.1 eq.), $Pd[PPh_3]_4$ (0.04 g,0.03 mmol, 0.05 eq.), K_2CO_4 (0.28 g, 2.1 mmol, 3.0 eq.) were mixed in THF (10 mL) and distilled water (5 mL) and were flushed with argon for 15 min. Afterwards, the mixture was heated to 80 °C and stirred over night (17 h). When the reaction reached room temperature it was quenched with distilled water and extracted with DCM. The organic layer was dried over $MgSO_4$ and the solvent evaporated to give a yellow solid. The crude product was purified by column chromatography (eluent: *n*-hexane:DCM 60:40) to give 0.33 g (58 %) yellow solid.
^{1}H-NMR (300 MHz, CD_2Cl_2): δ (ppm) =. 8.75(d, $J = 8.4$ Hz, 1 H), 8.22 (d, $J = 8.4$ Hz, 1 H), 7.96 (dd, $J = 8.8, 5.6$ Hz 4 H), 7.88 –7.76 (m, 2 H), 7.68 –7.54 (m, 2 H), 7.45 (d, $J = 7.50$ Hz 2 H), 7.37–7.25 (m, 2 H), 7.22 –7.04 (m, 8 H), 6.98 (qd, $J = 8.2, 3.6$ Hz, 8 H), 6.77 (dt, $J = 27.4, 7.2$ Hz, 4 H); ^{13}C-NMR (75 MHz, CD_2Cl_2): δ (ppm) = 25.68, 110.17, 110.40, 110.76, 115.69, 115.98, 119.66, 120.13, 120.20, 120.66, 122.29, 122.40, 123.56, 123.89, 123.98, 124.95, 125.65, 125.81, 131.06, 131.44, 131.56, 133.31, 139.25, 140.23, 140.96, 170.80; APCI calc. ($C_{57}H_{34}F_2N_6$): 840.3 found: 840.8

10.8 Synthesis of 9,9',9"-[2-(4,6-bis(4-fluorophenyl)-1,3,5-triazin-2-yl)benzene--1,3,4-triyl]tris(9*H*-carbazole) (236Trz)

The synthetic procedure was similar to the synthesis of 9,9',9"-[4-(4,6-bis(4-fluorophenyl)-1,3,5-triazin-2-yl)benzene-1,2,3-triyl]tris(9*H*-carbazole) **(234Trz)** the only difference was the usage of 9,9',9"-(2-bromobenzene-1,3,4-triyl)tris(9*H*-carbazole) **236Br** (1.48 g, 2.3 mmol, 1.0 eq.) as starting material. The crude boronic acid derivate was purified by column chromatography (starting with *n*-hexane:DCM 50:50 then gradually adding methanol) to give 0.57 g yellowish solid (41%).

The Suzuki reaction was carried out as described for 9,9',9"-[4-(4,6-bis(4-fluorophenyl)-1,3,5-triazin-2-yl)benzene-1,2,3-triyl]tris(9*H*-carbazole) **(234Trz)** (Chapter 10.7) with boronic acid derivate of **236Br** (0.53 g, 0.9 mmol, 1.0 eq.) as starting material. The crude product was purified by column chromatography (eluent: *n*-hexane:DCM 60:40) to give 0.31 g (43 %) yellow solid.

^{1}H-NMR (250 MHz, CD_2Cl_2): δ (ppm) = 9.05 (d, J = 20.8 Hz, 1 H), 8.26 (d, J = 17.8 Hz, 1 H), 8.12 –7.55 (m, 8 H), 7.53 –7.23 (m, 8 H), 7.21 –6.89 (m, 1 H2), 6.81 (t, J = 7.4 Hz, 2 H), 6.75 –6.59 (m, 2 H); ^{13}C-NMR (75 MHz, CD_2Cl_2): δ (ppm) = 25.68, 109.94, 110.18, 110.27, 110.52, 110.89, 110.93, 115.69, 115.98, 119.66, 120.27, 120.31, 120.36, 120.44, 120.49, 120.73, 120.85, 120.90, 120.97, 122.29, 124.86, 124.91, 125.75, 125.92, 126.20, 126.65, 131.52, 131.64, 132.53, 135.06, 167.87, 170.96; APCI calc. ($C_{57}H_{34}F_2N_6$): 840.3 found: 841.0

10.9 Synthesis of 9,9',9"-[5-(4,6-bis(4-fluorophenyl)-1,3,5-triazin-2-yl)benzene-1,2,4-triyl]tris(9*H*-carbazole) (245Trz)

The synthetic procedure was similar to the synthesis of 9,9',9"-[4-(4,6-bis(4-fluorophenyl)-1,3,5-triazin-2-yl)benzene-1,2,3-triyl]tris(9*H*-carbazole) **(234Trz)** the only difference was the usage of 9,9',9"-(5-bromobenzene-1,2,4-triyl)tris(9*H*-carbazole) **(245Br)** (1.00 g, 1.5 mmol, 1.0 eq.) as starting material. The crude boronic acid derivate was purified by column chromatography (starting with *n*-hexane:DCM 50:50 then gradually adding methanol) to give 0.47 g light brown solid (50%).

The Suzuki reaction was carried out as described for 9,9',9"-[4-(4,6-bis(4-fluorophenyl)-triazin-2-yl)benzene-1,2,3-triyl]tris(9*H*-carbazole) **(234Trz)** (Chapter 10.7) with boronic acid derivate of **245Br** (0.47 g, 0.8 mmol, 1.0 eq.) as starting material.

The crude product was purified by column chromatography (eluent: *n*-hexane:DCM 60:40) to give 0.34 g (53 %) yellow solid.

^{1}H-NMR (250 MHz, CD_2Cl_2): δ (ppm) = 9.10 (s, 1 H), 8.30 (s, 1 H) 8.09 (d, J = 7.7 Hz, 2 H), 8.02 (dd, J = 8.9, 5.7 Hz, 4 H), 7.96 –7.81 (m, 4 H), 7.55 –7.35 (m, 8 H), 7.28 (t, J = 6.6 Hz, 2 H), 7.21 –7.7.08 (m, 8 H), 7.00 (t, J = 8.8 Hz, 4 H); ^{13}C-NMR (75 MHz, CD_2Cl_2): δ (ppm) = 109.86, 110.13, 115.53, 115.56, 120.49, 120.72, 120.85, 120.97, 124.07, 124.15, 126.17, 126.65, 131.30, 131.63, 131.71, 132.45, 134.64, 135.15, 136.26, 137.17, 138.19, 139.76, 140.04, 141.88, 164.50, 167.85, 170.92; APCI calc. ($C_{57}H_{34}F_2N_6$): 840.3 found: 841.0

10.10 Synthesis of 6,6'-(perfluoro-1,4-phenylene)bis(2,4-diphenyl-1,3,5-triazine) (4F2Trz)

In an open 100 mL round-bottom flask 2,3,5,6-tetrafluoroterephthalaldehyde (0.50 g, 2.43 mmol, 1.0 eq.), benzamidine hydrochloride (2.28 g, 14.6 mmol, 6.0 eq.), copper(II) acetate (0.18 g, 0.97 mmol, 0.4 eq.) and sodium carbonate (1.54 g, 14.6 mmol, 6.0 eq.) were dissolved in toluene (40 mL). The resulting blue suspension was heated to 130 °C and stirred for 6 days. While the reaction further copper(II) acetate was added when reaction mixture turned yellow. After complete conversion (checked by APCI) the reaction mixture was poured into 10% HCl and washed three times with DCM. The crude product was collected by filtration as a white precipitate. Due to insolubility the product was purified by vacuum sublimation to give 0.32 g (22%) white solid.
^{1}H-NMR (700 MHz, $C_2D_2Cl_4$): δ (ppm) = 8.69 (d, J = 7.7 Hz, 8 H), 7.61 (t, J = 7.3 Hz, 4 H), 7.55 (t, J = 7.5 Hz, 8 H); APCI calc. ($C_{36}H_{20}F_4N_6$): 612.2 found: 612.8

10.11 Synthesis of 9,9',9",9"'-(3,6-bis(4,6-diphenyl-1,3,5-triazin-2-yl)benzene-1,2,4,5-tetrayl)tetrakis(9*H*-carbazole) (4Cz2Trz)

In a 100 mL Schlenk-tube **4F2Trz** (0.30 g, 0.49 mmol, 1.0 eq.), 9*H*-carbazole (0.33 g, 1.96 mmol, 4.0 eq.) and Cs_2CO_3 (3.19 g, 9.79 mmol, 20 eq.) were flushed with argon 3 times prior to adding dry DMF (20 mL). The resulting yellow suspension was heated to 175 °C and stirred for 17 h. After cooling to room temperature the reaction mixture was poured in demin. water (150 mL). The crude product was collected by filtration as a yellow solid. Due to insolubility the product was purified by vacuum sublimation to give 0.23 g (39%) yellow solid.
^{1}H-NMR (700 MHz, $C_2D_2Cl_4$): δ (ppm) = 7.43 (dd, J = 20.0, 7.8 Hz, 16 H), 7.26 (t, J = 7.9 Hz, 4 H), 7.21 (d, J = 7.6 Hz, 8 H), 7.02 (q, J = 8.3 Hz, 16 H), 6.87 (t, J = 7.5 Hz, 8 H); MALDI-TOF calc. ($C_{84}H_{52}N_{10}$): 1200.44 found: 1200.38

10.12 Synthesis of 9-(4-bromo-3,5-dimethylphenyl)-3,6-di-*tert*-butyl-9*H*-carbazole (tBuCz)

In a 100 mL Schlenk-flask 2-bromo-5-iodo-1,3-dimethylbenzene (3.00 g, 9.65 mmol, 1.0 eq.), 3,6-di-*tert*-butyl-9*H*-carbazole (2.97 g, 10.6 mmol, 1.1 eq.), copper (1.84 g, 28.9 mmol, 3.0 eq.) and K_2CO_3 (4.00 g, 28.9 mmol, 3.0 eq.) were purged 3 times with argon and dissolved in dry DMF (30 mL). The reaction mixture was heated to 130 °C and stirred for 24 h. After cooling to room temperature, the reaction mixture was washed with demin. water and extracted with DCM. The organic layer was dried over $MgSO_4$ and afterwards the solvent was evaporated. The crude product was purified by column chromatography (eluent: *n*-hexane:DCM 10:1) to give 3.82 g (86 %) white solid.
^{1}H-NMR (700 MHz, CD_2Cl_2): δ (ppm) = 8.15(d, J = 1.6 Hz, 2 H), 7.48 (dd, J = 8.6, 2.0 Hz, 2 H), 7.34 (d, J = 8.6 Hz, 2 H), 2.52 (s, 6 H), 1.46 (s, 1 H8); ^{13}C-NMR (176 MHz, CD_2Cl_2): δ (ppm) = 24.20, 32.15, 109.59, 116.68, 123.68, 124.09, 125.84, 126.56, 137.03, 139.51, 140.43, 143.41;
APCI calc. ($C_{28}H_{32}BrN$): 461.2 found: 462.0

10.13 Synthesis of 5,10-bis(4-(3,6-di-*tert*-butyl-9*H*-carbazol-9-yl)-2,6-dimethylphenyl)-5,10-dihydroboranthrene (tBuCzDBA)

The reaction, which includes 3 steps, was carried out without purification between the steps due to the high oxygen and water sensitivity of the used compounds. The first step was the reaction of 1,2-bis(trimethylsilyl)benzene and tribromoborate to give 5,10-dibromo-5,10-diboranthrene. In a second step **tBuCz** was transferred into a corresponding lithium species and the third step was the reaction of the lithium species with 5,10-dibromo-5,10-diboranthrene to give **tBuCzDBA**.
In a 50 mL Schlenk-tube 1,2-bis(trimethylsilyl)benzene (1.60 g, 7.20 mmol, 1.0 eq.), tribromoborate (5.52 g, 22.0 mmol, 3.1 eq.) and dry toluene (10 mL) were degassed with 3 freeze-pump-thaw cycles. After completing the degassing the septum was replaced by a glass plug to ensure that the tube is closed tightly. The Schlenk-tube was set under vacuum and the stopcock was closed. The reaction mixture was heated to 120 °C and stirred for 5 d under vacuum. The resulting brown solution was cooled to room temperature and immediately transferred to the subsequent reaction.
In a 250 mL Schlenk-flask **tBuCz** (3.36 g, 7.27 mmol, 1.0 eq.) was purged 3 times with argon prior to dissolving in dry THF (100 mL). The solution was cooled to -78 °C and *n*-BuLi (7.02 mL, 1.6 M, 11.2 mmol, 1.6 eq.) was added dropwise under vigorous stirring. When addition was completed the mixture was stirred for additional 15 min at -78 °C before warming to 0 °C and stirring for 30 min.
For the third step the reaction mixture of step 1 was transferred immediately to the flask of step 2 via syringe and added dropwise while stirring at -78 °C. To ensure all product of step 1 is transferred to the third step, the Schlenk-tube was filled with dry toluene for two times to dissolve remaining colorless crystals. After addition the reaction solution turned yellow and was warmed to room temperature and stirred for additional 8 h. The solution was washed with

saturated NH_4Cl(aq.) solution and extracted with DCM. The solvent for the combined organic layers was evaporated and gave a yellow solid. The crude product was purified by column chromatography (eluent: *n*-hexane:DCM 10:2) to give 0.21 g (6 % to first step) orange solid.
^{1}H-NMR (300 MHz, CD_2Cl_2): δ (ppm) = 8.21 (d, J = 1.1 Hz, 4 H), 7.81 (dd, J = 5.3, 3.3 Hz, 4 H), 7.68–7.51 (m, 12 H), 7.34 (s, 4 H), 2.24 (s, 12 H), 1.50 (s, 36 H); ^{13}C-NMR (75 MHz, CD_2Cl_2): δ (ppm) = 22.91, 32.44, 35.07, 109.93, 116.64, 118.60, 123.64, 123.95, 124.45, 134.35, 137.79, 139.46, 139.85, 140.08, 143.11; MALDI-TOF calc. ($C_{68}H_{72}B_2N_2$): 938.59 found: 938.60

11 Literature

[1] G. Hong, X. Gan, C. Leonhardt, Z. Zhang, J. Seibert, J. M. Busch, S. Bräse, *Advanced Materials* **2021**, *33*, 2005630.

[2] Y.-L. Chang, Z.-H. Lu, *Wiley Encyclopedia of Electrical and Electronics Engineering* **1999**, 1–15.

[3] M. Y. Wong, E. Zysman-Colman, *Advanced Materials* **2017**, *29*, 1605444.

[4] C. Poriel, J. Rault-Berthelot, *Advanced Functional Materials* **2020**, *30*, 1910040.

[5] D. R. Lee, M. Kim, S. K. Jeon, S.-H. Hwang, C. W. Lee, J. Y. Lee, *Advanced Materials* **2015**, *27*, 5861–5867.

[6] C. W. Tang, S. A. VanSlyke, *Applied physics letters* **1987**, *51*, 913–915.

[7] A. B. Hargadon, Y. Douglas, *Administrative science quarterly* **2001**, *46*, 476–501.

[8] M. G. Craford in Fifth International Conference on Solid State Lighting, *Vol. 5941*, International Society for Optics and Photonics, **2005**, p. 594101.

[9] S. Schmidbauer, A. Hohenleutner, B. König, *Advanced Materials* **2013**, *25*, 2114–2129.

[10] H. Uoyama, K. Goushi, K. Shizu, H. Nomura, C. Adachi, *Nature* **2012**, *492*, 234–238.

[11] D. Volz, M. Wallesch, C. Fléchon, M. Danz, A. Verma, J. Navarro, D. Zink, S. Bräse, T. Baumann, *Green Chemistry* **2015**, *17*, 1988–2011.

[12] J.-H. Lee, C.-H. Chen, P.-H. Lee, H.-Y. Lin, M.-k. Leung, T.-L. Chiu, C.-F. Lin, *Journal of Materials Chemistry C* **2019**, *7*, 5874–5888.

[13] W. Quirino, K. Teixeira, C. Legnani, V. Calil, B. Messer, O. V. Neto, M. Pacheco, M. Cremona, *Thin Solid Films* **2009**, *518*, 1382–1385.

[14] C. Poriel, J. Rault-Berthelot, *Advanced Functional Materials* **2020**, *30*, 1910040.

[15] N. B. Kotadiya, H. Lu, A. Mondal, Y. Ie, D. Andrienko, P. W. Blom, G.-J. A. Wetzelaer, *Nature materials* **2018**, *17*, 329–334.

[16] W. Liu, N. B. Kotadiya, P. W. Blom, G.-J. A. Wetzelaer, D. Andrienko, *Advanced Materials Technologies* **2021**, *6*, 2000120.

[17] J. A. Röhr, T. Kirchartz, J. Nelson, *Journal of Physics: Condensed Matter* **2017**, *29*, 205901.

[18] N. Mott, RW Gurney Electronic Processes in Ionic Crystals, **1940**.

[19] N. B. Kotadiya, A. Mondal, P. W. Blom, D. Andrienko, G.-J. A. Wetzelaer, *Nature materials* **2019**, *18*, 1182–1186.

[20] G. Wetzelaer, *Physical Review Applied* **2020**, *13*, 034069.

[21] P. De Bruyn, A. Van Rest, G. Wetzelaer, D. M. de Leeuw, P. W. Blom, *Physical review letters* **2013**, *111*, 186801.

[22] K. Seki, H. Oji, E. Ito, N. Hayashi, Y. Ouchi, H. Ishii in Organic Light-Emitting Materials and Devices III, *Vol. 3797*, SPIE, **1999**, pp. 178–188.

[23] A. Köhler, H. Bässler, *Electronic processes in organic semiconductors: An introduction*, John Wiley & Sons, **2015**.

[24] B. T. Lim, S. Okajima, A. Chandra, E. Lim, *Chemical Physics Letters* **1981**, *79*, 22–27.

[25] H. Uoyama, K. Goushi, K. Shizu, H. Nomura, C. Adachi, *Nature* **2012**, *492*, 234–238.

[26] F. B. Dias, T. J. Penfold, A. P. Monkman, *Methods and applications in fluorescence* **2017**, *5*, 012001.

[27] Y. Li, N. B. Kotadiya, B. van Der Zee, P. W. Blom, G.-J. A. Wetzelaer, *Advanced Optical Materials* **2021**, *9*, 2001812.

[28] N. B. Kotadiya, P. W. Blom, G.-J. A. Wetzelaer, *Nature Photonics* **2019**, *13*, 765–769.

[29] G. Wetzelaer, M. Kuik, H. Nicolai, P. Blom, *Physical Review B* **2011**, *83*, 165204.

[30] A. J. Oostra, P. W. Blom, J. J. Michels, *Organic Electronics* **2014**, *15*, 1166–1172.

[31] W. Shockley, *Bell System Technical Journal* **1949**, *28*, 435–489.

[32] G. Wetzelaer, L. Koster, P. Blom, *Physical review letters* **2011**, *107*, 066605.

[33] K. Harada, A. Werner, M. Pfeiffer, C. Bloom, C. Elliott, K. Leo, *Physical review letters* **2005**, *94*, 036601.

[34] A. L. Burin, M. A. Ratner, *The Journal of Physical Chemistry A* **2000**, *104*, 4704–4710.

[35] J. Tauc, R. Grigorovici, A. Vancu, *physica status solidi (b)* **1966**, *15*, 627–637.

[36] J. H. Kim, T. Schembri, D. Bialas, M. Stolte, F. Würthner, *Advanced Materials* **2021**, 2104678.

[37] S. Ma, S. Du, G. Pan, S. Dai, B. Xu, W. Tian, *Aggregate* **2021**, *2*, e96.

[38] W. Pasveer, J. Cottaar, C. Tanase, R. Coehoorn, P. Bobbert, P. Blom, D. De Leeuw, M. Michels, *Physical review letters* **2005**, *94*, 206601.

[39] T.-L. Wu, M.-J. Huang, C.-C. Lin, P.-Y. Huang, T.-Y. Chou, R.-W. Chen-Cheng, H.-W. Lin, R.-S. Liu, C.-H. Cheng, *Nature Photonics* **2018**, *12*, 235–240.

[40] B. van der Zee, Y. Li, G.-J. A. Wetzelaer, P. W. Blom, *Advanced Electronic Materials* **2022**, 2101261.

[41] S. R. Forrest, D. D. Bradley, M. E. Thompson, *Advanced Materials* **2003**, *15*, 1043–1048.

[42] M. Huang in Organic, Hybrid, and Perovskite Photovoltaics XVIII, *Vol. 10363*, SPIE, **2017**, pp. 68–74.

12 Appendix

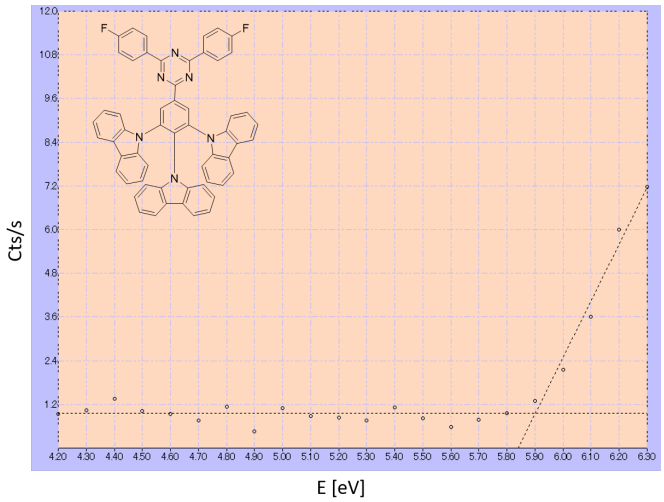

Figure A.1: Ultraviolet photoelectron spectroscopy of **345Trz**.

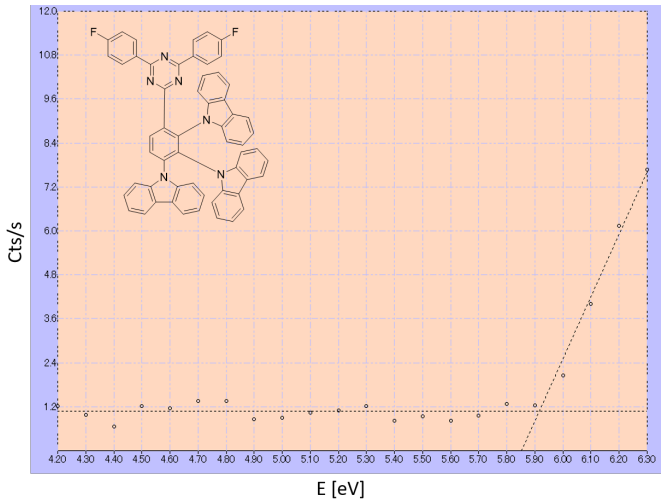

Figure A.2: Ultraviolet photoelectron spectroscopy of **245Trz**.

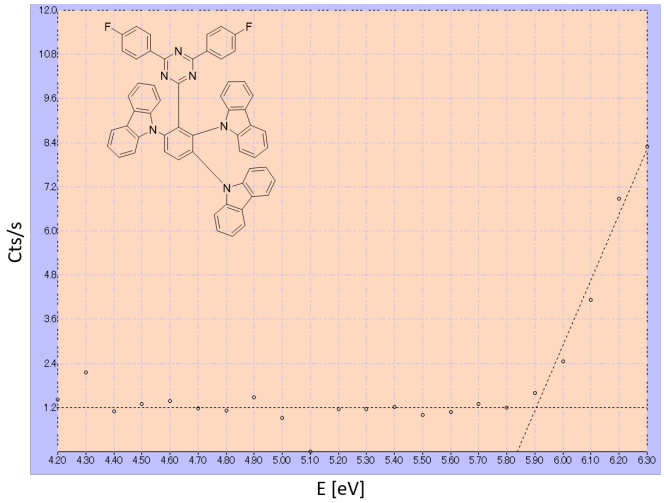

Figure A.3: Ultraviolet photoelectron spectroscopy of **236Trz**.

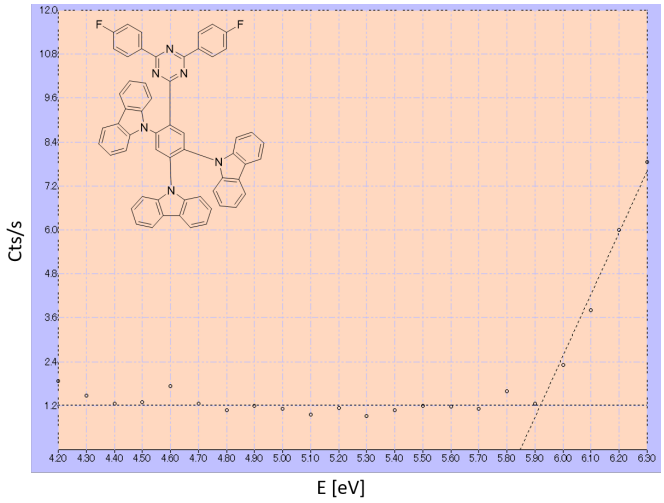

Figure A.4: Ultraviolet photoelectron spectroscopy of **245Trz**.

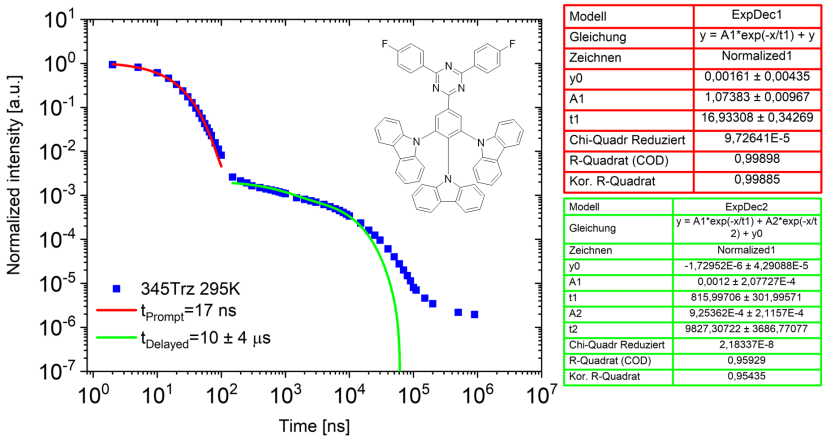

Modell	ExpDec1
Gleichung	y = A1*exp(-x/t1) + y
Zeichnen	Normalized1
y0	0,00161 ± 0,00435
A1	1,07383 ± 0,00967
t1	16,93308 ± 0,34269
Chi-Quadr Reduziert	9,72641E-5
R-Quadrat (COD)	0,99898
Kor. R-Quadrat	0,99885

Modell	ExpDec2
Gleichung	y = A1*exp(-x/t1) + A2*exp(-x/t2) + y0
Zeichnen	Normalized1
y0	-1,72952E-6 ± 4,29088E-5
A1	0,0012 ± 2,07727E-4
t1	815,99706 ± 301,99571
A2	9,25362E-4 ± 2,1157E-4
t2	9827,30722 ± 3686,77077
Chi-Quadr Reduziert	2,18337E-8
R-Quadrat (COD)	0,95929
Kor. R-Quadrat	0,95435

(a) Fitted TRPL spectrum of **345Trz**.

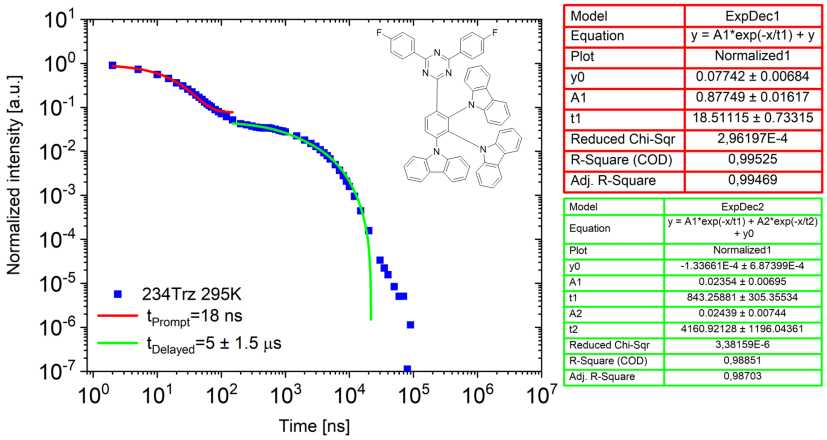

Model	ExpDec1
Equation	y = A1*exp(-x/t1) + y
Plot	Normalized1
y0	0.07742 ± 0.00684
A1	0.87749 ± 0.01617
t1	18.51115 ± 0.73315
Reduced Chi-Sqr	2,96197E-4
R-Square (COD)	0,99525
Adj. R-Square	0,99469

Model	ExpDec2
Equation	y = A1*exp(-x/t1) + A2*exp(-x/t2) + y0
Plot	Normalized1
y0	-1.33661E-4 ± 6.87399E-4
A1	0.02354 ± 0.00695
t1	843.25881 ± 305.35534
A2	0.02439 ± 0.00744
t2	4160.92128 ± 1196.04361
Reduced Chi-Sqr	3,38159E-6
R-Square (COD)	0,98851
Adj. R-Square	0,98703

(b) Fitted TRPL spectrum of **234Trz**.

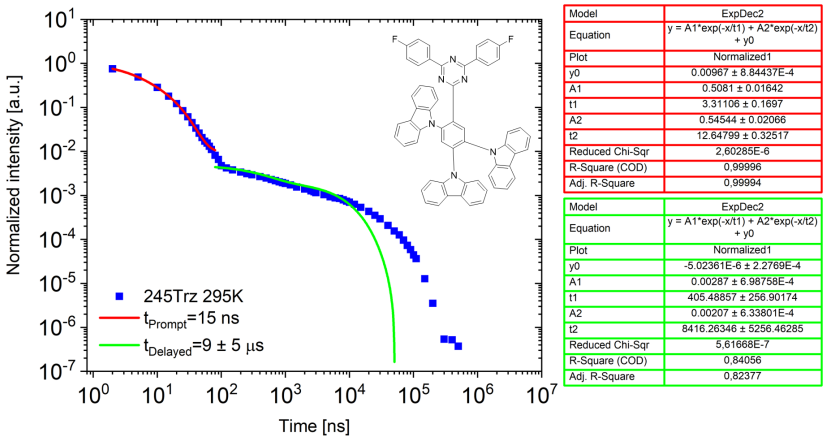

Model	ExpDec2
Equation	y = A1*exp(-x/t1) + A2*exp(-x/t2) + y0
Plot	Normalized1
y0	0.00967 ± 8.84437E-4
A1	0.5081 ± 0.01642
t1	3.31106 ± 0.1697
A2	0.54544 ± 0.02066
t2	12.64799 ± 0.32517
Reduced Chi-Sqr	2,60285E-6
R-Square (COD)	0,99996
Adj. R-Square	0,99994

Model	ExpDec2
Equation	y = A1*exp(-x/t1) + A2*exp(-x/t2) + y0
Plot	Normalized1
y0	-5.02361E-6 ± 2.2769E-4
A1	0.00287 ± 6.98758E-4
t1	405.48857 ± 256.90174
A2	0.00207 ± 6.33801E-4
t2	8416.26346 ± 5256.46285
Reduced Chi-Sqr	5,61668E-7
R-Square (COD)	0,84056
Adj. R-Square	0,82377

(c) Fitted TRPL spectrum of **245Trz**.

Figure A.5: TRPL spectra of **345Trz**, **234Trz** and **245Trz**, with exponential decay fits for prompt (red line) and delayed (green line) lifetimes.

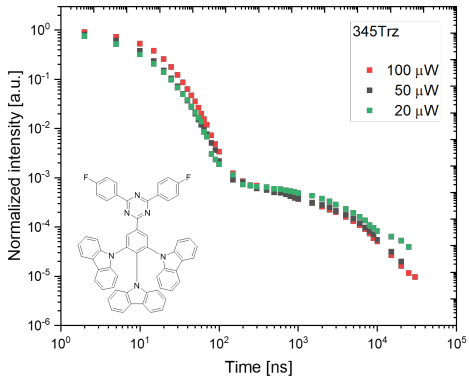

(a) Power-dependent TRPL measurement of **345Trz**.

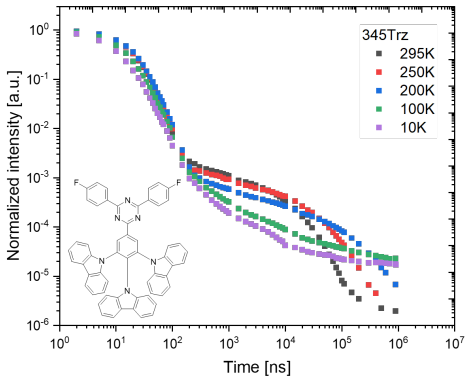

(b) Temperature-dependent TRPL measurement of **345Trz**.

Figure A.6: Temperature- and power-dependent TRPL measurements of **345Trz**.

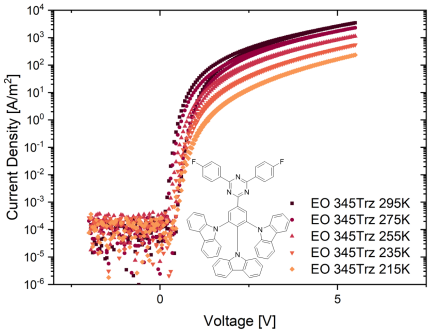

(a) Thermal scan of an EO device with **345Trz**.

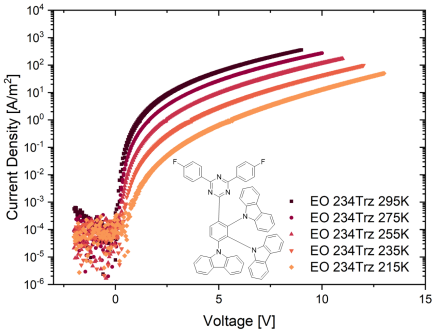

(b) Thermal scan of an EO device with **234Trz**.

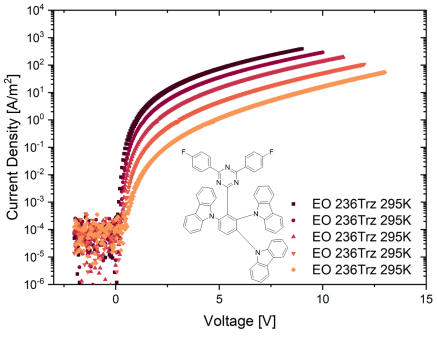

(c) Thermal scan of an EO device with **236Trz**.

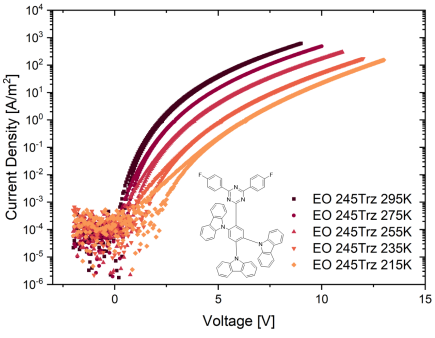

(d) Thermal scan of an EO device with **245Trz**.

Figure A.7: Thermal scans of asymmetric EO devices of **345Trz**, **234Trz**, **236Trz** and **245Trz**.

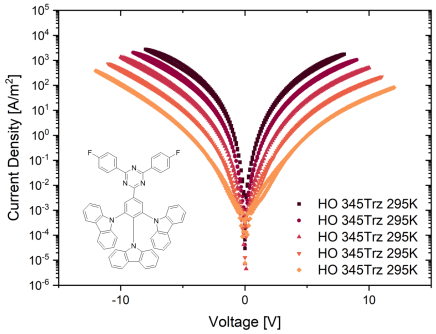

(a) Thermal scan of a HO device with **345Trz**.

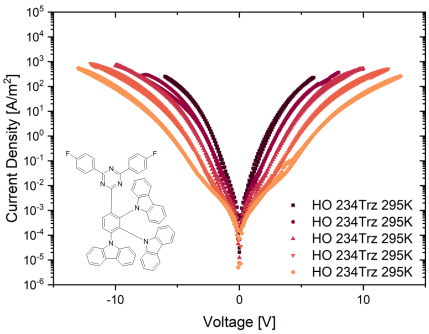

(b) Thermal scan of a HO device with **234Trz**.

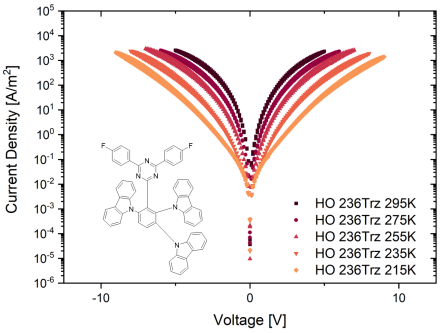

(c) Thermal scan of a HO device with **236Trz**.

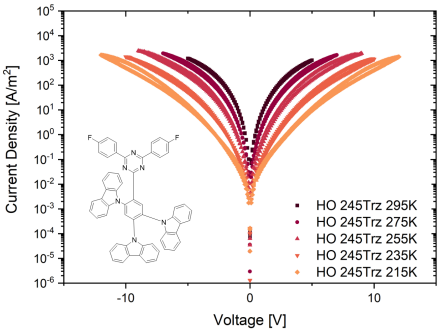

(d) Thermal scan of a HO device with **245Trz**.

Figure A.8: Thermal scans of symmetric HO devices of **345Trz**, **234Trz**, **236Trz** and **245Trz**.

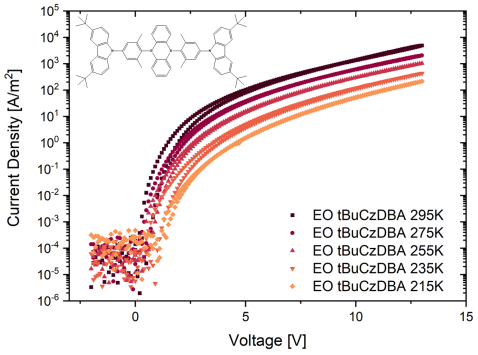

(a) Thermal scan of an asymmetric EO device with **tBuCzDBA**.

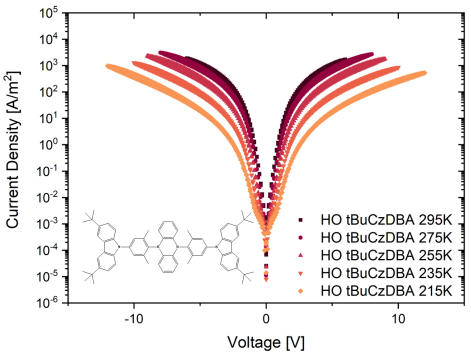

(b) Thermal scan of a symmetric HO device with **tBuCzDBA**.

Figure A.9: Thermal scan of single-carrier devices with **tBuCzDBA**.

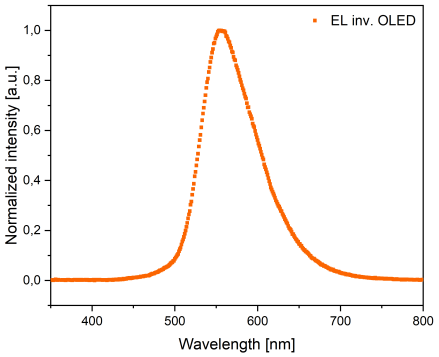

(a) Electroluminescent spectrum of inverted OLED with **tBuCzDBA**.

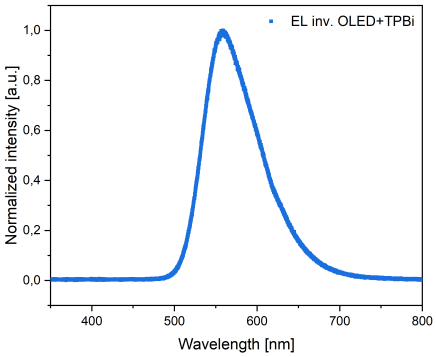

(b) Electroluminescent spectrum of inverted OLED with TPBi interlayer with **tBuCzDBA**.

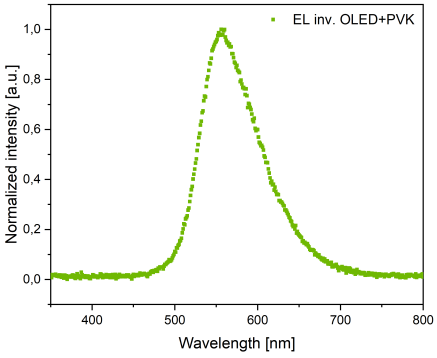

(c) Electroluminescent spectrum of inverted OLED with PVK interlayer with **tBuCzDBA**.

Figure A.10: Electroluminescent spectra of different **tBuCzDBA** OLEDs.

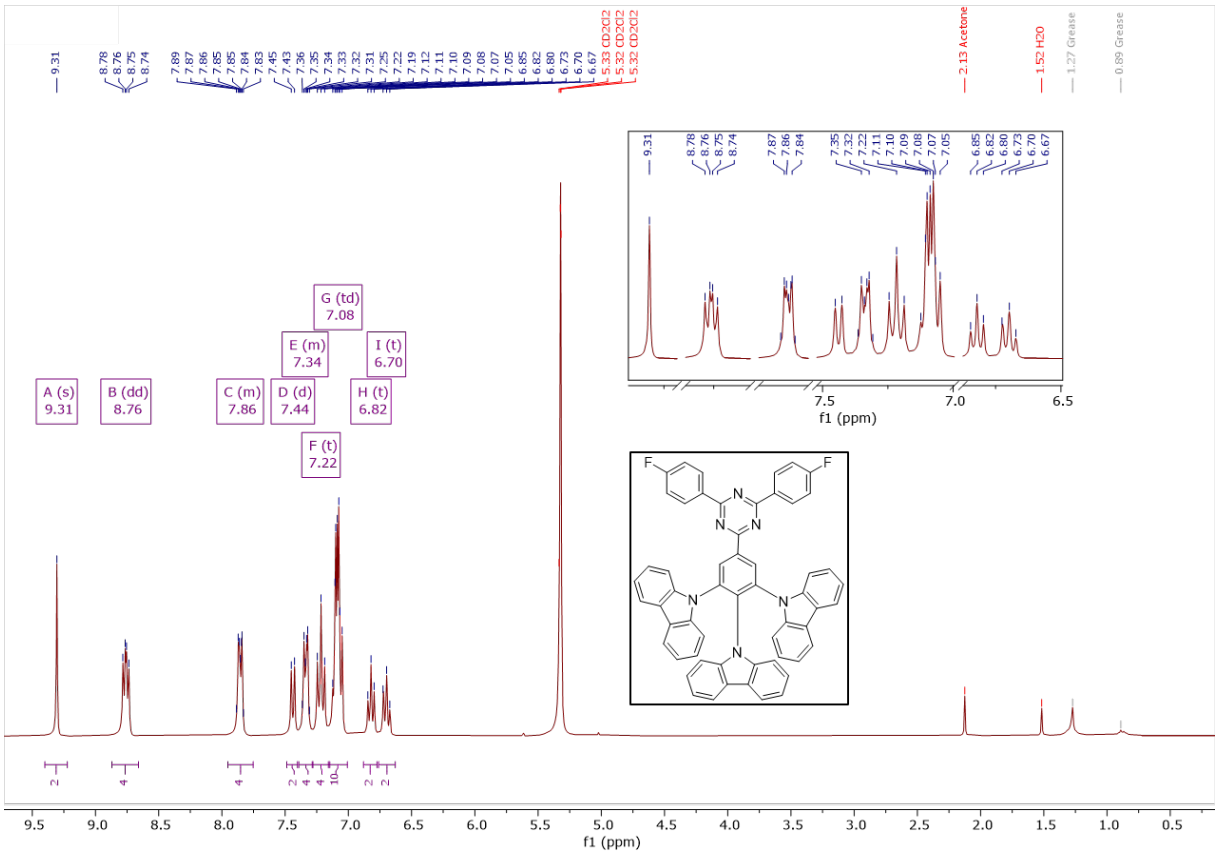

Figure A.11: ^{1}H-NMR spectrum of **345Trz**.

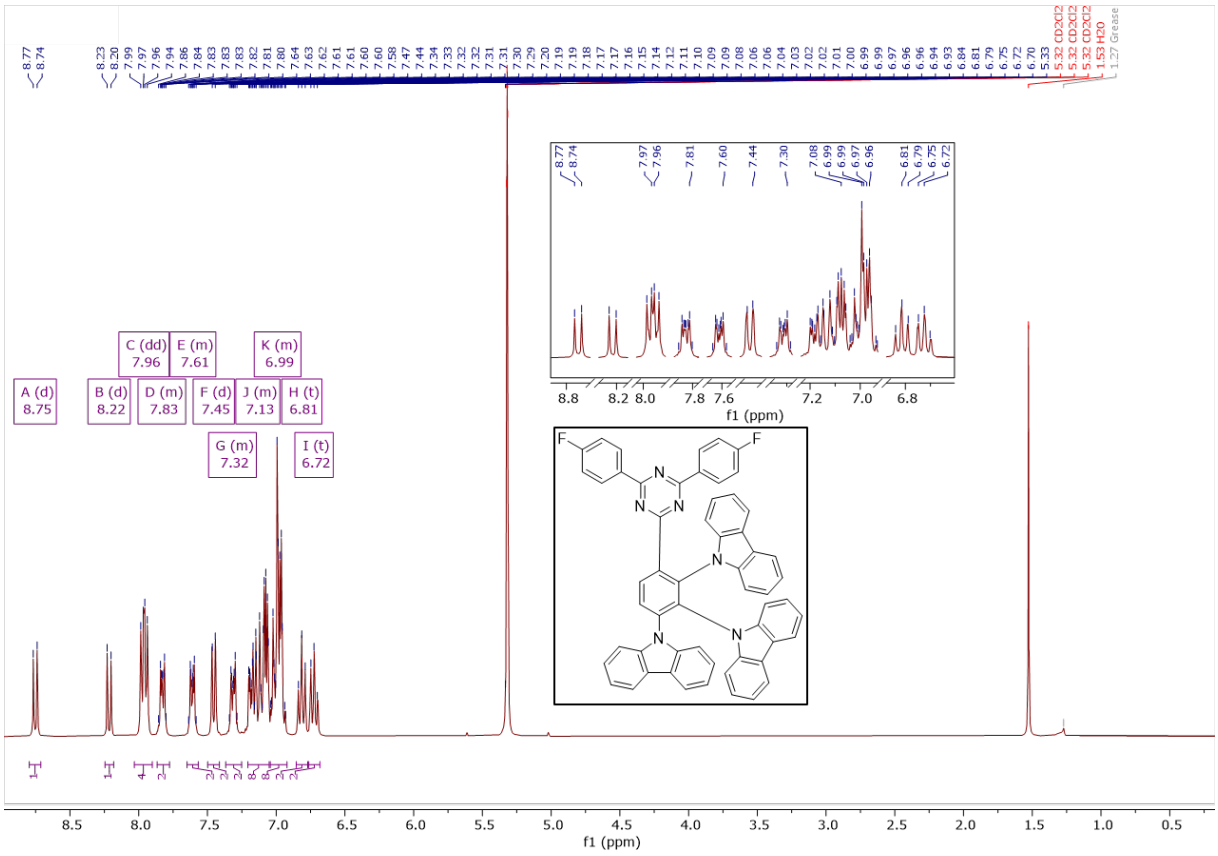

Figure A.12: ^{1}H-NMR spectrum of **234Trz**.

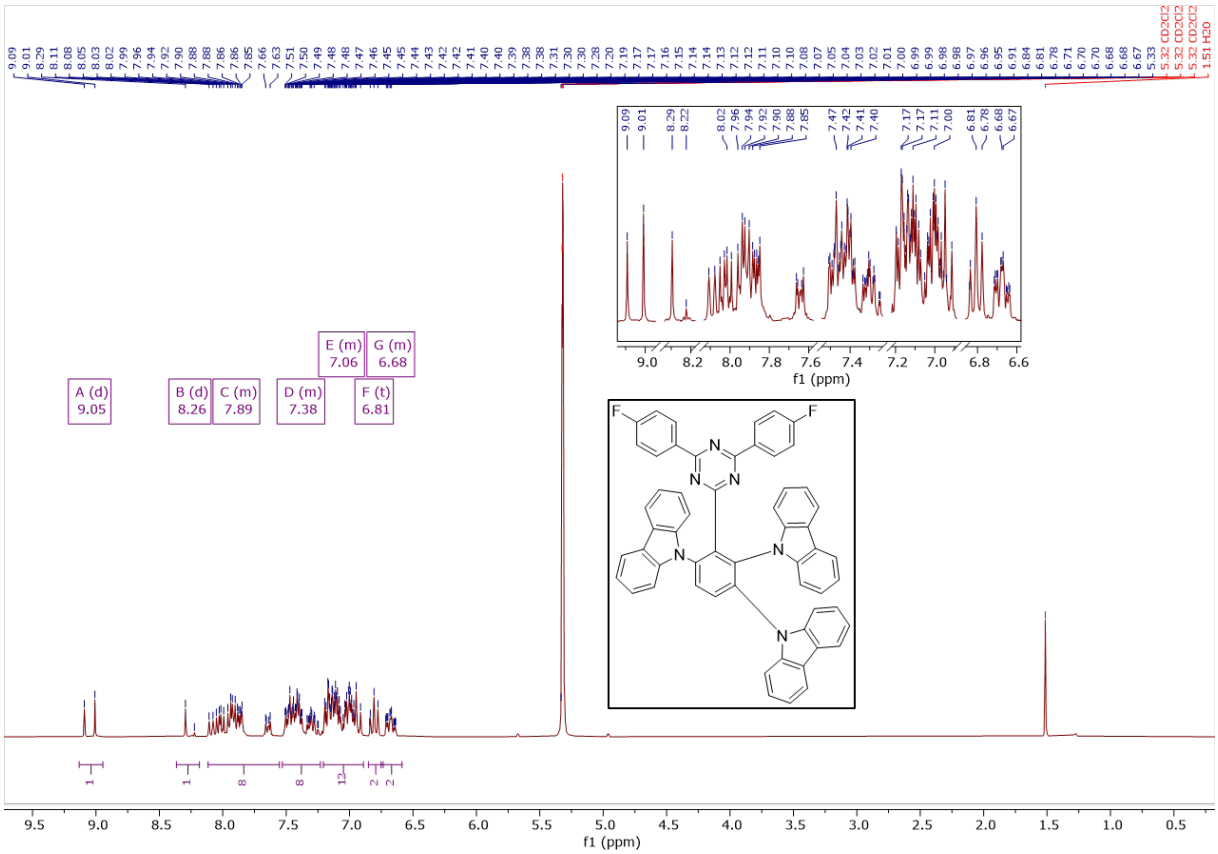

Figure A.13: ^{1}H-NMR spectrum of **236Trz**.

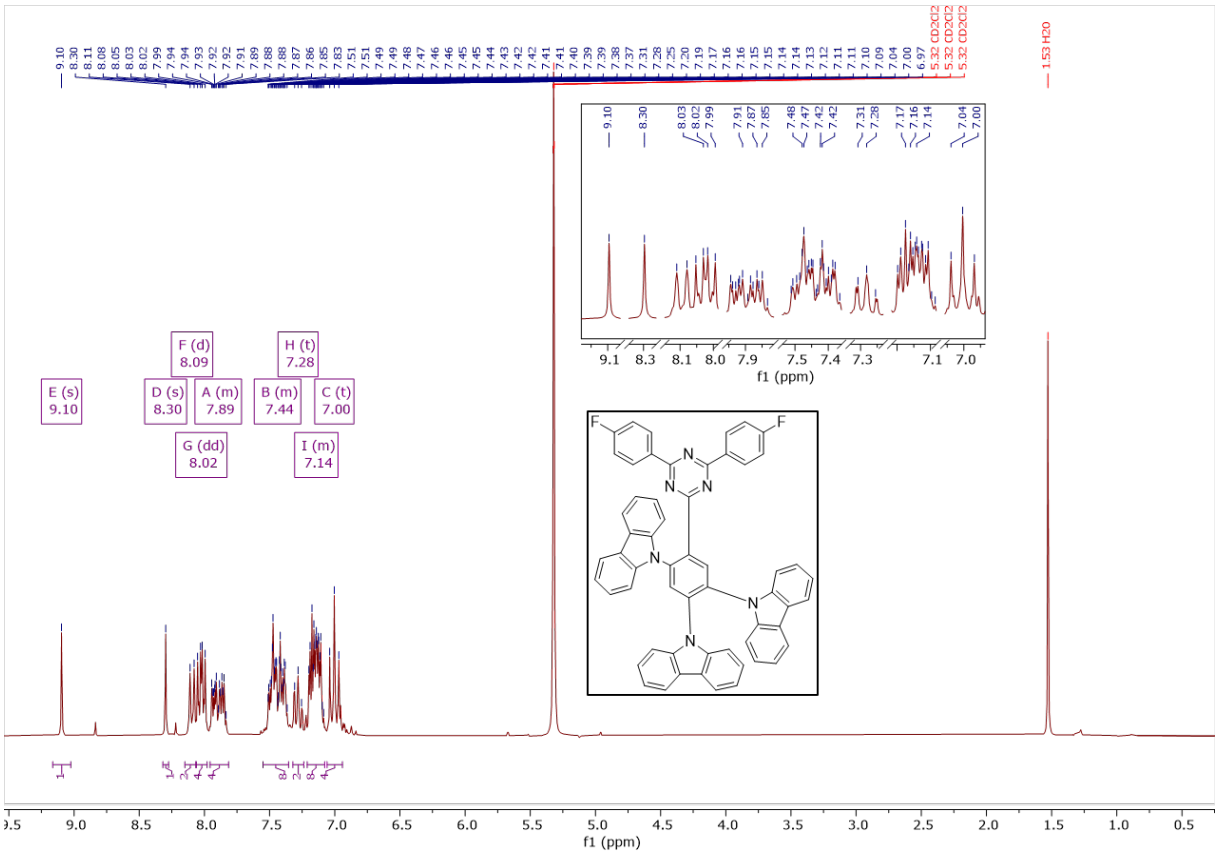

Figure A.14: ^{1}H-NMR spectrum of **245Trz**.

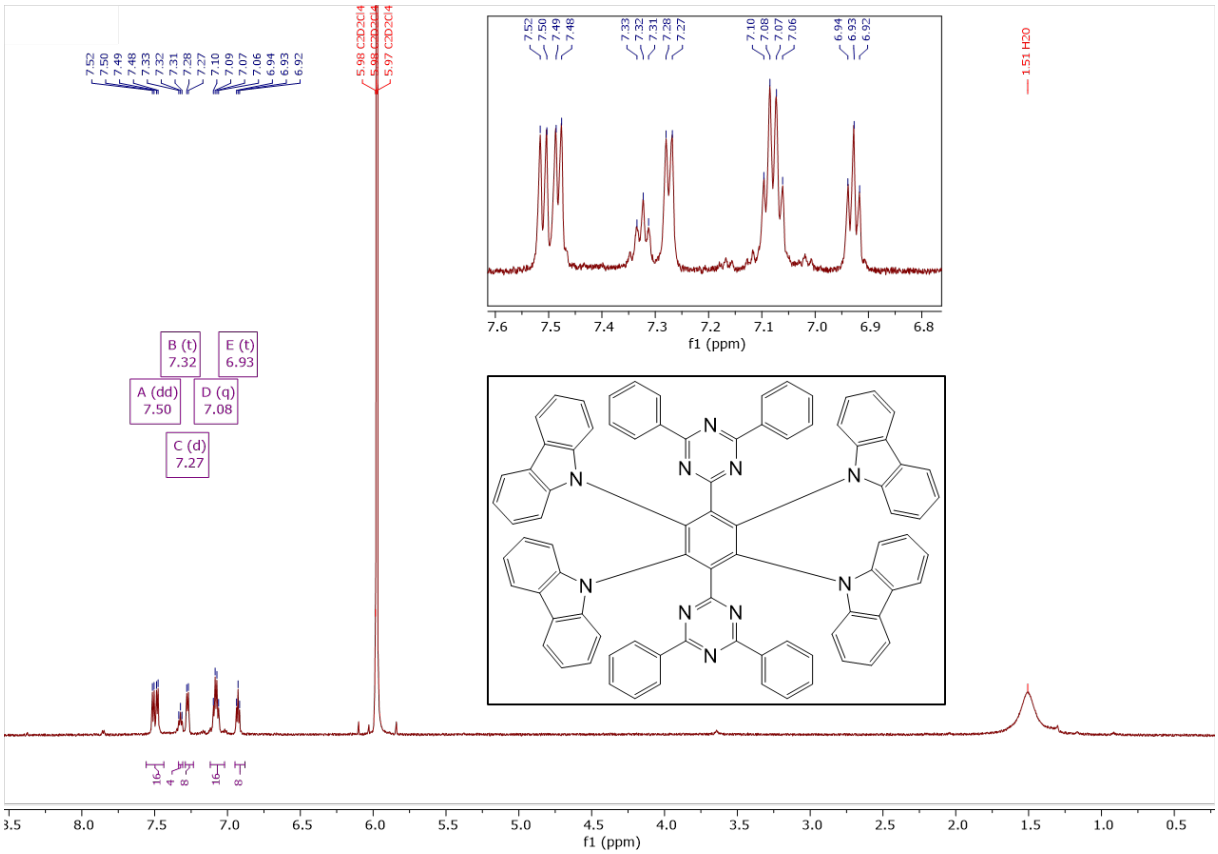

Figure A.15: ^{1}H-NMR spectrum of **4Cz2Trz**.

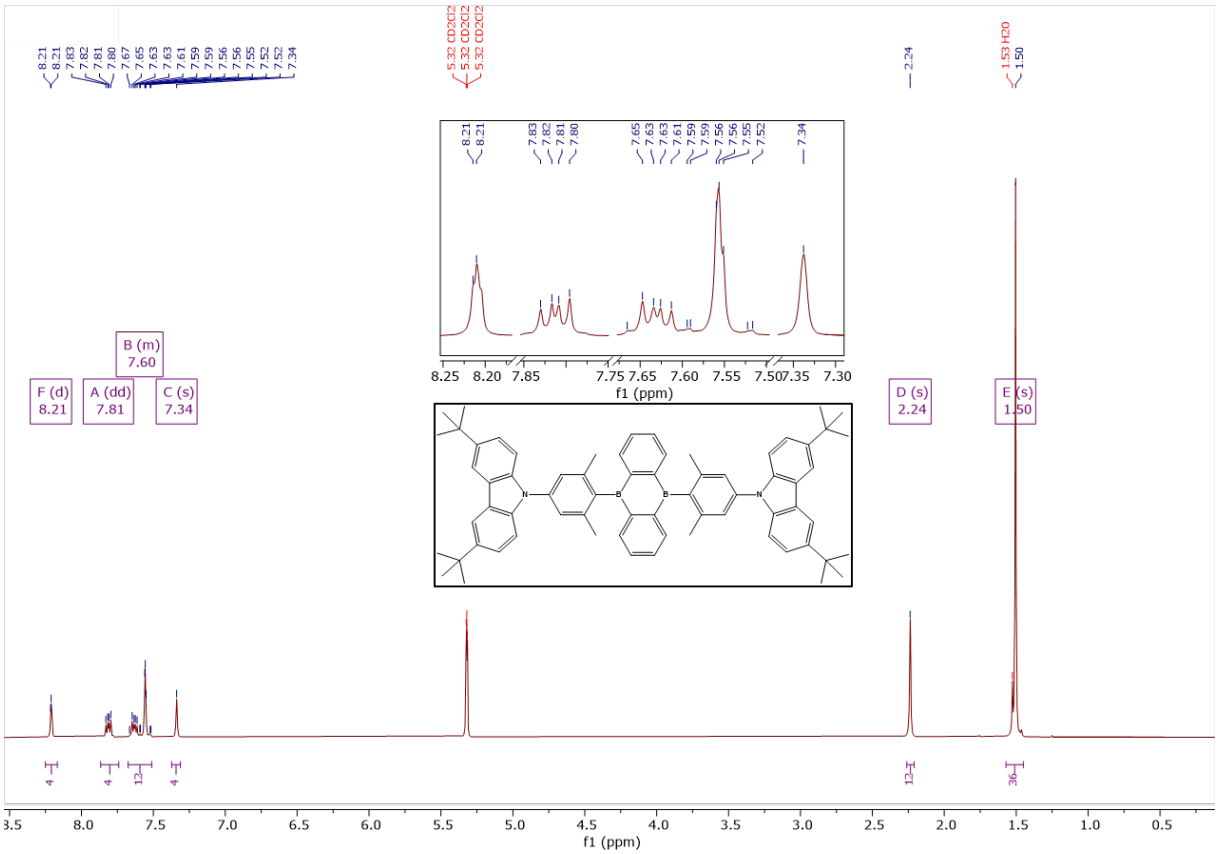

Figure A.16: ^{1}H-NMR spectrum of **tBuCzDBA**.